Chapter 3

The CDS instrument. Data analysis and calibration

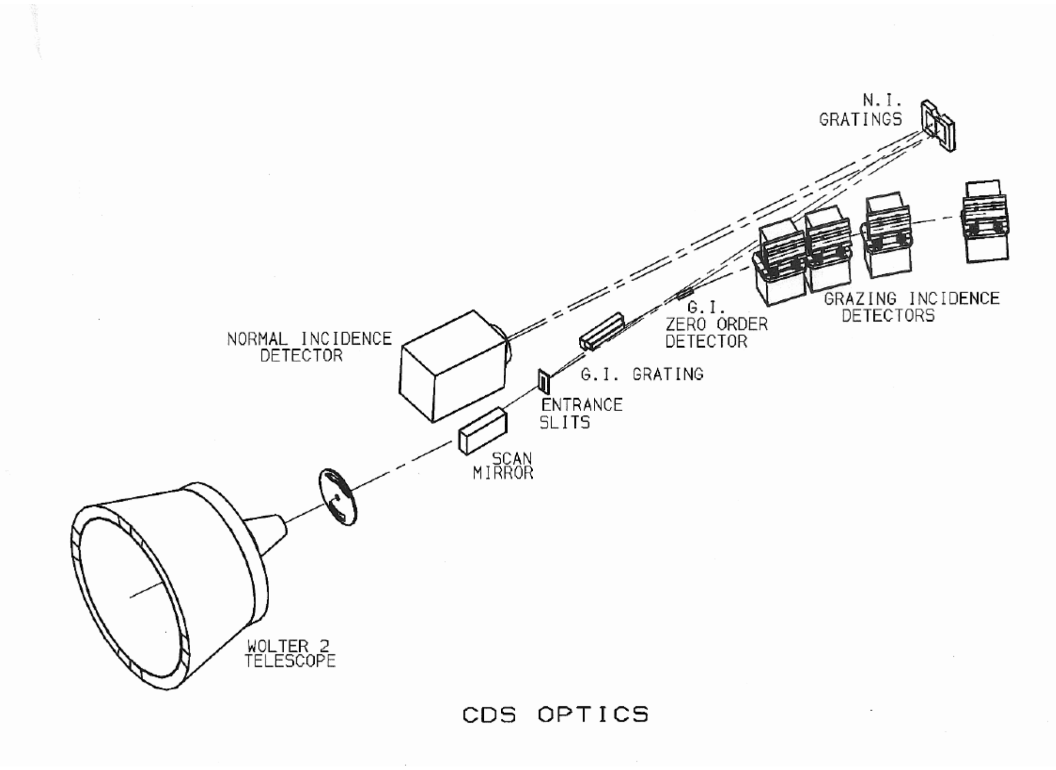

Figure 3.1: *The optical layout of the CDS instrument (from the WWW).*

The CDS instrument and data analysis are described in *Harrison et al.* (1995) and in the CDS software notes, available on the WWW. Since there is no user guide to CDS observations, the descriptions of the instrument characteristics that are given in this Chapter can be regarded as complementary (with examples) to those that can be found in the various software notes, although they reflect the personal experience and methods of data analysis adopted by the author, and should not be regarded as comprehensive.

The CDS instrument (Figure 3.1) consists of a Wolter-Schwartzschild type II grazing incidence telescope, a scan mirror, a set of different slits, and two spectrometers that do not observe simultaneously, the normal incidence spectrometer (NIS) and the grazing incidence spectrometer (GIS).

The slits provide various fields of view ($2''$x$2''$, $4''$x$4''$, $2''$x$240''$, $4''$x$240''$, $90''$x$240''$, $8''$x$50''$) and are normally oriented along the solar N-S direction.

Any position on the Sun is commonly indicated by two coordinates, Solar X and Solar Y, also used to indicate the centres of the pointing of any CDS observation. Solar X is given in arc sec from the disc centre along the East-West (E-W) direction, while Solar Y indicates arc sec from the disc centre along the South-North (S-N) direction. Note that $1''$ corresponds on the Sun to 700 km.

The NIS is composed of two normal incidence gratings that disperse the light into the NIS detector, known as the viewfinder detector subsystem, or VDS. The gratings are slightly tilted, in order to produce two wave-bands (NIS 1: 308 – 379 Å and NIS 2: 513 – 633 Å; note that in this thesis abbreviations such as N 1 and N 2 are also used) on the same detector, one on top of the other (see Figure 3.2). The spectral resolution is $\simeq$ 0.35 Å for NIS 1 and $\simeq$ 0.5 Å for NIS 2. Second order lines have been observed only in NIS 2.

The NIS can provide monochromatic images of the solar field of view. This is accomplished with the *rastering* of a region, moving a mirror and producing contiguous images of one of the long slits. The rastering is performed from west to east (being the normal alignment of CDS with the slits in the solar N-S direction). More details of the NIS spectral characteristics, performance and data analysis are given in Section 3.1.

The grazing incidence spectrometer (GIS) has a grazing incidence spherical grating that disperses the incident light to four microchannel plate (MCP) detectors placed along the Rowland Circle (GIS 1: 151 – 221 Å, GIS 2: 256 – 341 Å, GIS 3: 393 – 492 Å and GIS 4: 659 – 785 Å; note that in this thesis abbreviations such as G 1 or G1 are used). The spectral resolution of the GIS detectors is about 0.5 Å. Many second order lines have been observed in GIS 3 and GIS 4.

The GIS is astigmatic, focusing the image of the slit along the direction of dispersion but not perpendicular to it. Images of the Sun are obtained using a pinhole slit and combining movements of the slit and of the scan mirror. Normally, the movements are such that an area of the Sun is rastered in a zig-zag pattern, starting from south to north and from west to east (in normal CDS alignment). More details of the GIS spectral characteristics, performance and data analysis are given in Section 3.2.

The pointing to any location is accomplished through two mechanisms, one external and one internal. The first is achieved with the use of external legs, that move the whole CDS instrument at 45 degrees to the N-S and E-W directions, with about $2''$ steps. The overall pointing accuracy of the CDS instrument has been *at best* $10''$. This meant that in many cases small target sources have been 'missed', that corrections for the solar rotation are very limited, and that accurate measurements need analysis (e.g. cross-correlations of the observation with large field of view images) to identify the real pointing.

The solar rotation produces an apparent movement of any feature of about $10''$ in an hour at the sun centre. Considering that the typical duration of a CDS observation is one hour, rastering over a region of the order of one arc min, the solar rotation is often a non-negligible effect in observations near sun-centre, and is further complicated by the differential rotation of the solar corona.

CDS has feature tracking software, which moves the entire instrument, but since the accuracy of the movements is much less than the spatial resolution, it is not generally recommended. CDS software note #45 details the limitations, but in short these are:

1) The minimum E-W movement is approximately $2''$.

2) the actual movement may often be $2'' \pm 2''$ with the result that the effect may be 'worse than doing nothing', depending on what effect was intended.

3) The default interval for updating the pointing is 600 seconds. If an individual raster duration is less than this, no correction will ever occur.

The internal movement is more accurate because it is done via the movement of the scan mirror and the slits, with $2''$ steps, and has a negligible error. It is limited to 4' in either direction.

Telemetry constraints usually make it necessary to pre-select a number of NIS wavelength windows to be extracted on-board from the spectra, before the data are telemetered to the ground.

An advantage of the GIS over the NIS is that it is possible to record spectra with short exposure times. In fact, with normal CDS telemetry the four GIS spectra can be downloaded in about 13s. Telemetry is therefore not a limitation for GIS, and the entire GIS wavelength range can be telemetered (and actually should, to have the possibility to then *deghost* the spectra, see Section 3.2). Observations are instead limited by the necessary exposure time to achieve sufficient signal. This exposure time is of the order of hundreds of seconds for coronal holes, much higher than the telemetry time.

An important aspect of the planning of CDS observations comes in the designing of the *'studies'* to be run by the instrument. Each CDS study is a sequence of commands to be sent to the spacecraft, containing pointing, exposure times, movements of the mirror and/or the chosen slit, and various telemetry instructions (for example the specifications of the extraction windows for the NIS). Chapter 4 describes the CDS studies that were used and those that had to be designed and developed to study coronal holes. More details of the main CDS characteristics that are of particular importance for the planning of observations are also described in Chapter 4.

Since the CDS was new, it took almost two years before a correct approach to the data analysis was found, and before the proper software either became available or was developed by the author. As an example, during the first year of the mission, in 1996, there were no suitable IDL routines to perform a gaussian multi-fit of the spectra, and some of the data analysis was done using IRAF packages. Therefore, most of the data have had to be re-analysed more than once, as often happens during a learning process when analysing new data. In the following Sections 3.1 and 3.2, some aspects of the standard CDS data analysis reduction are covered, while more general software developed by the author for the analysis of the coronal hole observations is described in Chapter 4.

The CDS wavelength region is rich in emission lines but is relatively unexplored. A large effort was devoted to the identification of the more than 500 lines present in the spectra, to writing automatic IDL routines for multiple line-fitting of all the lines present in the spectra, and to finding the most useful ones for the various diagnostic purposes.

Because of the moderate resolution of CDS, the presence of second order lines and the various instrumental effects that will be described later, an analysis of CDS spectra of several different solar regions (e.g. active regions, quiet sun, coronal hole, plumes, on-disc, off-limb) was needed to achieve a correct identification of the lines. In fact, many lines observed by CDS are blends and in most of cases different lines become predominant in different solar regions.

Also, it was important to develop a diagnostic method to be used for the line identification. The DEM and abundance evaluation method already described in Chapter 2 was employed. It is interesting to note that very few works have presented solar EUV line identifications that are *not* simply based on line positions, but rather on diagnostic methods as used in this thesis. *Malinovsky and Heroux* (1973) were among the first to apply a diagnostic method (*Pottasch*, 1963) to confirm or reject previous identifications in the 50-300 Å range, using an integrated Sun spectrum with 0.25 Å resolution taken with a grazing-incidence spectrometer flown on a rocket in 1969.

Comparison with higher resolution spectral data also helped assessment of line identification and blending. As described in Chapter 1, there have been only a few studies that could be used for this purpose (*Malinovsky and Heroux*, 1973; *Firth et al.*, 1974; *Behring et al.*, 1976; *Dere*, 1978a; *Dere*, 1982), which observed the entire sun and/or active regions. Aside from these, the most useful studies are those based on the SERTS flights, mainly the 1989 flight (*Thomas and Neupert*, 1994; *Young et al.*, 1998) and the 1995 one (*Brosius et al.*, 1998a; *Brosius et al.*, 1998b).

The importance of CDS/GIS observations for abundance analysis was the motivation for the large and original effort by the author in analysing GIS spectra. To obtain a better understanding of the in-flight behaviour of the GIS detectors, three early (two first-light) GIS observations representative of different types of coronal emission were analysed: an active region, the quiet Sun and a coronal hole. The main goals of this work, presented in Section 3.3, were to identify the principal emission lines, study the characteristics of spectra of different regions, evaluate which lines could be used to perform density and temperature diagnostics, and check the wavelength and intensity calibration. This work contributed to one of the papers that described the first science results from CDS (*Mason et al.*, 1997).

3.1 The normal incidence spectrometer

The VDS detector is mainly composed of a microchannel plate and a 1024x1024 pixels charge coupled device (CCD), composed of four square sections. The CCD was orientated with its columns parallel to the slit alignment. Therefore, any pixel Y position should represent a single Solar Y point, while the grating dispersion is along the pixel X coordinates. In reality, the CDS alignment is more complex, as shown in Figure 3.2 and described below.

A pixel in the detector Y direction corresponds to $1.68''$. The extent in Y of the long slits ($240''$) is therefore 143 pixels on the detector. A pixel in the detector X direction corresponds to about 0.07 Å for NIS 1 and 0.11 Å for NIS 2.

Unfortunately, the NIS spectra contain a large scattered light (*'background'*) component when observed on the solar disc. The NIS 1 spectral region, where CDS has many potential diagnostic lines, is the most affected. This scattered light produces a spatially and wavelength-dependent background component in the spectra, and is most intense in the network spectra, as shown in Figure 5.5.

Typically, in the NIS 1 channel, the scattered light component is a factor of 2 higher in the network areas than in the cell centre areas. The background level can be of the order of the peak intensity of most of the NIS 1 lines (see, e.g., Figure D.1) in coronal hole regions, and also in the quiet sun. The background determination provides the major uncertainty in line intensity measurements. This scattered light is also strongly wavelength-dependent in some areas (as can be seen in many of the spectra presented in this thesis), in particular in bright regions of the network. Because of this, in general only results from comparison of lines close in wavelength were relatively free from such an uncertainty, and in any case this diffuse background component should be carefully removed.

During the first year of analysis , the data were first intensity-calibrated, and the lines subsequently fitted. Because of the wavelength-dependence of the calibration, it was difficult to correctly subtract the diffuse background component. Because of this, and because the intensity calibration was uncertain, it was then decided to perform the fit directly on the photon-event spectra. This also allowed a more appropriate evaluation of the errors, and the possibility of applying different intensity calibrations to the data.

In the following, the procedure that was used to analyse the NIS data is outlined, specifying some aspects of the CDS data reduction.

Subtraction of the CCD bias

This is accomplished by the CDS routine VDS_DEBIAS. All rasters used by the author were designed to include four VDS background windows in the corners of the CCD. Average CCD readout biases are removed from each of the four CCD sections. The error associated with this step is small when compared to the scattered light. Raw data from the VDS detector are in 'ADC' (Analog to Digital Conversion) units. After applying VDS_DEBIAS, the units of the data are 'DEBIASED-ADC'.

Cosmic ray removal

An effect that strongly constrains the observations is the presence of cosmic ray hits. Exposure times cannot be too long, otherwise cosmic rays literally wipe out the use of large fractions of the spectra. Various software routines are available to automatically 'flag' cosmic ray hits with 'missing' values, but an interactive check is highly recommended, although this takes a very long time if the number of exposures and extraction windows is large. The CDS routine CDS_CLEAN_IMAGE was used by the author, together with XCDS_COSMIC. Figure 3.2 shows some cosmic ray hits flagged as missing with this software. Often, the number of cosmic ray hits is such that a line profile in one exposure is lost and no line intensity can be deduced. Therefore, it is highly recommended to raster small regions on the sun a few times, clean the single spectra from the cosmic rays, and then

Table 3.1: *The burn-in factors for some lines, as applied by the standard CDS software, for two dates one year apart. Note the increase of the correction with time and that in 1997 the brightest line in NIS 2 already had a 40% in peak intensity depression. The wavelengths correspond to the predicted position of the lines for the observations on 1st Sept 1997 (there is a time-dependent wavelength calibration).*

Line	Detector	1st Sept 1997	1st Sept 1996
Fe XVI (bl) 335.407 Å	NIS 1	0.141	0.095
Fe XI 341.117 Å	NIS 1	0.005	-
Si X 347.390 Å	NIS 1	0.080	-
Si X 356.023 Å	NIS 1	0.081	0.006
Fe XVI 360.763 Å	NIS 1	0.165	0.093
Fe XII 364.456 Å	NIS 1	0.096	0.051
Mg IX 368.086 Å	NIS 1	0.226	0.146
O III 525.863 Å	NIS 1	0.104	0.050
He I 537.108 Å	NIS 2	0.161	0.112
O IV 554.499 Å	NIS 2	0.236	0.146
He I 584.370 Å	NIS 2	0.419	0.321
O III 599.620 Å	NIS 2	0.124	0.082
Mg X (bl O IV) 609.818 Å	NIS 2	0.268	0.158
Mg X 624.990 Å	NIS 2	0.189	0.099
O V 629.819 Å	NIS 2	0.369	0.274

average the spectra. In this way, the effect of the cosmic rays is removed (unless cosmic rays hit the same emission line at the same spatial position along the slit). Another way of reducing the effect of the cosmic rays is to spatially average the line profiles.

Corrections for flat-fielding, burn-in and nonlinear effects, using VDS_CALIB

The flat field of the detector presents variations of only a few percent. However, before the spectra are divided by the appropriate parts of the flat field, the burn-in correction is added to the flat field. The VDS detector sensitivity decreases with time in the most strongly illuminated areas (i.e. in the centres of the brightest lines), because of local gain depression (*burn-in*). This has been monitored since launch using wide slit observations. The line profiles are reconstructed, adding to the flat field some gaussian 'absorption' profiles with a predicted width, position, and normalized peak intensity. Table 3.1 shows some of the lines that need such a correction. Note how the correction changes with time, and how considerable it is. For example, the He I 584 Å line, the brightest in these detectors, had already in September 1997 a burn-in of 40%. This correction is accurate (to a few percent) only for the bright and un-blended lines.

VDS_CALIB, after dividing the spectra by the flat field, corrects the exposure time and divides it into the data to give the ADC count rate. The correction to the exposure time is due to the electronic shuttering, which makes each exposure slightly longer (0.1165 seconds for the normal VDS operating voltage). VDS_CALIB also applies a correction for non-linear effects at high count rates (ADC counts per photon, a function of the voltage).

Then, the VDS throughput is divided into the data to convert from DEBIASED-ADC count-rate to photon-events/pixel/s. The term “photon-events” refers to those EUV photons which actually interact with the detector. For the subsequent data analysis, it is useful to also have the spectra in photon-events/pixel and so the output from VDS_CALIB is multiplied by the ‘corrected’ exposure time.

Correction for geometric distortions, using VDS_ROTATE

Unfortunately, it is not possible to make in-flight adjustments to CDS to correct for, e.g. distortion during launch. This has resulted in a series of effects, that can only be partially corrected for during the data analysis.

First, it seems that the NIS instrument is not in focus. In fact, the line widths created by the $2''$ and $4''$ slits appear to be about the same, and much larger (by factors ~ 2) than in pre-flight measurements. No correction is possible.

Another optical factor to take into account in the data analysis is the fact that the centres of the various slits are not co-aligned, which has the consequence that images taken will not be aligned in the Y-direction. However, images taken with different slits by the author show that the $4''$x$4''$ and the $4''$x$240''$ slits are co-aligned, in accordance with results based on other work (D. Pike, priv. comm.), which have shown for the other slits misalignments of up to $4''$.

Then, the spectra are slanted, in the sense that the dispersion direction is tilted relative to the rows of the VDS CCD, with different angles for NIS 1 and NIS 2, as shown in Figure 3.2. This is the main effect. On top of this, the spectral lines appear to be tilted relative to the dispersion direction (i.e. the angle they for with the dispersion direction is not 90 degrees, and varies). The slant of the spectra complicates the planning of a CDS ‘study’ and data analysis. A correction for the slant and tilt of the lines can be done in two ways, one during the data planning and one in the analysis (by the routine VDS_ROTATE).

During the planning of a CDS ‘study’, the CDS routine MK_RASTER makes the following adjustment. If a study is designed with specific data extraction windows then the windows are positioned on the detector at different row positions to allow for the slant. Using this method, data extracted at any of the wavelength windows are co-spatial on the Sun to

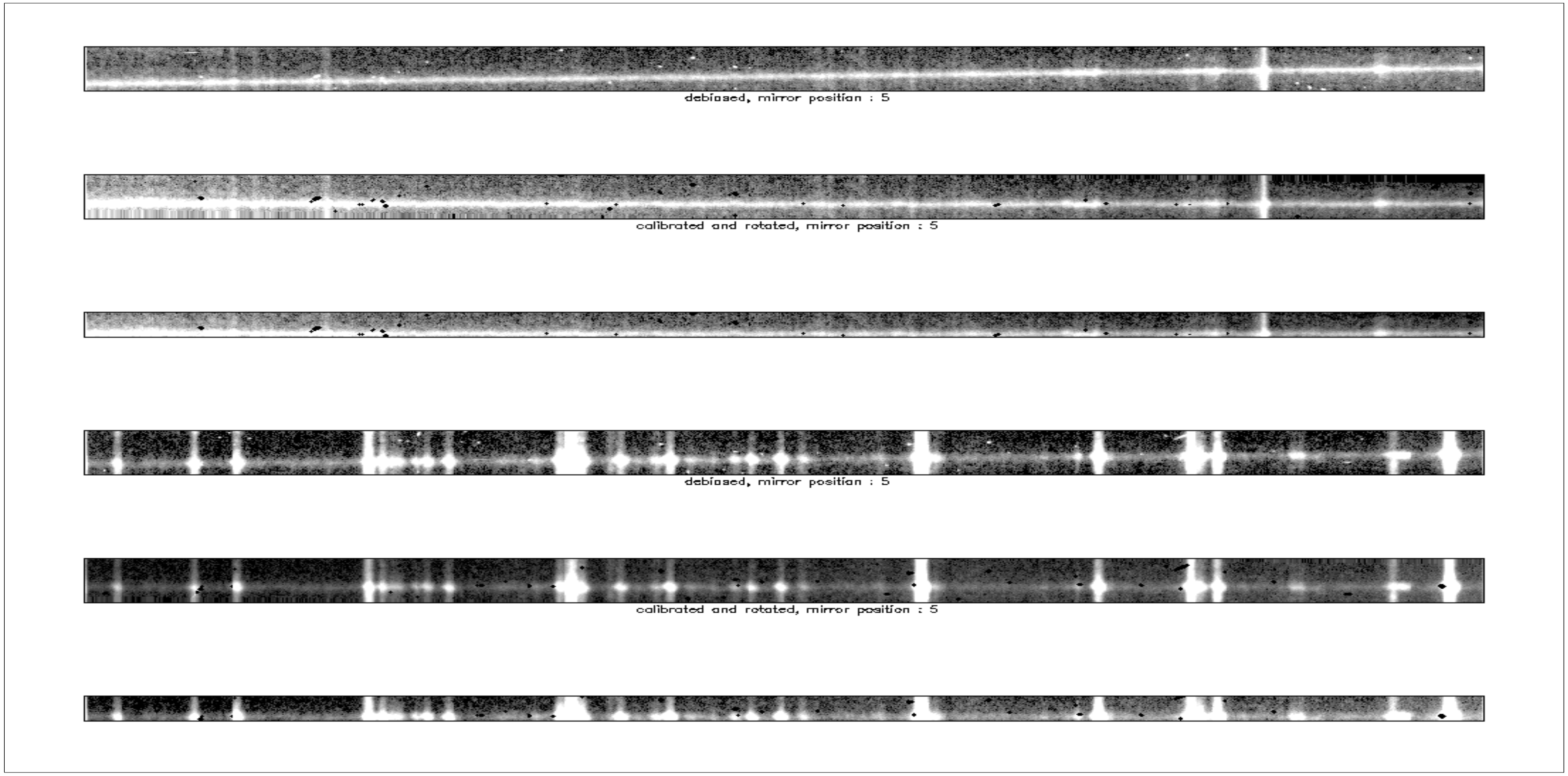

Figure 3.2: *The NIS spectra, showing the effects of the slant of the spectra and the cosmic rays. First three spectra, from top to bottom: a NIS 1 de-biased spectrum; the same spectrum with the cosmic rays flagged as missing data, calibrated using VDS_CALIB (and NIS_CALIB), and rotated (using VDS_ROTATE); the previous spectrum, but with the unusable spatial areas (top and bottom rows) removed. The bottom three figures show the NIS 2 spectra. The particular exposure shown here was taken during a brightening in a spatially-localized region of the network. The bright stripe across the spectra is caused by enhanced emission in all the emission lines, plus by scattered light, and clearly shows the slant of the spectra, that is more pronounced in NIS 1. Note that a large portion of the spectra (along the slit) is lost after the correction for the slant is applied.*

within one pixel in Y. The usual extraction window height is 143 pixels, corresponding to $240''$.

For studies that use the full default extraction window the correction for slant has to be applied during data analysis, and it is important in the planning phase to extend the Y-size so that a sufficiently large area of the detector is extracted, to cover the full rotated spectrum. In the data analysis, VDS_ROTATE is used to rotate the entire NIS 1 and NIS 2 spectra to correct for the slant and tilt. In this category there are two further types of CDS 'studies', one that extracts the full spatial positions along the slit (as done in the spectral atlases) and one with a shortened extraction along the slit (case shown in Figure 3.2). In the case of spectral atlases, two windows of 1024x160 pixels are extracted. VDS_ROTATE pivots around the centre of the data. There is a difference in the height of the unrotated data for NIS1 and NIS2, where the first is 160 pixels in height, and the second is only 153 pixels. Therefore, NIS1 data pivots around vertical pixel 79.5, while NIS2 data pivots around pixel 76. Thus, there is a 3.5 pixel difference in the positions due to that effect. VDS_ROTATE then cuts the two spectra to 143 pixels, although two arrays of 1024x160 pixels are given in output. In the other case, with shortened extraction along the slit, there is no difference in the height of the unrotated data for NIS1 and NIS2, and the spectra are rotated around the centre of the data.

In any case, the slant of the two channels is such that about $30''$ along the slit direction is lost, if one is interested in having all the NIS spectral information at the same spatial position. Figure 3.2 shows the rotated NIS 1 and NIS 2 spectra.

The tilt of the lines can be partially corrected for by applying the routine VDS_ROTATE to the spectra, or by adjusting the wavelength calibration.

The NIS wavelength calibration also has some peculiar aspects. The wavelength calibration requires a 'scan mirror correction', which appears to be different for different observations. Then, the NIS wavelength calibration has been found to be a function of the CDS optical bench temperature (D. Pike, priv. comm.), which continuously changes depending on the solar illumination, and which has been observed to cause shifts of up to a pixel (0.1 Å), which for a strong line such as O V 629 Å corresponds to a velocity of 56 km/s.

Even after all the possible tilt and wavelength corrections, the line profiles are not strictly gaussian, and residuals to gaussian fits show peculiar spatial patterns still not explained. Recently, *Haugan* (1999) has suggested that a possible explanation for some of these features is an asymmetric tilted point spread function.

In conclusion, NIS does not have an accurate 'standard' wavelength calibration, and therefore, in the absence of any reference wavelength scale, most absolute wavelength measurements are subject to various uncertainties. Also, the NIS shows a series of geometrical effects that are not well understood and are difficult to explain, and can only be partially corrected for.

Spatial resolution and binning along the slit

It has to be noted that the resolution of the instrument (FWHM of the Point Spread Function or PSF) is at least 5–6$''$. Therefore, the pixel resolution (1.68$''$) along the slit is much less than the spatial resolution, and the spectra can be binned without losing any spatial information. Binning over two pixels was applied to all the NIS data during the analysis. This not only reduces by a factor of two the data volume, but is also useful in reducing the effect of the cosmic rays, since it is an averaging process.

Alternatively, binning can be implemented on-board as has been done for some CDS studies developed by the author (see Table 4.1), to reduce the telemetry time.

Line-fitting

Line intensities were obtained by using multiple-line-fitting IDL routines (CFIT package, *Haugan*, 1997) on the spectra, assuming gaussian profiles, and removing the *'background'* by fitting polynomials.

The CFIT package has many advantages, compared to many other line fitting packages found in the literature (and tested). It is very flexible, in the sense that any type of line profile and/or background, with any number of parameters can be fitted; any number of lines can be fitted over a wavelength region (although large numbers considerably slow the process); the parameter's values can be allowed to vary within some fixed ranges, or can be kept constant; each fitted line's parameters can be checked and modified interactively. The fit is performed with a non-linear weighted least squares fit, optimizing an initial user-supplied set of parameters in order to find the best agreement between the chosen model function and the observed data.

Many IDL routines have been written by the author to apply the routines of the CFIT package to different types of observations. For example, in some cases each CDS NIS 'study' is composed of a scan with the long slit in the X-direction, giving two spatial dimensions. The data to be analysed is in this case a 'cube'. In other cases, there can be a time dimension to be added, or only one spatial dimension, if one is interested in the line variation along only one spatial direction. In any case, the fit is actually done for a one-dimensional spatial-temporal dimension at a time, i.e. on a single spectrum, intensities versus wavelengths.

Gaussian profiles have been assumed for the analysis of NIS spectra, and therefore the parameters are the peak intensity I_0, the central wavelenghth, and the full width of half maximum $FWHM$. In many cases lines are closely spaced, and a proper de-blending can only be done if ranges for the positions and widths are given. Only 'real' lines that have a width at least equal to the instrument resolution are fitted.

Since different CDS 'studies' extract different spectral ranges, routines that could automatically analyse any type of NIS data were written. This was done first by writing a database with the parameters (values, minimum and maximum range, for a total of about 1500 values) of all the lines observed by NIS in all solar regions examined, a total of more than 165 lines.

Then, two sub-types of fitting routines had to be written, one to analyse full spectral data, and one for the 'windowed' data. In fact, the line fitting programs cannot cope with too many lines to fit, and the full spectral data had to be fitted in sections. The windowed data, on the other hand, have to be merged whenever possible, to allow a better evaluation of the background.

In either of these two sub-types of fitting routines, the fit on the background is performed first. To do so, all the pixels that correspond to regions where lines are expected are flagged with weights=0., and the routine therefore attempts a polynomial fit to the remaining pixels. This is done for the full spectral data over the whole spectral range, before dividing the spectra into sections for the fit of the lines.

Then, the integrated line intensities are estimated from the background-subtracted spectra by summing pixel values. This first estimate is very close to the final value that is provided by the gaussian fit for well separated lines, if a correct position and width of the line are given. This has been checked on many test cases.

After this, the peak intensities are estimated and given to the line fitting routine, with the position and $FWHM$ as an initial value, to speed the fitting process; this can take a long time (of the order of an hour on a Digital workstation for a typical medium-size NIS raster). The background can be allowed to vary. Then the fit is interactively checked, adjusting some parameters as necessary. This is also time-consuming. The parameters are then saved in IDL save files, together with the processed data and various information. This is the first step of the analysis completed.

Error estimates.

The various noise sources associated with the NI spectrometers are described in *Thompson* (1997). As well as Poisson noise associated with the photons which interact with the detector, there is another source of noise due to the fluctuation in the amount of amplification in the detector system, known as the pulse height distribution (PHD). This latter effect can be assumed to be comparable to the Poisson noise. Other sources of noise are only detector-dependent. The readout noise R has been found to vary from 0.62 to 0.83 photon-events/pixel, and therefore has an effect only at low light levels. A value of 0.7 is assumed in this work.

If N is the total number of photon-events in a line, the Poisson noise is $\sqrt{N}$, and assuming that the PHD component is comparable, and adds in quadrature, the total photon noise is $\sigma_N = \sqrt{2 * N + R^2 * n_{pix}}$, where n_{pix} is the number of pixels being summed over and R is the readout noise per pixel. In reality, the main source of error (not mentioned in *Thompson*, 1997) in determining intensities in NIS spectra is the scattered light in the detector, and what we want to measure is the intensity of each background-subtracted line $I = N - B$, where B is the total background intensity over the line. The noise associated with the background is again $\sigma_B = \sqrt{2 * B + R^2 * n_{pix}}$ and the error on the intensity I is therefore

$$\sigma_I = \sqrt{\sigma_N^2 + \sigma_B^2} = \sqrt{2 * (I + B) + R^2 * n_{pix} + 2 * B + R^2 * n_{pix}} \tag{3.1}$$

In the case of n_{avg} spectra averaged, we have to divide σ_I by $\sqrt{n_{avg}}$.

Another way to determine the error on the intensity is directly from the errors on the parameters of the fit. All the line profiles have been assumed to be gaussian, and the total intensity in the line has been derived from the peak amplitude I_0 and the line full-width-half-maximum $FWHM$ (in pixels):

$$I = \frac{1}{2}\sqrt{\frac{\pi}{\ln 2}}\ \ I_0 \ \ FWHM \tag{3.2}$$

Since the fitted peak amplitude I_0 and the $FWHM$ are not statistically independent, in the sense that too high $FWHM$ favors too low I_0 and vice versa, the error on the intensity σ_I has been calculated from:

$$\frac{\sigma_I}{I}^2 = \frac{1}{2}\left[\frac{\sigma_{I_0}}{I_0}^2 + \frac{\sigma_{FWHM}}{FWHM}^2\right] \tag{3.3}$$

In most cases, the errors derived from (3.3) are very similar to those from (3.1). Unless stated, the errors derived from the parameters (3.3) are those presented in this thesis.

The intensity calibration

The CDS routine NIS_CALIB performs the conversion from photon-events/pixel/s to the calibrated default units 'photons/cm^2/sec/arcsec^2'. The conversion factor from arcsec^2 to steradians is simply $(\pi/(180 \times 60^2))^2 \simeq 2.35 \times 10^{-11}$, while the conversion from photons to ergs is $hc/\lambda \simeq 1.986 \times 10^{-8}/\lambda$, where λ is in Ångstroms. There are several factors which determine this final conversion of the data from photon-events to absolute units.

1. The absolute sensitivity $ef(\lambda)$ [counts/photons] as a function of wavelength.

   The absolute sensitivity of the NI spectrographs is a combination of the reflectivity of the primary mirror, the secondary mirror and the scan mirror, the efficiencies of the gratings, and the quantum sensitivity of the VDS detector. The wavelength dependence of absolute sensitivity is therefore a combination of the wavelength dependence of all these various factors. The sensitivities were measured on the ground at only a few wavelengths (see Figures 3.28, 3.29, and 3.30). See the calibration Section 3.4.10 for more details.

2. The telescope aperture $A_t(k)$ [cm^2].

   $A_t(k)$ is a function of the scan mirror position (k), because as the scan mirror moves, the two NIS gratings are 'seeing' apertures of different sizes.

   The variations, around a median value of 27–28 cm^2 (for NIS 1–2) are considerable ($\sim$ 20%) over the full extent of the scan mirror positions ($4'$). The CDS routine GET_EFF_AREA provides the pre-flight values of $A_t(k)$, and these have been confirmed by in-flight measurements (W. Thompson, priv. comm.).

3. Angular width of the slit.

   The values are well known.

4. The exposure time.

Note that, unless stated otherwise: all the NIS spectra presented in this thesis are in photon-events; the spectral line intensities in the Figures are in phot s^{-1} cm^{-2} $arcsec^{-2}$; the intensities in the Tables are in ergs s^{-1} cm^{-2} sr^{-1}; the intensity ratio values, both in Tables and in Figures, are obtained from the intensities in ergs s^{-1} cm^{-2} sr^{-1}, and therefore, for clarity reasons, are indicated as 'ratio values (ergs)'. The errors in the intensities do not include all the systematic errors that can come from all the correction and calibration factors above-mentioned, of which the main one is the error in the instrument sensitivities, discussed below.

3.2 The grazing incidence spectrometer

The GIS detectors (*Breeveld*, 1992; *Breeveld*, 1996) are composed of a stack of micro-channel plates (MCPs), and a spiral anode (SPAN) to read the position and charge of the electron cloud created by the MCPs. The reading is converted with an 8-bit analogue to digital converter (ADC) which outputs data at (x, y) position values (known as GIS raw data). The (x, y) values form a spiral in cartesian coordinates (see Figure 3.3), which contains all the one-dimensional spectral information (the GIS being astigmatic, no more information is needed). The wavelength varies with distance along the spiral and the width of each *arm* is related to the noise in the electronics.

Figure 3.3: *The spiral pattern of a GIS observation (courtesy of R. Bentley).*

A set of parameters, called a look up table (LUT) is produced for each detector, fitting this spiral pattern, in order to convert the signal produced by the photon events to an array of 2048 spectral data points as a function of wavelength.

Because the gain in the micro channel plates is sensitive to the intensity, the voltages applied to each detector are adjusted depending on the slit used and the solar conditions (active or quiet sun), creating different spiral patterns, each requiring a different set of LUTs.

Because it takes too long to telemeter to the ground the raw data, this is done only once in a while to generate the LUTs. Normally the raw data are converted on-board by applying a set of LUTs, uniquely identified by a number *GSET_ID*, to the raw data. Various sets of LUTs are stored on-board for use, and loaded before the GIS starts exposing (it takes about half an hour). It is important, during planning, to select the correct set of LUTs (i.e. GSET_ID number) for the type of observation, otherwise the telemetered spectra are not usable.

The GIS spectra have various effects that must be carefully considered before starting any data analysis. Some effects are typical of any MCP detector, and are electronic dead times, short term gain depression and long term gain depression.

The GIS operates by sending a continuous stream of event positions to the Command and Data-Handling System (CDHS). The various electronic dead-times are such that any events occurring within about 10 ms of each other will be rejected, and higher rates will render the data meaningless.

Short term gain depression occurs when count rates per pixel are above 40. In this situation, the MCP cannot re-charge fast enough to provide full gain for every event, and the data are not usable.

Long term gain depression is an *ageing* effect, a reduction in detector sensitivity over a long time interval due to continued illumination. The applied high voltage can be increased to compensate for the decrease in the MCP gain with time. However, the gain depression will be greatest at the position of the brightest lines so a wavelength-dependent effect will remain. Corrections for flat field and long term gain depression were not included in reduction of data for this thesis since they are not yet available. It is known, however, that these corrections are small.

Some other effects are very peculiar, and are related to the finite number of bits employed in the ADCs, and the noise of the electronics, that create distortions in the spiral pattern and wrong encoding by the LUTs. These are *fixed patterning* and *ghosts*, and are described in detail in the following two Sections. Some of the results presented in these two Sections are based on the analysis of GIS observations described in Section 3.4.4, and are also partially reported as contribution of the author in *Landi et al.* (1999a).

3.2.1 Fixed patterning and line profiles

The profiles of the GIS lines are predominantly instrumental. They are corrupted by the superposition of a *spiky* effect on the whole spectrum, referred to as *fixed patterning.* Counts falling near the boundary of a pixel can be shifted to neighbouring pixels, producing narrow spikes and troughs in the profiles of the emission lines. Weaker lines can appear swamped by this effect. Figure 3.4*a* shows a portion of the GIS 1 spectrum, as an example. It is not only impossible to define a line profile, but even hard to recognise the presence of weak lines. Fixed patterning *should not alter* the total counts recorded in an emission line; it merely displaces some of them.

It is evident that it is necessary to apply some kind of correction in order to restore the original line profiles and to clean weak lines without altering the total intensity of the lines. This is important since a fixed patterned line profile is an obstacle to any fitting routine, which tries to adapt a selected analytical line profile to the input data. This is particularly important in the case of unresolved blending of lines. Strong departures from smooth profiles cause additional uncertainties in the evaluation of line intensities, and moreover can make it impossible even to fit weak lines.

Since it is impossible to rebuild the original pixel intensities from the observed spectrum, a smoothing technique, which does not change the total count-rates, is the only 'correction' that can be applied.

Many smoothing methods are available. In order to evaluate the effect that a smoothing procedure has on the GIS spectra, three different methods have been applied to a spectrum, and their effects compared. This was done by applying the same line fitting procedure to the smoothed spectra, and comparing the derived intensities with those obtained by simply summing up the pixel intensities over the entire 'line profile'. Since the fixed patterning is expected to simply shift counts to neighbouring pixels, summing the pixel values should give the most accurate measurement of the intensity of an un-blended, well isolated line, because it is independent of the type of line profile adopted. Unfortunately, the moderate resolution of the GIS does not allow this to be applied for most of the lines.

The three different methods chosen are: boxcar filtering with 3 pixel width, convolution with a gaussian function with a 2 pixel-wide σ, and Fourier filtering of proper width. The widths of the filtering kernels were chosen in order to reasonably smooth the GIS spectra, with the smallest broadening of the line profiles. In Figure 3.4 a comparison between the original GIS 1 spectrum and the results of the three smoothing procedures is reported between 169 Å and 176 Å.

It is possible to see that the shape of the spectrum is much improved by all three smoothing procedures. It is important to note however that the 3-pixel boxcar smoothing (Figure 3.4*b*) is not able to remove completely the effects of fixed patterning, though these are greatly reduced, and produces double peaked line profiles, more evident for most of the GIS 1 lines and less pronounced in the lines observed in the other spectral windows.

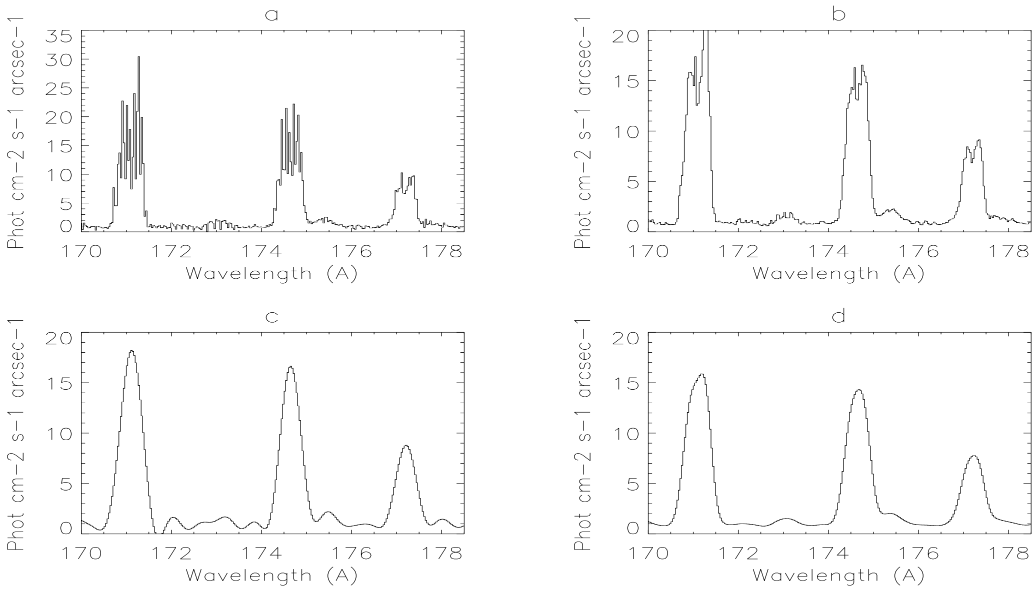

Figure 3.4: *Effects of different smoothing procedures applied to a portion of the GIS 1 active region spectrum.* a*: original spectrum;* b*: box-smoothed spectrum;* c*: Fourier-filtered spectrum;* d*: Gaussian-convolved spectrum.*

Fourier filtering (Figure 3.4*c*) produces nearly gaussian line profiles and a very clean spectrum, but alters the background, making it very difficult to distinguish weak spectral features as real lines or spurious effects produced by the smoothing procedure.

The gaussian convolution is able to clean line profiles (Figure 3.4*d*), and the resulting lines are close to gaussian-shaped profiles (as expected), with a flat background.

Line profiles.

However, various tests done on all the GIS spectra have shown that none of the smoothing procedures is able to provide gaussian profiles, unless a significant loss of spectral resolution is accepted, increasing the widths of the kernels. Moreover, these tests have also shown that, whichever smoothing procedure is applied, *each line in the GIS spectra presents a slightly different (and wider) smoothed profile.* The GIS 1 is the worst channel in this respect, where many lines are double-peaked.

Some of these (unexplained) effects must be due to the MCPs or to some distortions related to the optics. In fact, pre-flight observations (*Bromage et al.*, 1996) did show the fixed patterning effect, but not anomalous line profiles. Also, the line widths were narrower (by about a factor of 2, see the comparison in *Landi et al.*, 1999a) than those that are observed in-flight, even after including a broadening correction due to the fact that the ground calibration used a narrow-beam source of EUV radiation. It is therefore possible that distortions took place during flight, some of which might be common to the NIS, which has also shown larger in-flight line widths and various geometrical effects, as already described. Another explanation for the anomalous line profiles can be found in the fact that the line positions were observed to shift depending on which part of the aperture is illuminated, an effect reported in *Bromage et al.* (1996) (see Figure 24) and measured scanning the aperture with the narrow-beam source. Since the Sun fully illuminates (usually) the aperture, the resulting observed line profile would be a superposition of different line profiles shifted between each other. Double-peaked line profiles can therefore be created. In addition to these profile anomalies, there are some variations of the line widths along each detector as expected, due to the configuration of the detectors (which are flat) along the curved Rowland Circle.

In conclusion, the GIS line profiles (that in any case are instrumental) are anomalous and therefore the spectral resolution of the GIS depends on the type of smoothing adopted to reduce the effects of the fixed patterning.

Comparison of different smoothing procedures.

In order to quantitatively compare the three different smoothing procedures, it is necessary to use a line fitting routine that adapts a known line profile to the observed spectral lines, to obtain the line intensities. Due to the complexity of the GIS line profiles, the adopted method has been to use gaussian profiles. First, the line fitting routines of CFIT (see above) and ADAS (*Summers et al.*, 1996) packages have been applied (in collaboration with E. Landi) to the same dataset, to evaluate the effect a different line fitting routine has on the results. A general agreement was found, with differences between the results smaller than $\simeq 5\%$ for the strongest lines. These differences were ascribed to the different evaluation of background in the two packages, which results in larger differences for weaker lines. It is worth noting that the GIS background emission results from a combination of true continuum emission, scattered light, detector effects (some of which are present at the edges, others that are related to ghosting, see below), and a contribution from weak emission lines. A proper evaluation of the background emission will only be possible when detector effects have been removed through proper flat-fielding.

The CFIT package was used to deduce line intensities, positions and widths for GIS spectra filtered with the three smoothing procedures. Table 3.2 reports the results in terms of line intensities and widths for some lines of the GIS 1 'raw' and smoothed spectra.

The same linear background has been adopted for the four spectra. This choice is suggested by the fact that the boxcar filtered spectrum and the gaussian convolved spectrum have a nearly identical background. The Fourier filtered spectrum instead alters the background more significantly. Table 3.2 shows that there is good agreement between the intensities

Table 3.2: *Comparison of fitting results. In the first column are the results of fitting the original spectrum, then the results from the three spectra smoothed using different methods. In the last column the results from the sum of counts from the original spectrum is given. The same background was imposed in all 4 cases.*

Ion	Wavelength (Å)	Original sp.	Boxcar sm.	Fourier sm.	Gauss sm.	Sum of counts
		Line widths (pixels)				
Fe IX	171.07	0.49±0.01	0.51±0.01	0.52±0.01	0.54±0.01	-
O VI	173.00	0.65±0.11	0.65±0.07	0.65±0.07	0.65±0.07	-
Fe X	174.53	0.47±0.01	0.49±0.01	0.51±0.01	0.51±0.01	-
Fe X	177.24	0.47±0.02	0.61±0.02	0.65±0.02	0.65±0.02	-
Fe XI	180.41	0.45±0.01	0.45±0.01	0.50±0.01	0.48±0.01	-
O VI	184.00	0.60±0.06	0.60±0.05	0.37±0.05	0.60±0.05	-
Fe X	184.54	0.49±0.01	0.38±0.01	0.51±0.02	0.41±0.01	-
Fe XII	186.87	0.50±0.01	0.52±0.01	0.51±0.01	0.56±0.01	-
Fe X	190.00	0.51±0.02	0.59±0.02	0.57±0.03	0.57±0.02	-
Fe XII	192.39	0.60±0.01	0.65±0.01	0.65±0.03	0.65±0.02	-
Fe XII	193.52	0.40±0.01	0.43±0.01	0.41±0.01	0.46±0.01	-
Fe XII	195.12	0.42±0.00	0.42±0.00	0.41±0.01	0.46±0.01	-
Fe XIII	196.54	0.60±0.03	0.50±0.04	0.46±0.01	0.54±0.04	-
Fe XIII	200.02	0.51±0.01	0.54±0.03	0.53±0.01	0.57±0.04	-
Fe XIII	201.13	0.44±0.01	0.46±0.02	0.46±0.01	0.49±0.02	-
Fe XIII	202.04	0.44±0.00	0.45±0.02	0.47±0.00	0.47±0.02	-
Fe XIII	203.80	0.40±0.00	0.41±0.01	0.46±0.00	0.46±0.01	-
Fe XIV	211.32	0.52±0.02	0.49±0.02	0.50±0.01	0.52±0.52	-
		Line intensities (phot $s^{-1}cm^{-2}arcsec^{-2}$)				
Fe IX	171.07	2996±54	3372±60	3635±62	3538±57	3567±61
O VI	173.00	154±23	187±22	199±22	196±21	212±18
Fe X	174.53	2257±51	2453±59	2557±60	2487±54	2591±52
Fe X	177.24	1228±58	1561±54	1653±53	1599±48	1530±40
Fe XI	180.41	1993±46	2042±50	2259±54	2126±48	2192±48
O VI	184.00	147±14	188±15	121±16	184±15	261±18
Fe X	184.54	744±20	633±20	790±36	645±20	740±29
Fe XII	186.87	1189±23	1279±24	1319±37	1318±24	1300±37
Fe X	190.00	387±15	480±17	491±27	474±17	465±23
Fe XII	192.39	939±24	1042±25	1020±56	797±25	1005±33
Fe XII	193.52	1359±24	1418±25	1409±37	1427±26	1418±39
Fe XII	195.12	1809±27	1866±28	1883±41	1897±28	1872±44
Fe XIII	196.54	303±16	342±28	346±6	363±28	354±21
Fe XIII	200.02	270±5	284±20	290±5	292±21	275±19
Fe XIII	201.13	477±6	489±26	494±6	496±27	505±24
Fe XIII	202.04	851±8	939±36	980±9	970±38	981±33
Fe XIII	203.80	987±8	1266±38	1357±10	1327±40	1306±37
Fe XIV	211.32	615±26	748±30	798±29	786±786	764±29

derived from the smoothed spectra and those derived by the total sum of counts, with differences smaller than 5 % in most cases, with the only exception being lines shortward of 180 Å for which the double peaked profile is most pronounced. The smoothing procedures therefore all provide values close to the correct ones.

On the other hand, the results of the line fitting on a raw spectrum are such that intensities are usually reduced, with differences up to 25 %, showing how it is important to smooth the spectra before any fit is done and a gaussian fitting profile is used.

The agreement between the results obtained from each of the smoothed spectra is always better than 10 %. Only a few very weak lines show greater differences between the Fourier filtered spectrum and the other two due to strong background alteration. The line widths are also slightly different for the various smoothing procedures, while the line positions are very similar.

Unless otherwise stated, the smoothing adopted for the GIS data is a convolution with a gaussian profile of $\sigma = 2$ pixels.

3.2.2 Ghosts

For some lines, the cluster of photon events will tend to spread across to the neighbouring arms of the spiral. This happens when the width of the spiral is broadened by electronic noise. This effect tends to occur only in those regions where the spiral arms are close together, and can lead to spreading to one of the adjacent arms (or both). Now, once a set of LUTs is applied to the data on-board, i.e. a particular spiral pattern is assumed appropriate for the data, the original information is lost. In terms of counts versus wavelength, this means that a portion of the counts belonging to a line can be shifted into different parts of the telemetered spectrum, giving rise to spurious spectral lines if they fall in a spectral region void of lines, or providing extra intensity to already existing spectral lines. Henceforth we will refer to a spectral line whose intensity is enhanced in this way as *ghosted (or contaminated) line*, while the lines whose counts have been partially shifted toward other regions of the spectrum will be referred to as *ghosting (or parent) lines*. The counts shifted by this effect will be called *ghosts*, while the process will be called simply *ghosting*.

Since the spreading can only occur toward one or the other side of a spiral arm, each line can generate no more than two ghosts. When the spreading occurs toward the outer arm, a ghost is created at a lower wavelength, in the so-called red-shifted spectrum. Conversely, when part of the counts of a line are read into the inner arm, a ghost is created at a higher wavelength (in the so-called blue-shifted spectrum). Note that the definitions of red-shifted and blue-shifted GIS spectra do not have any relation to physical blue- or red-shifts, nor these spectra are simply 'shifted' (in fact, they are compressed or expanded in the wavelength scale). This notation, commonly used in GIS-related documentation, is simply used to indicate in which arm of the spiral ghosting occurs.

For each application of a given set of LUTs, ghosts will appear in the same positions. Once the applied LUTs are known, it is therefore possible to deduce which regions of the spectrum are unlikely to be affected by them, and to predict where ghosts might appear. It is therefore theoretically possible to *deghost (or reconstruct)* the spectra, i.e. add to each line the intensity lost by the creation of a ghost.

A large number of GIS spectra has been analysed, using software developed by the author, in order to assess the ghosting problem, since it severely affects any scientific use of the GIS spectra. Indeed, because of the ghosting problem, very few people have attempted any use of the GIS spectra, despite their great potential for plasma diagnostics.

Unfortunately, the situation is quite complex, for many reasons.

- First, different LUTs (i.e. spectra with different GSET_ID) produce different ghosting.

- Then, *there are no general rules that can be applied to deghost the spectra.*

  One example is that the boundaries of the regions where ghosts are expected to appear are not sharp, in the sense that there are ghosts that are created also in other regions. On the other hand, there are regions where ghosting is predicted to occur, but has not been observed. Another example is the fact that when ghosting occurs, it does in random proportions. Sometimes ghosts are only a few percent of the ghosting line, while in other cases they are much brighter than the parent line, i.e. almost all the intensity of the ghosting line appears in a ghost. It is therefore not possible to, say, analyse GIS spectra without correcting for ghosting, assuming some uncertainty level. Some lines appear to create two ghosts, while others only create one ghost. For the GSET_ID=42 case it appears that most of the lines produce red-shifted ghosts, rather than blue-shifted, although some produce both. The only positive note is that apparently only the brightest lines in each detector tend to create ghosts, even though it is difficult to exclude any ghosting of weak lines, masked in the noise of the spectra.

  Examples of ghosts, ghosting lines, contaminated lines, both contaminated and ghosting lines, red-shifted and/or blue-shifted ghosts, etc., and the possible reconstructions that were applied to the GIS spectra presented in this thesis are given in the rest of *this thesis in the form of labels in the spectra and in Tables. Note that although most of the ghosting in the GIS spectra has similar patterns for different GSET_IDs, the amount of it varies by large factors, and the examples provided here should only be used as an indication of where the problems are.*

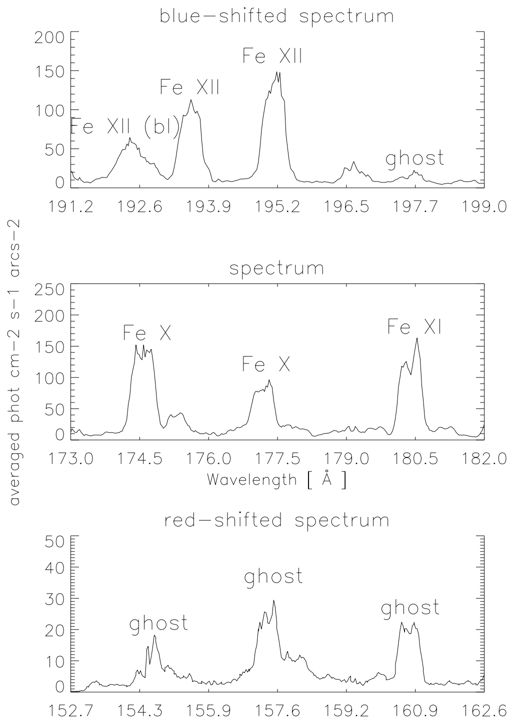

Figure 3.5: *A GIS 1 ghosting region.*

Only when a ghost appears in a region of the spectrum free of lines, is it possible to reconstruct the depleted line from which it came. Usually it is very difficult to distinguish between the ghost and any real lines with which it is blended.

For this reason only an extensive analysis of a large number of different GIS spectra can help in the ghost identification. An example of the sort of problems and how corrections can be applied, is given here. Figure 3.5 displays in the middle a portion (173-182.5 Å) of a GIS 1 spectrum. Using the geometry of the spiral pattern that was adopted to create the spectrum, the blue- and red-shifted spectra have been constructed from the observed spectrum. The spectral regions where ghosts were expected, in the blue- and red-shifted spectra, are displayed above and below the original spectrum, with the appropriate wavelength scale.

In this type of plot, a ghost would appear in one of the two shifted spectra at a position corresponding to where a line appears in the original spectrum. It is possible to see that the three spectral features observed in the bottom spectrum are *ghosts* of the three bright

Fe X 174.5 Å, Fe X 177.2 Å and Fe XI 180.4 Å lines. This is clear because no emission lines are expected to be visible in the 150–162 Å spectral region, for the type of source observed. It is therefore possible in this case to reconstruct the three ghosting lines, adding the ghosts' intensities to each parent line.

In the blue-shifted spectrum the ghosting problem seems to produce three contaminated lines: Fe XII 192.4 Å, Fe XII 195.1 Å and the Fe XIII 197.4 Å. In this case, a simple reconstruction is not possible. In fact, a great complication in the GIS spectra is that ghosted lines can be themselves the source of ghosts, ghosting into the very same region that created their contamination (*'cross-ghosting'*). In the example shown in Figure 3.5, the Fe XII 192.4 Å line can itself ghost into its red-shifted correspondent, i.e. contaminate the Fe X 174.5 Å line, increasing the confusion in this spectral range.

In conclusion, an examination of many GIS spectra has suggested the following method to try and tackle the ghosting problem in the GIS spectra. Initially, no correction to ghosting is made. [A different approach has been suggested by *E. Breeveld* (1998, priv.comm.), who developed CDS software to interactively move the intensities of 'presumed' ghosts (i.e. unidentified lines that appear in areas likely to be affected by ghosts) back to their parent line. The main limitation of the method proposed by *E. Breeveld* is that ghosts can be confused (or blended) with real emission lines. In any case, no correction should be applied to contaminated lines. There are many examples in which, depending on the type of solar source observed, ghosts can be blended with other real lines. Such examples are described in Section 3.4.6].

The presumed ghosts should then be treated as real lines, and their intensity measured. Then, a DEM analysis should be performed, using a selection of suitable lines. GIS synthetic spectra can then be created, and compared to the observed ones. This will immediately show the presence of the principal isolated ghosts, and will give an indication of the contaminated or ghosting lines. Ghost identification is also supported by the analysis of the position of the lines, in the original spectrum and in the blue- and red-shifted spectra. Examples will be given in Section 3.4.6. Corrections can then be applied to both the ghosting and ghosted lines. Even in the case of cross-ghosting, it is theoretically possible to apply some corrections, at least when the lines that cross-ghost are from ions for which an independent way of measuring their emission measure exists.

The drawbacks of this method are that it is time-consuming and that it relies on the accuracy of atomic physics and intensity calibration, that in some cases can have uncertainties of the same order as the ghosting. In any case, a complete reconstruction of the GIS spectra is not always possible. Note, on the other hand, that a blind exclusion of all the GIS lines possibly affected by a ghosting problem would leave only very few lines usable.

Table 3.3: *The coefficients for the GIS wavelength calibration, derived for two GSET_ID.*

	GSET_ID =42
GIS 1	151.23139, 0.031265225, 2.148844E-06, -7.9808423E-10, 2.0195808E-13
GIS 2	255.34898, 0.041980195, -2.6495787E-06, 1.3628225E-09, -5.8074565E-14
GIS 3	392.15063, 0.046712395, 7.634996E-07, -3.388151E-10, 2.2388279E-13
GIS 4	657.01778, 0.062105382, -6.019735E-06, 4.5349149E-09, -7.16958E-13
	GSET_ID =47
GIS 1	150.992, 0.0327321, -1.64271E-08, 3.75398E-10
GIS 2	256.491, 0.0412557, -1.44149E-06, 7.60522E-10
GIS 3	393.535, 0.0452287, 2.25383E-06, -3.88733E-10
GIS 4	657.343, 0.0599007, -1.78422E-06, 1.52401E-09

3.2.3 The wavelength calibration

The wavelength-to-pixel relation for the GIS spectra is a complex function, that depends on many factors. First, it depends on the slit used and on the LUT applied to convert the spiral pattern into a one-dimensional spectrum. Therefore, each GIS spectrum with a different GSET_ID number requires a different wavelength calibration. Also, the noise created by the electronics introduces distortions (*R. Bentley*, priv. comm.). Then, the wavelength calibration depends on the dispersion from the grating and the fact that the detectors are flat, and not curved, along the Rowland circle.

In the pre-flight calibration (*Bromage et al.*, 1996; *Lang et al.*, 1999) a quadratic relation for the wavelength calibration was assumed. Early in-flight spectra were fitted for different LUTs to obtain a revised set of quadratic wavelength calibrations (*B. Bromage*, priv. comm.) and these are available in the CDS software. This quadratic relation is sufficiently accurate for the central parts of the detectors, but is increasingly inaccurate toward the edges of all the detectors, reaching offsets of more than 1 Å, an unacceptably large value.

The above-mentioned complexity of the GIS wavelength calibration makes any attempt to describe it in terms of a polynomial very difficult. However, for simplicity in the data analysis, and since high accuracies are unattainable, given all the other complications in terms of line profiles, polynomial fits to various datasets have been made. Table 3.3 presents the coefficients that were found by the author, and that have been applied to the GIS observations presented in this thesis. These coefficients give reasonable accuracies (usually to better than one-half the resolution) over the whole detectors.

3.2.4 The intensity calibration

As for the NIS case, there are several factors which determine the conversion of the data to absolute units.

1. The absolute sensitivity $ef(\lambda)$ [counts/photons] as a function of wavelength, which is a combination of the efficiencies of the optics, grating, and detectors. As in the NIS case, intensity calibrations were obtained on the ground for a limited number of lines within each detector (see Figure 3.30). To refine this, and to determine post-launch changes, an in-flight calibration was required. More details can be found in Section 3.4.10.

2. The telescope aperture A_t [cm^2]. Contrary to the NIS case, there is no measurable variation with the scan mirror position (*Bromage et al.*, 1996). In any case, even if some dependence were present, it would be negligible, because the GIS rasters are in most cases very small (i.e. the scan mirror is moved only few times). An averaged value of 25.5 cm^2 is adopted.

3. The geometric area available at the slit, which depends on which slit is used.

4. The exposure time, which is measured accurately and only needs a small correction for dead times.

Software to calibrate the GIS spectra in intensity was written by the author.
Note, as in the NIS case, that unless stated otherwise: all the GIS spectra presented in this thesis are in 'corrected' counts, or counts/s; the spectral line intensities in the Figures are in phot s^{-1} cm^{-2} $arcsec^{-2}$; the intensities in the Tables are in ergs s^{-1} cm^{-2} sr^{-1}; the intensity ratio values, both in Tables and in Figures, are obtained from the intensities in ergs s^{-1} cm^{-2} sr^{-1}, and therefore, for clarity reasons, are indicated as 'ratio values (ergs)'. The errors in the intensities do not include all the systematic errors that can come from all the correction and calibration factors above-mentioned of which the main ones are: the error in the instrument sensitivities, discussed below; contaminations due to the ghosting problem.

3.3 The first-light GIS observations

Table 3.4 lists some of the main characteristics of the first-light observations that were analysed. Single spectra were extracted, averaging the total number of exposures in each observation. Figures 3.6, 3.7, 3.8 show the averaged spectra of these observations. Spectra are smoothed over 3 pixels, to reduce the fixed pattern. Note the large differences in the spectra (that are plotted on different scales), in terms of both absolute intensity and the relative intensities between lines emitted by different ions, which clearly indicates completely different temperature distributions.

Second order lines were found to be present in GIS 3 and GIS 4, and are particularly prominent in the active region spectrum. The spectra have been calibrated in wavelength and in intensity, and a multiple gaussian line fit (with a linear background) was performed using standard IRAF programs, to deduce line intensities.

Table 3.4: *The GIS first-light observations. The type of observed region, the CDS fits file name, the day of observation, the slit used, the number of exposures of the rasters (averaged), the exposure time, the GSET_ID number, and the type of observation are displayed.*

Region	file	day	slit	# exp.	t exp.	GSET_ID	type
Active (AR)	s110r00	28/02/96	$2''$x$2''$	50	10s	19	first light
Quiet Sun (QS)	s132r00	04/03/96	$2''$x$2''$	225	50s	22	spectral atlas
Coronal hole (CH)	s90r00	25/02/96	$2''$x$2''$	20	500s	16	first light

The ground-based calibration for GIS was used as a starting point, but some variations in the sensitivity of the GI detectors were expected to have occurred since launch, so it was important to check them, and to assess the values for the second order sensitivities.

The adopted sensitivities for the first order (second order) were: GIS 1: 1.4e-4 (1.4e-5); GIS 2: 2.4e-4 (2.4e-5); GIS 3: 3.4e-4 (2.7e-5); GIS 4: 0.5e-4 (1.e-5). These values were deduced comparing the intensities of density-insensitive lines emitted by the same ion and observed in different detectors. These results were preliminary. In particular, no wavelength-dependent effects were considered. To help with the complex identification of the lines, check the calibration and the contribution of the second order lines, a differential emission measure analysis was performed. The Arcetri inversion technique (*Monsignori Fossi and Landini*, 1991) and the CHIANTI (version 0.9) database were used in order to deduce the differential emission measure . The continuum (visible in the GIS 4) was calculated with the Arcetri code, with the *Feldman et al.* (1992b) abundances and a log N_e=9. Densities of the three spectra were estimated mainly using Fe XIII 203.83 Å / 202.04 Å, and the contribution functions were therefore calculated at the following constant pressures: $1 \cdot 10^{16}$ (AR);$2 \cdot 10^{15}$ (QS); $1 \cdot 10^{14}$ (CH).

Adjustments were made to the elemental abundances to obtain consistency among spectral lines from different elements. The photospheric (*Grevesse and Anders*, 1991) abundances were used to deduce the DEMs for the coronal hole and quiet sun observations, with the following element abundances varied (values are log differences from the starting values): C (+0.6), N(+0.3), O(+0.2), S(+0.5) for the quiet sun observation; C (+0.7), N(+0.3), O(+0.25), Ne(-0.05), S(+0.5) for the coronal hole observation. The coronal (*Feldman et al.*, 1992b) abundances were found more appropriate for the AR observation. The following element abundances were varied (values are log differences from the starting

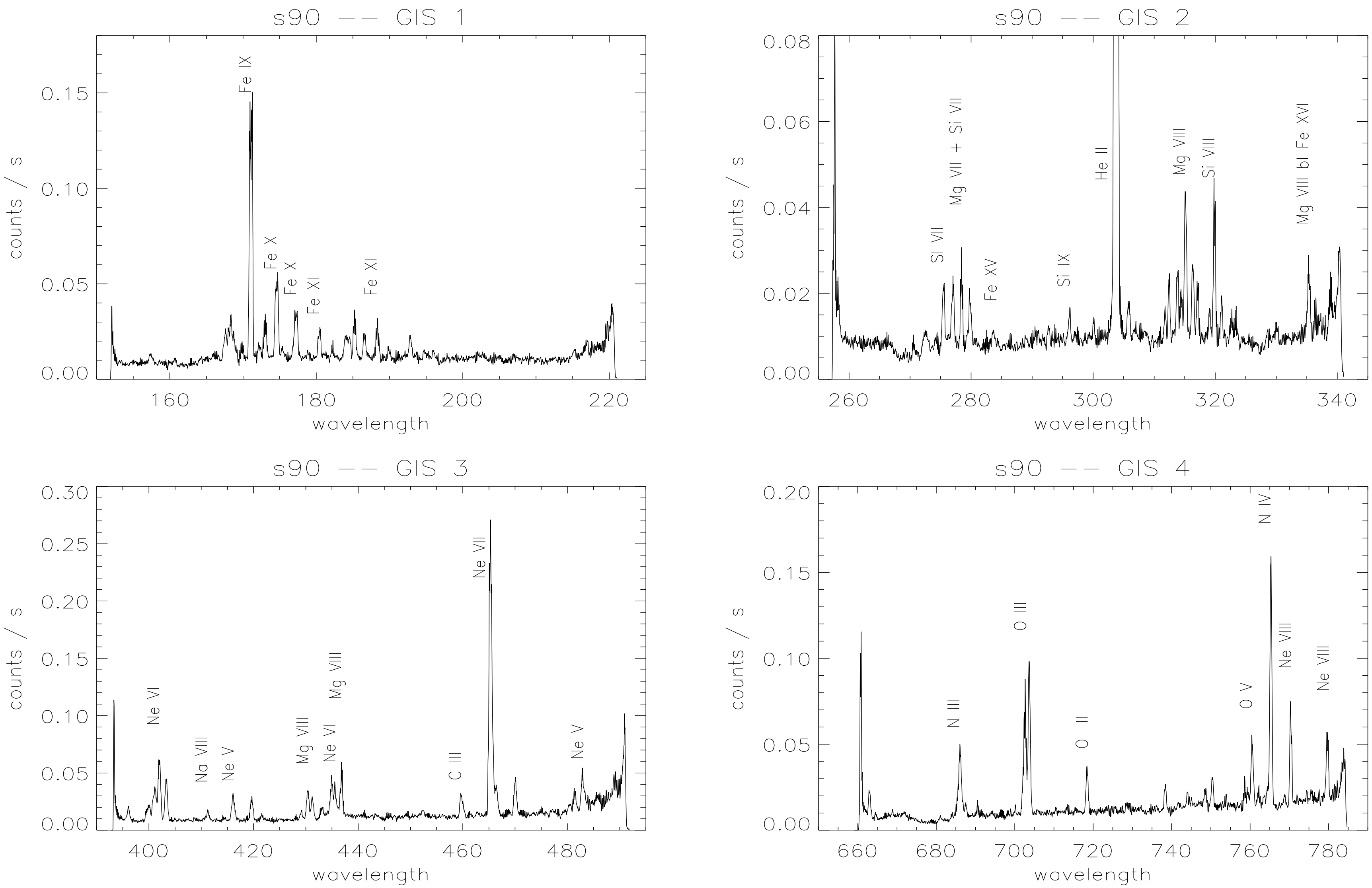

Figure 3.6: *The first light GIS spectra of a coronal hole (s90)*

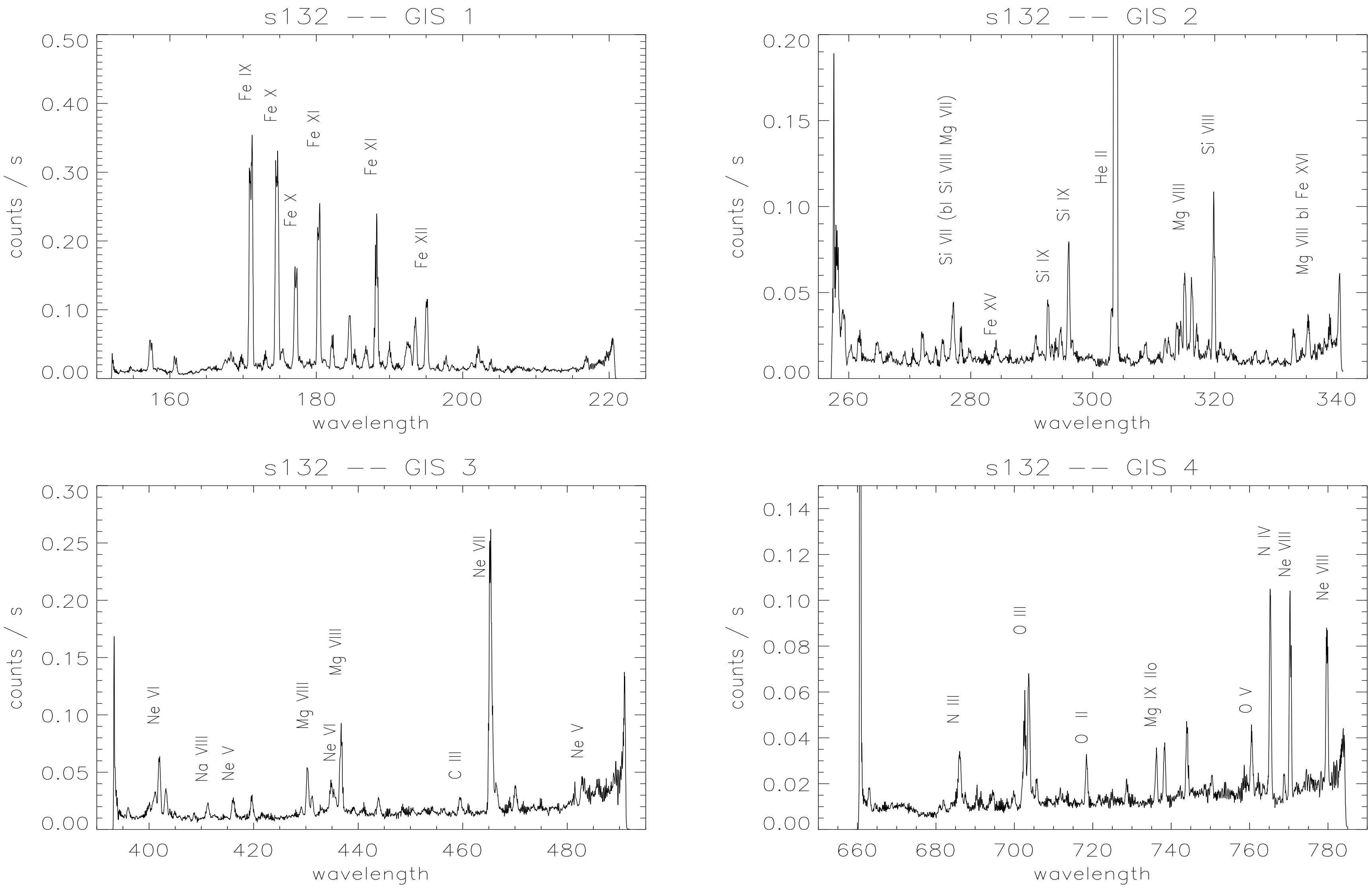

Figure 3.7: *One of the first series of GIS spectra of a quiet sun (s132) region.*

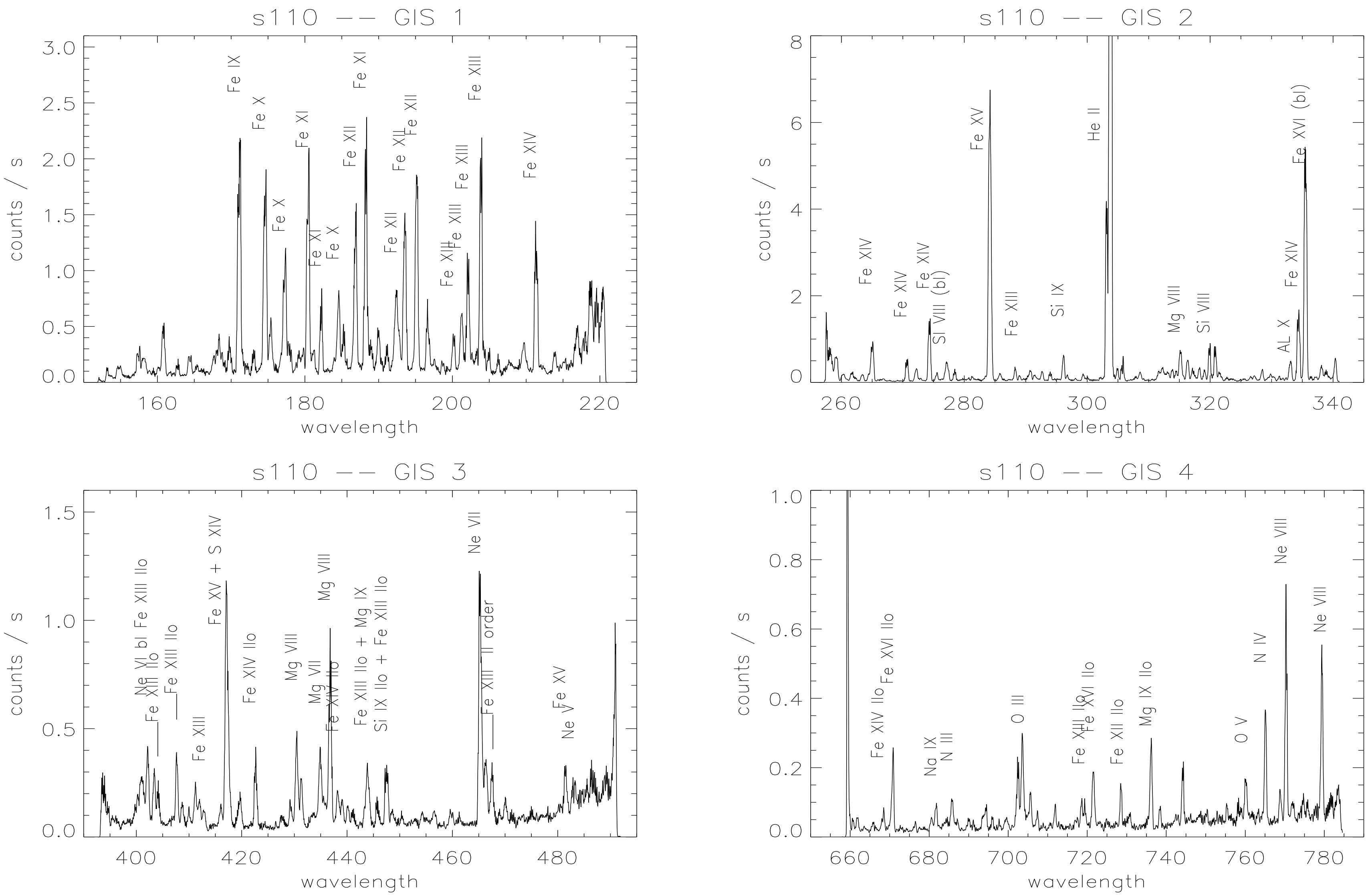

Figure 3.8: *The first light GIS spectra of an active region (s110).*

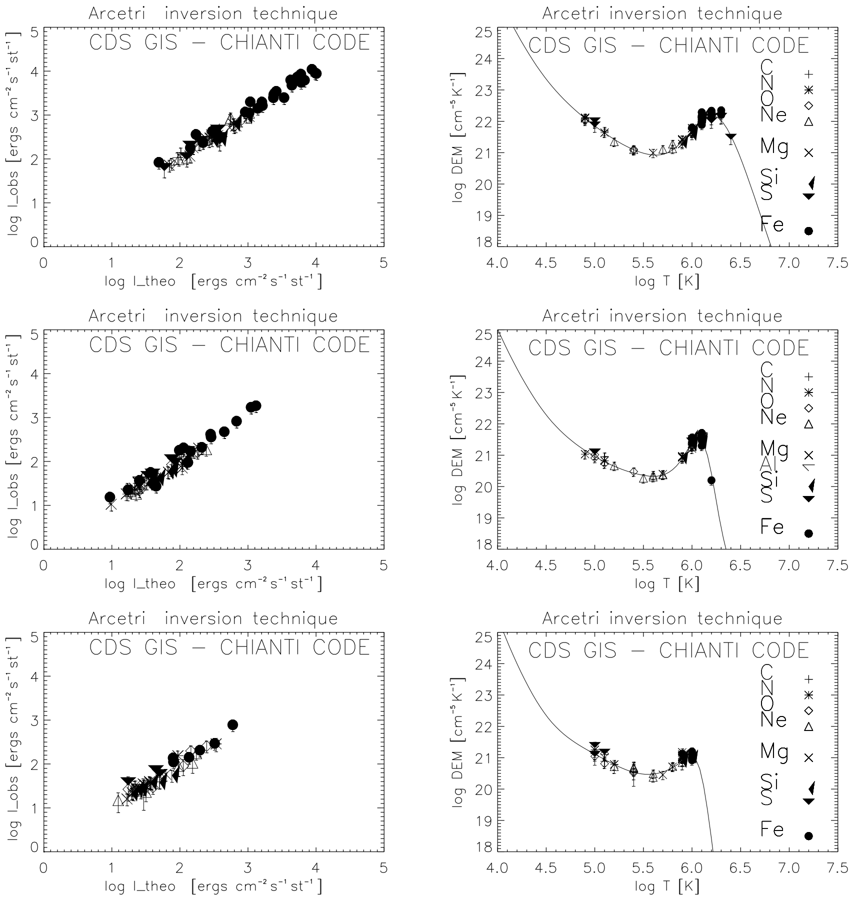

Figure 3.9: *The derived DEMs (right hand plots) and comparison of observed ($LogI_{obs}$) and theoretical ($LogI_{theo}$) intensities (left hand plots) for an active region, the quiet Sun and a coronal hole. (top to bottom).*

values): C (+0.6),N(+0.1),S(+0.1).

The DEM analysis shown in Figure 3.9 confirms a difference between the elemental abundances of different regions. The low temperature region (Log T $\sim$ 4.5) is constrained by the continuum, which is seen at longer wavelengths. The high temperature region (Log T $\sim$ 6.5 - 7) is constrained by the absence of high temperature lines. The highest temperature lines used (from Fe XV, Fe XVI and S XIV), were visible in the quiet Sun and active region spectrum, and were used to determine the drop in the DEM at high temperatures. We note that the DEM falls rapidly in the coronal hole spectrum. This is constrained by the lack of any Fe XIII lines - in particular the lines at 202Å and 203.8Å and any other higher Fe ionization stages.

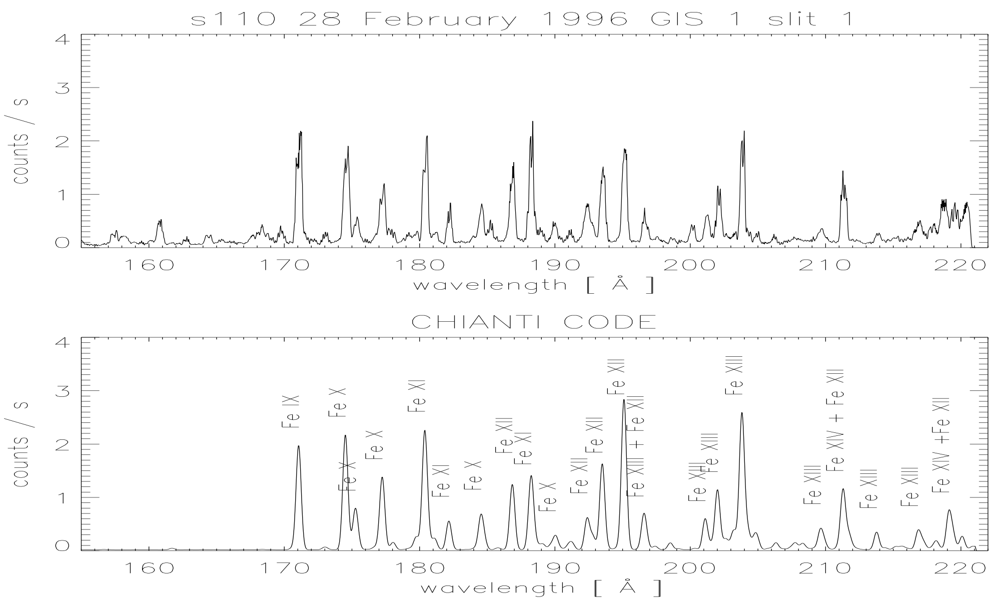

Figure 3.10: *The observed (top) and synthetic (bottom) GIS 1 spectra of the active region observation.*

With the adopted DEM distributions and calibration values, most of the spectral lines have a 30-40% agreement between the theoretical and observed intensities (see the left hand plots of Figure 3.9). Synthetic spectra of the three regions were then created, including the second order lines and the continuum. In Figure 3.10 and Figure 3.11 we show as examples, comparisons of the observed and synthetic spectrum for the active region spectrum for the GIS 1 and GIS 3 wavelength bands. The GIS 1 wavelength band is dominated by a sequence of iron lines from Fe IX - Fe XIV. These are well reproduced by the CHIANTI synthetic spectra. The GIS 3 spectrum is also well represented, with many second order lines, some of which are blended with first order lines.

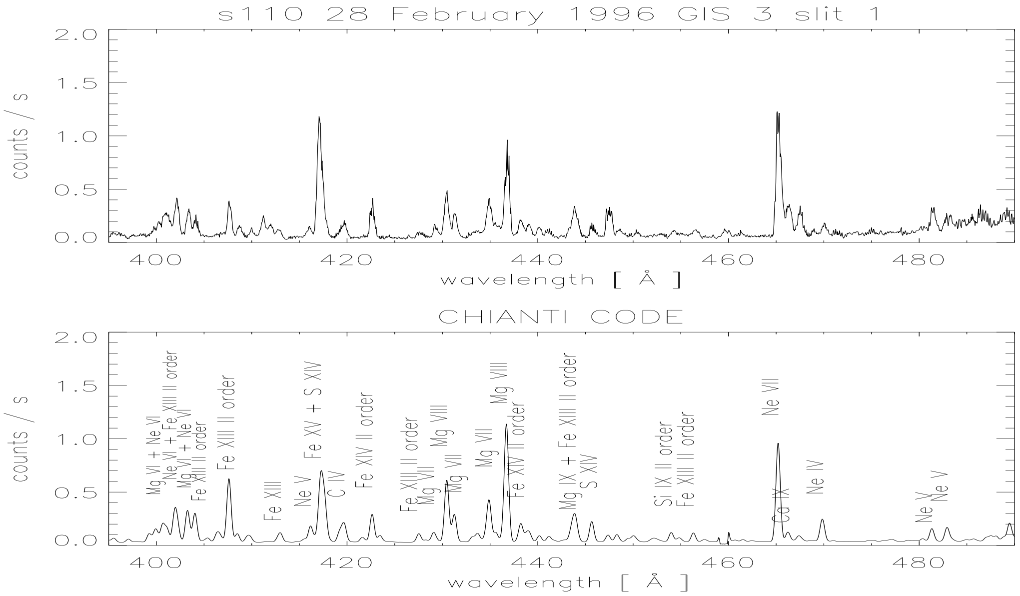

Figure 3.11: *The observed (top) and synthetic (bottom) GIS 3 spectra of the active region observation.*

3.4 The calibration of the CDS instrument

Intensity calibration is a fundamental requirement for any scientific use of spectral data, but obtaining such information is not an easy undertaking in the extreme ultraviolet spectral range. A history of the CDS calibration is now summarised, to clarify this important issue.

- A pre-flight calibration was performed (*Bromage et al.*, 1996), producing an absolute calibration for both NIS and GIS. However, these measurements did not provide the full relative sensitivity function along each NIS and GIS detector. It provided an initial measure of the mean sensitivity of each detector and a basis for absolute calibration of the instrument.

- The *Bromage et al.* (1996) values, together with a theoretically derived wavelength dependence and a preliminary correction (based on in-flight measurements), produced the sensitivities stored for public use in the CDS data analysis software until December 1998. This NIS calibration will be referred as the the *NIS first standard calibration*. It is shown in detail in Figures 3.28, 3.29, and discussed in Sections 3.4.8 and 3.4.9, below.

- The NIS first standard calibration was found to require corrections by various authors (see, e.g., *Landi et al.*, 1997a), the main one being the need to increase the NIS 1 sensitivity, relative to NIS 2, by some factor. *Landi et al.* (1997a) proposed a factor between 2.5 and 5. Note that such *large uncertainty* in the NIS 1/NIS 2 calibration significantly affects the determination of the FIP effect (because the diagnostic lines are observed by different detectors). It can also affect emission measure (or DEM) analysis, since almost all low-temperature lines are seen in NIS 2, while most of the high-temperature lines are observed only in NIS 1.

- An in-flight cross-calibration between the NIS and a rocket flight launched in May 1997 has recently been presented by *Brekke et al.* (1999). This study has produced *absolute* values of the NIS sensitivities, for both NIS 1 and NIS 2. For NIS 2, it was possible to estimate a coarse wavelength-dependence (which turned out to be different from the predicted pre-flight one, see Figure 3.29 in Section 3.4.9 below). For NIS 1, only one reliable measurement at one wavelength was possible (see Section 3.4.8 below for a discussion).

- A revised pre-flight calibration for both GIS and NIS has recently been presented (*Lang et al.*, 1999). This revised pre-flight calibration (see Figures 3.28, 3.29, for NIS and Figure 3.30 for the GIS values, and discussion below) suggests a different

NIS calibration, both in *absolute* and relative (between NIS 1 and NIS 2) terms. The revised value of the absolute sensitivity at 584 Å(NIS 2) is in agreement with the in-flight value of *Brekke et al.* (1999). The other values are not.

- A *NIS second standard* calibration, based on the results of *Brekke et al.* (1999) and *Lang et al.* (1999) was proposed in December 1998 and implemented in the CDS data analysis software. It is also shown in Figures 3.28, 3.29, and discussed below.

- No measurements (except for a pre-flight one) of the second order NIS 2 sensitivities were available. It will be shown here how many second order lines are seen in NIS 2.

- No measurements of the GIS second order sensitivities were available. Most of the observed lines in GIS 2 and GIS 3 are either second order lines or blends with second order lines.

- No GIS standard calibration was provided in the CDS data analysis software (until recently).

It should be noted that the uncertainties in the pre-flight calibration ($\sim$ 15%) and in the cross-calibration work of *Brekke et al.* (1999) [$\sim$ 15-25%] are relatively large, and moreover only limited wavelength dependence has been sufficiently measured for the NIS 1 channel, which is most important in terms of diagnostics. Also, the ground calibration may not be directly applicable to the in-flight observations, for many reasons:

- The pre-flight calibration was based on spectra taken on the ground nearly two years before launch (in March 1994). A comparison with the CDS spectra taken in-flight shows that the CDS instrument has suffered many changes, probably during launch, that have already been mentioned. The main ones are lower resolution for both NIS and GIS, and a large scattered light contribution in the NIS 1 channel.

- The detectors on the ground were illuminated by a narrow-beam calibration source, while in-flight they are fully-illuminated by the Sun.

- Because of the presence of MCPs in both the NIS and GIS detectors, a decrease in their sensitivity was expected, due to the exposure to solar radiation, in particular during the first few months of operations (which in fact has been observed).

- The same exposure to solar radiation, produces effects that change the detectors' characteristics with time, known as the long-term gain depression (i.e. the burn-in in the bright NIS lines).

- Other important variations in time are related to a decreased reflectivity of the telescope's mirrors, the scan mirror and the gratings, which can be due to deposits on the various surfaces and can cause decreased sensitivities for all the CDS detectors. Such effects have become even more evident in the recent CDS spectra, after the dramatic SOHO loss of contact in 1999.

From all the above, it is clear that *an in-flight calibration of all the CDS detectors was necessary*, and in the absence of any on-board equipment, the only possibility was to use the solar emission as the calibration source (which causes a lot of problems, as described in Section 3.4.6). The aim of the work presented here was to find a relative calibration that could represent most of the brightest lines observed in all the CDS detectors within a 20-30% accuracy.

The CDS *absolute* intensity calibration is not the main concern here, since a change in the absolute intensity calibration would merely have the effect of changing the scaling of quantities such as the DEM values. What is important is to find the *relative* intensity calibration, i.e. the intensity calibration as a function of wavelength for the various channels. In fact, most of the diagnostic lines fall at different wavelengths and a different calibration has the effect of changing absolute values of densities, temperatures and element abundances.

In all the following work it will be assumed that all the above-mentioned factors that contribute to the intensity calibration of both NIS and GIS are correct and do not vary in time (a reasonable assumption), while all the relative values of the sensitivities will be allowed to vary and deduced from in-flight observations. An absolute reference point for the sensitivity was chosen at the He I 584 Å line $ef = 4.75\text{x}10^{-4}$ *[counts/photon], in accordance with the* Lang *et al. (1999) and* Brekke *et al. (1999) values. All the other values of the sensitivities, for both the NIS and GIS channels, and for the first and second order, have been obtained relative to that point, using the diagnostic method. The results are shown in Figure 3.30. These calibration values are used throughout this thesis, unless explicitly stated otherwise.*

3.4.1 The diagnostic method for the CDS calibration

The diagnostic method

The best way to find the relative intensity calibration (and any changes with time), is to compare the observed intensities (taken at different times) with theoretical values, for those groups of lines whose ratios are expected to be independent of the observed source. The calibration is adjusted in order to obtain agreement between the observed and theoretical intensities.

First, ratios of lines emitted by the same ion are examined. The results are therefore independent of the element abundance *and* the thermal distribution along the line of sight of the source (i.e. the DEM values). The first ratios to examine are branching ratios (i.e. ratios of lines that share a common upper level), that are equal to the ratios of the radiative transition probabilities, which are well known. Then, ratios of density-insensitive lines are also used. For each ion, in fact, there are groups of transitions, usually originating from the same upper level, that have nearly the same density dependence so that any ratio formed from these lines is density-independent.

The procedure is then applied to all the other observed lines, examining ion by ion, to obtain a relative calibration over the entire wavelength range. When agreement is found between the results obtained by the use of many lines of different ions, one can be sure that the calibration is correct. In order to make full use of this diagnostic method for calibration purposes, given the uncertainties in the atomic data and the observed intensities, it is essential to use as many lines emitted by the same ion as possible.

This method is not new, and has already been applied a few times in the past. For example, *Neupert and Kastner* (1983) apply this method for an in-flight calibration of the OSO V and OSO VII EUV spectrometers, in the 150-400 Å range. Recently, this method was successfully applied (*Brosius et al.*, 1998b) to calibrate the Solar EUV Rocket Telescope and Spectrometer observations in 1995 (SERTS-95), using averaged active region and quiet sun spectra, and CHIANTI (version 1.01, except for Fe XIV). SERTS-95, compared to the previous SERTS flights, had an enhanced second order sensitivity and recorded high-resolution (0.03 Å) spectra in the 171-225 Å range in second order and in the 235-335 Å range in first order.

Applicability of the method

A large effort was spent for this thesis on calibration issues, analysing and planning new CDS observations in order to apply the calibration method. This was needed since the coronal hole spectra are not suitable for calibration purposes, because of the low signal. There is no space here to describe all of them, and only examples will be given. Table C.1 presents a list of some of the observations designed by the author, together with B. Bromage, for calibration purposes.

Many NIS and GIS observations of different solar regions have been analysed, and the calibration method applied. These are the main reasons:

- the need to observationally assess the blending of the lines, for all the CDS channels. In fact, as it will become clear, many 'calibration' lines are blended with other lines, and only by observing completely different regions, can the contributions from the blending lines be ruled out, without having to rely on theoretical predictions to remove the intensity of the blending line. For example, the bright 610 Å line is a strong blend of Mg X and O IV transitions, and only in off-limb observations does the O IV contribution become negligible. Many of these cases are present in the NIS spectra, and will be described in detail.

- The need to independently assess ghosting in the GIS spectra. For example, a ghost will disappear if the parent line does, as low-temperature lines do in off-limb observations. In other cases it is difficult to assess the presence of a ghost because it contaminates a line, and it is only when this line is not emitted by the observed solar region (again a cool line in off-limb observations, for example), that the observed 'line' can be identified as a 'pure ghost'. Examples of all these cases will be given.

- The need to assess the importance of the 'background' intensity in the NIS and GIS spectra. As mentioned, in the NIS spectra this component is mainly due to scattered light and disappears in off-limb observations. In GIS spectra, the main background component is due to true He and H continua, which also disappear off-limb.

3.4.2 Layout of the rest of Section 3.4

In order to help with the complexity of line identification, test the latest atomic data available, and to find which 'calibration' lines are suitable for the CDS calibration, a complete DEM analysis has been performed on the SERTS-89 observation (*Thomas and Neupert*, 1994). This is presented in Section 3.4.3.

Many GIS observations have been analysed to study the GIS peculiar characteristics. Only some examples will be given in this thesis. A GIS detailed study of two different observations was performed, to give a preliminary assessment of the ghosts and to check the pre-flight relative intensity calibration of the GIS channels. This work contributed to the published work of *Landi et al.* (1999a), and is briefly described in Section 3.4.4. In the same Section, a revision of that work (using more recent atomic data) is also presented.

Many NIS observations, on disc and off-limb, were analysed, for the internal calibration of the NIS detectors alone. They are described in Section 3.4.5.

One of the main outcomes of the above-mentioned analyses has been the realisation that for both NIS and GIS instruments only a few reliable (i.e. not blended, not affected by instrumental effects or atomic physics problems) calibration lines emitted by the same ion are observed in each detector. Actually, only for a few detectors is it possible to produce at least two values of the sensitivity. This strongly limits the application of the diagnostic method for calibration purposes. *The potential of the diagnostic method is therefore achieved only when all the NIS and GIS detectors are calibrated at the same time, with the use of the full CDS wavelength range.*

In a detailed survey, all the available CDS observations, including those that were made for the purpose of calibrating the CDS against other instruments (including rocket flights), were found to be unsuitable for a proper application of the diagnostic method, and hence for a cross-calibration of the CDS detectors. This was for many different reasons (e.g. low S/N, paucity of extracted NIS lines, temporal variability of the solar region observed, lack of sufficient spatial overlapping region between the NIS and the GIS rasters, due to solar rotation).

Since NIS and GIS detectors do not observe simultaneously, special NIS-GIS observing sequences were therefore carefully planned, executed and analysed by the author and B. Bromage. These are described in Section 3.4.6. Most of these observations were performed at the solar limb. Section 3.4.6 also presents some examples of the analysis that was done to assess any time variability of the relative CDS calibration during 1997. The constancy in time and space of the ratios of the lines selected for calibration is also illustrated with some typical examples. These NIS-GIS sequences were used for both internal NIS and GIS calibration, and in particular for the cross-calibration of all the CDS detectors. Some results are already presented in Section 3.4.6.

Among all the NIS-GIS observations analysed, two have been selected as examples for the following Sections, to be used not only for calibration purposes but also to present for the first time typical NIS and GIS near-simultaneous spectra of the quiet sun. They are an on-disc (October 16 1997) and an off-limb (May 4 1997) observation, extracted from two series of NIS-GIS observations at the solar limb.

Although most of the calibration lines used here have only a minor dependence on density and temperature, some sensitivity is still present, and is therefore important to calculate the contribution functions of these lines at the correct density (or pressure). The values of densities and temperatures of the two regions selected as examples are presented in Section 3.4.7, where it is also shown that the use of a different calibration does not significantly affect the derived values.

Specific software was written by the author in order to apply this calibration method to CDS observations. This method, given the complexity of having 9 different wavelength regions (including the second order, and with only a few pre-flight measurements for some of them) to cross-calibrate at the same time, has been applied in stages, taking into account many different observations.

There is no space here to describe all the various steps in great detail. However, a description of how the method has been applied to assess the NIS 1 internal calibration (Section 3.4.8) and then the NIS 2 first order internal calibration (Section 3.4.9) is presented. These internal calibrations are completely independent.

Then, all the NIS and GIS channels, including the second orders, have been calibrated against each other, using the diagnostic calibration method. Some of the lines used for this cross-calibration are described in detail in Section 3.4.10, where the final results are presented and compared with the other calibration studies.

Finally, the DEM analyses of the two example observations are presented, and used to illustrate a series of points. First, the off-limb DEM analysis is presented in Section 3.4.11. The relatively simple plasma structure (almost isothermal) of this observation allowed discrepancies between lines emitted by different ions to be highlighted. This is used for a double purpose. First, it shows that the most up-to-date second NIS standard calibration fails to represent some of the observed lines well, and at the same time confirms the calibration presented here. Secondly, it shows how different ionization equilibrium calculations affect the calculated intensity of the lines. The full line lists and identification of the lines is then presented. This also confirms that the calibration presented here explains most of the observed emission. The DEM analysis of the on-disc observation of October 16 1997 is finally presented in Section 3.4.12, together with a full line list of the identified lines.

3.4.3 The SERTS-89 spectrum

The active region SERTS-89 observation (*Thomas and Neupert*, 1994) has represented a landmark in EUV solar spectroscopy for several years. Unfortunately, *Thomas and Neupert* (1994) presented line identifications based only on the positions of the lines, and misidentified some of them. *Del Zanna et al.* (1996) produced a differential emission measure analysis using some ions of different elements. *Brickhouse et al.* (1995) also presented a differential emission measure analysis, but based only on the Fe ions, while *Young et al.* (1998) have recently corrected and introduced new line intensities and identifications, comparing observed and theoretical line ratios, ion by ion. *Dwivedi et al.* (1998) have presented a list of diagnostic lines, based on the SERTS-89 spectrum.

Since most of the lines present in the SERTS-89 list are also visible in the CDS spectrum, the SERTS-89 observation, with its high spectral resolution and quality, has been used here to help the identification and blending of some of the CDS lines, and to assess the quality of the atomic data used subsequently to calibrate the CDS instrument.

The calibrated intensities of *Thomas and Neupert* (1994), plus those of *Young et al.* (1998) have been used together with CHIANTI v.2 (including the recent Fe XIV calculations by *Storey et al.*, 1999). A DEM analysis was performed on all these lines, and a full line list of this spectrum, with identifications based on a DEM method, is presented here for the first time. The contribution functions have been calculated at constant N_e = 2x10^9 cm^{-3}, using the *Arnaud and Rothenflug* (1985) ionization equilibrium (for all the ions) and photospheric abundances (*Grevesse and Anders*, 1991), except for the following elements (with logarithmic differences from the photospheric values indicated in parentheses): Na (+0.3), Al (+0.3), S (-0.4). It is to be noted that a need for an increase in the Al abundance, relative to the other low-FIP elements, was also found by *Falconer et al.* (1997).

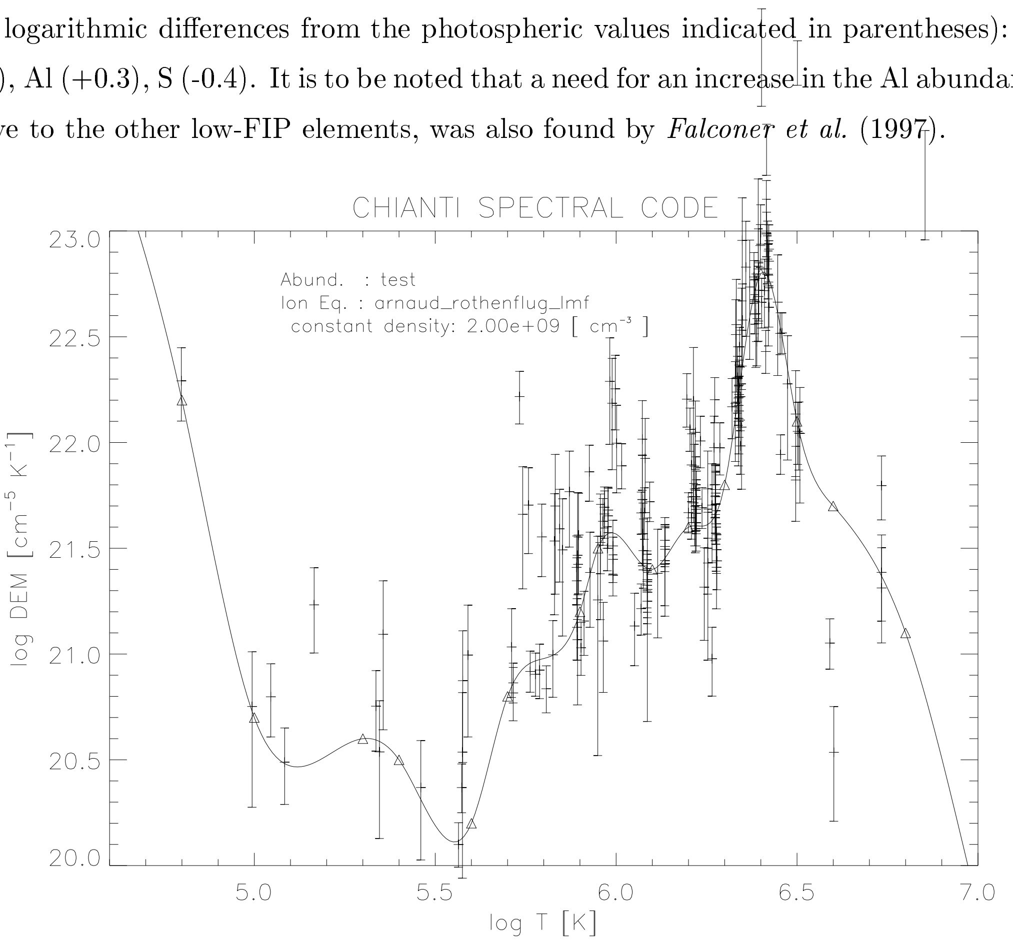

Figure 3.12: *The derived DEM for the SERTS-89 active region spectrum.*

Figure 3.12 shows the derived DEM which is well constrained at high temperatures. Table A.1 presents the results for all the lines that have been identified, ordered in temperature. In most cases, agreement with the corrections and new identifications presented by *Young et al.* (1998) was found. However, some new identifications, or corrections to inaccurate ones (even at the high resolution of SERTS, blending is still present in some cases) are presented in Table A.1. The fact that the majority of the lines, including Fe XIV, are well reproduced (within 10%) confirms the high quality of the atomic data. The new Fe XIV calculations evidently solve a long-standing problem with the Fe XIV lines (see e.g. *Young et al.*, 1998 and references therein).

Many lines are not so well reproduced, but this can be simply explained in some cases. For example, when lines are density-dependent. In fact, a single averaged density fails to reproduce all the density-sensitive lines, as already shown by all the previous studies of this spectrum. Furthermore, no particular trend, as a decrease with the temperature of formation of the ions, can be found. Another example is for the lines that were seen in second order, where the calibration was more uncertain. *Young et al.* (1998) propose a correction (up to a factor of 2) in the calibration at wavelengths above 400 Å. The analysis presented here confirms a need for a correction, but at longer wavelengths, above 430 Å, as constrained by Mg VIII, Mg VII, Ne VI lines. It should be noted that if the correction proposed by *Young et al.* (1998) is applied, then all the Mg IX lines around 440 Å would no longer be in agreement with the bright Mg IX 368 Å line. The lines of C IV and Ar XVI are underestimated and overestimated by large factors, a confirmation of the problem with the Li-like ions, introduced in Chapter 2.

Other groups of lines are in disagreement as a whole, as is the case of the Mg V lines, which are in agreement among themselves, but not with all the other lines. This disagreement can not be due to an element abundance problem, since the the other Mg lines are well represented. For example, the Mg VI lines are in excellent agreement with the Ne VI lines, confirming that for that active region spectrum there was no FIP effect. Finally, many other single lines are not well represented, and for which a change in the smooth calibration adopted by *Thomas and Neupert* (1994), or variations of element abundance with height, or a different atomic physics, would be required.

Some of the peculiar characteristics found from the analysis, can be ascribed to the complexity and inhomogeneity of the large region where the average spectrum was obtained. It is therefore important to keep in mind that for calibration purposes it is best to observe a simple region, possibly having uniform characteristics, such as temperature and density.

3.4.4 A GIS internal intensity calibration study

GIS spectra of an active region and of a region of quiet sun were analysed, in order to apply a new *L-function* diagnostic technique, already used for a preliminary NIS calibration *Landi et al.* (1997a). This plasma diagnostic technique has been used to check the pre-flight relative intensity calibration of the four GIS windows. The analysis of the observations was also used to assess the in-flight characteristics of the GIS detectors. This work was done in collaboration with E. Landi, and has led to the *Landi et al.* (1999a) paper, where details can be found. Here, only a brief description of the analysis is given. This work led to the selection of a number of lines which were found not to be significantly affected by ghosting, and so could and so can be reliably used for plasma diagnostics with GIS in further studies.

The active region spectrum has been re-analysed for this thesis, by the author, using new atomic data and different ionization equilibrium calculations. This re-analysis is described below, since this spectrum was also used to assess the GIS new calibration presented below.

The GIS study presented in *Landi et al.* (1999a)

The Arcetri Spectral Code (*Landi and Landini*, 1998a) was used for this data analysis. The ionization equilibrium of *Arnaud and Raymond* (1992)has been adopted for the iron ions, while the *Arnaud and Rothenflug* (1985) data were used for the other elements and those of *Landini and Monsignori Fossi* (1991) for the minor elements.

Two full spectral GIS atlases were analyzed, one emitted by a solar active region (AR), and the other in quiet sun (QS) conditions. Both of them were obtained by rastering over a $30''$x$30''$area on the solar disk with 15 mirror positions and 15 slit positions using the $2''$x$2''$slit. For each of the resulting 225 exposures of both sets of spectra the exposure time was 50s. The quiet sun observation was obtained between 18:26 UT and 21:38 UT on September 2nd 1996. The corresponding data file for this observation is s4552, and its GSET_ID number is 41. The active region spectrum was taken after the quiet sun observation, starting at 22:42 UT and ending at 01:54 UT on September 3rd 1996. Its GSET_ID is 47. The data file for the active region observation is s4554. It is important to keep in mind that the spectra analysed had GSET_ID=41 and 47 and therefore the ghosting analysis that allowed a selection of usable lines to be made can in principle only be applied to other observations having the same GSET_IDs. The two spectra were taken on the same day in order to eliminate any possible long term time variation of the GIS intensity calibration between one observation and the other, so that the results obtained from the two spectra could be directly compared.

Spatially averaged spectra were formed, in order to increase the signal to noise ratio. Monochromatic images of the rastered areas on the Sun were obtained by summing up the pixel intensities of the brightest lines. These were examined for inhomogeneity in the emitting regions, before spatially averaging the spectra. This is necessary because, as noted by *Landi et al.* (1997a), the L-functions will cross each other only if the emitting plasma is homogeneous. If there are inhomogeneities it is possible that some departures of the L-functions from the expected behavior may occur due to lines emitted in different solar conditions, making it more difficult to determine possible intensity calibration problems.

The emission appeared fairly uniform over the QS region, and there was no evidence of significant inhomogeneities, while the AR images showed large variations in the intensity in the hottest lines, revealing a very complex morphology, the structure varying with temperature. A map of the intensity ratio of two Fe XIII strongly density-sensitive lines 202.0 Å / 203.8 Å also indicated considerable variations in electron density. As a result, only an area with a restricted range of density values (Fe XIII ratio values between 1.2 and 1.4) was used to form an average AR spectrum. This selected region broadly covered the hottest part of the total emitting area, and had an averaged electron density $\simeq 10^{9.4}\ cm^{-3}$.

This preliminary study of the spectra was done assuming constant sensitivities for each channel, and with values equal to the averaged values of the pre-flight (*Bromage et al.*, 1996) calibration. Only few lines were de-ghosted. In the GIS spectra there are only a few ions whose lines are observed in more than one window and which can be used for calibration purposes: Mg VII; Mg VIII; Mg IX; Fe X; Fe XII; Fe XIII; Fe XV. These lines have been used for checking the relative intensity calibration of the GIS instrument. No evident indications for a modification of the pre-flight intensity calibration (*Bromage et al.*, 1996) were found. More details of the results can be found in *Landi et al.* (1999a).

The revision of the active region spectrum

The study of the active region spectrum has been revised, using: 1) new atomic data (CHIANTI v.2 plus recent Fe XIV calculations, *Storey et al.*, 1999); 2) the *Arnaud and Rothenflug* (1985) ionization equilibrium for all the ions, except the minor elements for which *Landini and Monsignori Fossi* (1991) was used; 3)a constant density $N_{\rm e} = 2\text{x}10^9$ cm^{-3}; 4) coronal abundances (*Feldman et al.*, 1992b).

These data have been used for calibration purposes because many bright high-temperature lines are observed. These lines have been used to constrain part of the GIS 3 and GIS 4 second order calibration, presented below in Figure 3.30. Furthermore, a DEM analysis has been performed on the calibrated data, and synthetic spectra created and compared to the observations, to show how well this calibration reproduces the observed lines.

The DEM is shown in Figure 3.13. Figures 3.14 and 3.15 show the averaged spectra. The main lines, the main ghosts, and those high-temperature lines that are otherwise not visible in the quiet sun and coronal hole spectra (that are presented elsewhere in this thesis), are labelled.

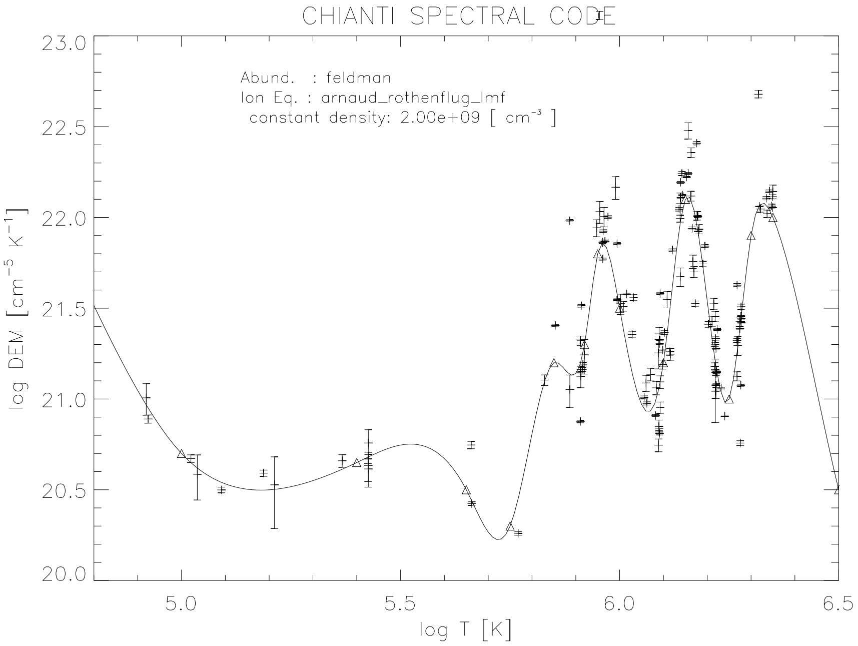

Figure 3.13: *The derived DEM for the active region spectrum of September 2nd 1996. Note the high-temperature peak.*

Table 3.5 presents the results for a selected group of lines, mainly high-temperature lines, and those used for the calibration, with in addition some particular ones. Some of the lines have been reconstructed, i.e. the ghost intensity added to them, while others still have partial, unremovable ghosting. Note:

- The observed lines are well represented, including most of the Fe XIV ones (without the new Fe XIV calculations of *Storey et al.*, 1999, discrepancies of factors of 2 or more are found).
- The second order lines are also well represented. Some of the second order lines are seen also in first order, allowing a direct check of the second order sensitivity.
- The Li-like lines of Na IX and Ne VIII are about a factor of 2 weaker than predicted by theory, while the S XIV lines (445.7 Å) are about a factor of 7 weaker, another example of the problems with the Li-like ions.
- The Fe XV 417.26 Å line is much brighter than expected, especially taking into account the fact that this line, at the moderate GIS resolution, is blended with a S XIV 417.66 Å line that is probably overestimated by a factor of 7. The problem with the Fe XV 417.26 Å again is a well known one (see e.g. *Young et al.*, 1998).

Figures 3.14 and 3.15 also contain synthetic spectra that have been produced (with software written by the author) taking into account the derived DEM, the abundances, and the first and second order calibration (Figure 3.30). The synthetic profiles have been produced by convolution with assumed gaussian profiles of constant width across each channel, and therefore are not exactly comparable with the observed profiles, because of the peculiar GIS line profile characteristics. However, these comparisons give a direct and visible idea of the quality of the adopted assumptions and the completeness of the CHIANTI atomic database. Such comparisons are very rarely found in the literature, where instead results are presented only for a selected group of lines.

Visual inspection of Figures 3.14 and 3.15 shows many interesting aspects: the edge effects; the continuum emission in GIS 3 and GIS 4 (which is not reproduced in the synthetic spectra); the ghosts of the brightest lines; the complexity of GIS 3 and GIS 4 spectra, where ghosts, ghosting lines, first order and second order lines all contribute significantly.

Table 3.5: *Line List for the active region spectrum of September 2nd 1996.*

Ion	λ_{th} (Å)	λ_{ob} (Å)	Transition	I_{ob}	I_{th}/I_{ob}	+/-	Det	log T_{eff}	log T_{max}	frac	
Fe XII	192.393	192.4	3s2.3p3 $^4S_{3/2}$ - 3s2.3p2(3p).3d $^4P_{1/2}$	1359.9	0.84	0.08	G 1	6.18	6.16		
Fe XII	193.521	193.5	3s2.3p3 $^4S_{3/2}$ - 3s2.3p2(3p).3d $^4P_{3/2}$	3752.5	0.86	0.09	G 1	6.18	6.16		
Fe XII	195.118	195.1	3s2.3p3 $^4S_{3/2}$ - 3s2.3p2(3p).3d $^4P_{5/2}$	5495.5	0.98	0.10	G 1	6.18	6.16		
Fe XII	196.648	196.6	3s2.3p3 $^2D_{5/2}$ - 3s2.3p2(1d).3d $^2D_{5/2}$	1093.8	0.63	0.06	G 1	6.19	6.16	0.59	[1]
Fe XIII	196.54		3s2 3p2 $^1D_2$ - 3s2 3p 3d $^1F_3$						6.21	0.40	
Fe XIII	200.022	200.1	3s2 3p2 $^3P_1$ - 3s2 3p 3d $^3D_2$	870.4	0.73	0.07	G 1	6.22	6.21		
Fe XIII	201.128	201.2	3s2 3p2 $^3P_1$ - 3s2 3p 3d $^3D_1$	1527.8	0.57	0.06	G 1	6.22	6.21		
Fe XIII	202.044	202.1	3s2 3p2 $^3P_0$ - 3s2 3p 3d $^3P_1$	3042.6	1.03	0.10	G 1	6.22	6.21		
Fe XI	202.706	202.7	3s2.3p4 $^1D_2$ - 3s2.3p3(2d*).3d $^1P_1$	350.0	0.94	0.10	G 1	6.14	6.11		
Fe XIII	203.828	203.8	3s2 3p2 $^3P_2$ - 3s2 3p 3d $^3D_3$	4081.2	0.80	0.08	G 1	6.22	6.21	0.75	
Fe XIII	203.797		3s2 3p2 $^3P_2$ - 3s2 3p 3d $^3D_2$						6.21	0.25	
Fe XIII	204.263	204.3	3s2 3p2 $^3P_1$ - 3s2 3p 3d $^1D_2$	337.3	1.11	0.12	G 1	6.22	6.21		
Fe XII	206.371	206.1	3s2.3p3 $^2D_{3/2}$ - 3s2.3p2(1s).3d $^2D_{3/2}$	253.4	0.90	0.10	G 1	6.18	6.16		
Fe XIII	209.919	209.6	3s2 3p2 $^3P_2$ - 3s2 3p 3d $^3P_1$	777.2	1.24	0.13	G 1	6.22	6.21	0.55	
Fe XIII	209.621		3s2 3p2 $^3P_1$ - 3s2 3p 3d $^3P_2$						6.21	0.45	
Fe XIV	211.32	211.3	3s2 3p $^2P_{1/2}$ - 3s2 3d $^2D_{3/2}$	2435.3	1.07	0.11	G 1	6.28	6.25		[2]
Fe XIII	213.771	213.9	3s2 3p2 $^3P_2$ - 3s2 3p 3d $^3P_2$	390.2	1.11	0.12	G 1	6.22	6.21		
Si VIII	216.915	216.9	2s22p3 $^2D_{5/2}$ - 2s2p4 $^2P_{3/2}$	562.3	0.95	0.11	G 1	6.10	5.91	0.41	
Fe XIII	216.834		3s2 3p2 $^1D_2$ - 3s2 3p 3d $^3D_2$						6.21	0.24	
Fe XIII	216.869		3s2 3p2 $^1D_2$ - 3s2 3p 3d $^3D_3$						6.21	0.14	
Fe IX	217.101		3p6 $^1S_0$ - 3p5.3d $^3D_1$						5.94	0.12	
Fe XVI	262.984	263.4	3p $^2P_{3/2}$ - 3d $^2D_{5/2}$	226.4	1.10	0.12	G 2	6.34	6.34		
Fe XIV	264.78	264.9	3s2 3p $^2P_{3/2}$ - 3s 3p2 $^2P_{3/2}$	1261.2	1.11	0.11	G 2	6.28	6.25		
Fe XIV	270.507	270.8	3s2 3p $^2P_{3/2}$ - 3s 3p2 $^2P_{1/2}$	169.9	4.45	0.46	G 2	6.28	6.25		[3]
Fe XIV	274.2	274.5	3s2 3p $^2P_{1/2}$ - 3s 3p2 $^2S_{1/2}$	1498.4	0.97	0.10	G 2	6.28	6.25		
Si VII	275.353	275.7	2p4 $^3P_2$ - 2s.2p5 $^3P_2$	203.2	1.18	0.12	G 2	5.91	5.77	0.87	
Si VII	275.667		2p4 $^3P_1$ - 2s.2p5 $^3P_1$						5.77	0.13	
Si X	277.255	277.2	2p $^2P_{3/2}$ - 2s.2p2 $^2S_{1/2}$	553.0	1.20	0.12	G 2	6.08	6.13	0.51	
Si VIII	277.054		2s22p3 $^2D_{5/2}$ - 2s2p4 $^2D_{5/2}$						5.90	0.30	
Mg VII	277		2s22p2 $^3P_1$ - 2s2p3 $^3S_1$						5.81	0.16	
Fe XV	284.16	284.2	3s2 $^1S_0$ - 3s3p $^1P_1$	7765.0	1.01	0.10	G 2	6.32	6.29		
S XI	285.822	285.8	2s22p2 $^3P_1$ - 2s2p3 $^3D_2$	190.3	0.84	0.09	G 2	6.27	6.24	0.71	
S XI	285.587		2s22p2 $^3P_1$ - 2s2p3 $^3D_1$						6.24	0.28	
Al IX	286.377	286.5	2s2.2p $^2P_{3/2}$ - 2s.2p2 $^2P_{1/2}$	34.2	0.70	0.10	G 2	6.06	6.03		
S XII	288.434	288.1	2s2.2p $^2P_{1/2}$ - 2s.2p2 $^2D_{3/2}$	236.5	0.92	0.09	G 2	6.33	6.32	0.83	
Ni XVI	288.166		3s2 3p $^2P_{1/2}$ - 3s 3p2 $^2D_{3/2}$						6.39	0.17	
Fe XIV	289.148	288.8	3s2 3p $^2P_{3/2}$ - 3s 3p2 $^2S_{1/2}$	126.1	0.87	0.09	G 2	6.28	6.25		
Mg VIII	315.039	314.9	2p $^2P_{3/2}$ - 2s.2p2 $^2P_{3/2}$	822.5	0.99	0.10	G 2	5.96	5.91		[4]
Si VIII	319.826	319.6	2s22p3 $^4S_{3/2}$ - 2s2p4 $^4P_{5/2}$	675.0	1.09	0.11	G 2	5.99	5.91		[5]
Fe XIII	320.809	320.5	3s2 3p2 $^3P_2$ - 3s 3p3 $^3P_2$	410.9	0.94	0.09	G 2	6.23	6.20		
Fe XIII	321.4	321.3	3s2 3p2 $^3P_2$ - 3s 3p3 $^3P_1$	131.9	0.82	0.08	G 2	6.22	6.20		
Fe XV	327.011	326.9	3s3p $^3P_2$ - 3p2 $^1D_2$	73.3	1.06	0.11	G 2	6.32	6.29		
Al X	332.789	333.0	2s2 $^1S_0$ - 2s.2p $^1P_1$	316.1	0.75	0.08	G 2	6.16	6.09		[6]
Fe XIV	334.172	334.4	3s2 3p $^2P_{1/2}$ - 3s 3p2 $^2D_{3/2}$	1031.0	1.01	0.10	G 2	6.27	6.24		[7]
Fe XVI	335.41	335.6	3s $^2S_{1/2}$ - 3p $^2P_{3/2}$	3608.6	0.89	0.09	G 2	6.35	6.34		[8]

[1]+ ghost 211.3 Å
[2]ghosting 196.5 Å
[3]ghosting ?
[4]reconstructed
[5]reconstructed
[6]ghosting 316 Å
[7]ghosting 317 Å
[8]reconstructed

Table 3.5: *(continued)*

Ion	$\lambda_{\rm th}$ (Å)	$\lambda_{\rm ob}$ (Å)	Transition	$I_{\rm ob}$	$I_{\rm th}/I_{\rm ob}$	+/-	Det	log $T_{\rm eff}$	log $T_{\rm max}$	frac
Mg VIII	339.006	339.3	2p $^2P_{3/2}$ - 2s.2p2 $^2S_{1/2}$	194.7	0.96	0.10	G 2	5.97	5.92	
Fe XIII	202.044	403.8	3s2 3p2 $^3P_0$ - 3s2 3p 3d $^3P_1$	3043.9	1.02	0.10	G 3	6.22	6.21	
Fe XIII	203.828	408.0	3s2 3p2 $^3P_2$ - 3s2 3p 3d $^3D_3$	2956.7	1.10	0.11	G 3	6.22	6.21	0.75
Fe XIII	203.797		3s2 3p2 $^3P_2$ - 3s2 3p 3d $^3D_2$						6.21	0.25
Fe XV	417.258	417.1	3s2 $^1S_0$ - 3s3p $^3P_1$	524.2	0.79	0.08	G 3	6.34	6.29	0.58
S XIV	417.66		1s2.2s $^2S_{1/2}$ - 1s2.2p $^2P_{3/2}$						6.44	0.40
Fe XIV	211.32	422.4	3s2 3p $^2P_{1/2}$ - 3s2 3d $^2D_{3/2}$	2521.3	1.04	0.11	G 3	6.28	6.25	
Fe XIII	213.771	427.2	3s2 3p2 $^3P_2$ - 3s2 3p 3d $^3P_2$	314.4	1.37	0.18	G 3	6.22	6.21	
Mg VIII	430.465	430.1	2p $^2P_{1/2}$ - 2s.2p2 $^2D_{3/2}$	227.6	1.22	0.12	G 3	5.96	5.91	
Mg VII	431.313	431.0	2s22p2 $^3P_1$ - 2s2p3 $^3D_2$	123.7	1.10	0.11	G 3	5.91	5.80	0.78
Mg VII	431.188		2s22p2 $^3P_1$ - 2s2p3 $^3D_1$						5.80	0.22
Mg VIII	436.735	436.6	2p $^2P_{3/2}$ - 2s.2p2 $^2D_{5/2}$	521.0	0.99	0.10	G 3	5.96	5.91	
S XIV	445.7	445.8	1s2.2s $^2S_{1/2}$ - 1s2.2p $^2P_{1/2}$	10.8	7.33	1.37	G 3	6.39	6.44	
Ne VII	465.22	464.8	2s2 $^1S_0$ - 2s2p $^1P_1$	405.8	0.63	0.06	G 3	5.85	5.72	
Fe XIV	467.395	467.0	3s2 3p $^2P_{3/2}$ - 3s 3p2 $^4P_{3/2}$	121.6	0.42	0.04	G 3	6.27	6.24	
Ne IV	469.823	469.4	2s2 2p3 $^2D_{5/2}$ - 2s 2p4 $^2D_{5/2}$	22.3	0.90	0.11	G 3	5.37	5.28	0.56
Ne IV	469.875		2s2 2p3 $^2D_{3/2}$ - 2s 2p4 $^2D_{3/2}$						5.28	0.37
Al X	332.789	665.9	2s2 $^1S_0$ - 2s.2p $^1P_1$	542.5	0.43	0.06	G 4	6.16	6.09	
Fe XIV	334.172	668.4	3s2 3p $^2P_{1/2}$ - 3s 3p2 $^2D_{3/2}$	1126.7	0.92	0.11	G 4	6.27	6.24	
Fe XVI	335.41	670.8	3s $^2S_{1/2}$ - 3p $^2P_{3/2}$	3631.4	0.90	0.09	G 4	6.35	6.34	
Na IX	681.721	681.8	1s2.2s $^2S_{1/2}$ - 1s2.2p $^2P_{3/2}$	50.2	1.71	0.19	G 4	6.11	5.92	
Fe XI	341.113	682.4	3s2.3p4 $^3P_2$ - 3s.3p5 $^3P_1$	142.6	0.78	0.14	G 4	6.14	6.10	
N III	684.998	684.8	2s2 2p $^2P_{1/2}$ - 2s 2p2 $^2P_{3/2}$	7.0	0.91	0.20	G 4	4.92	5.01	
N III	685.817	685.8	2s2 2p $^2P_{3/2}$ - 2s 2p2 $^2P_{3/2}$	38.3	1.15	0.13	G 4	4.92	5.01	0.72
N III	685.515		2s2 2p $^2P_{1/2}$ - 2s 2p2 $^2P_{1/2}$						5.01	0.28
Fe X	345.723	691.4	3s2.3p5 $^2P_{3/2}$ - 3s.3p6 $^2S_{1/2}$	275.0	0.87	0.11	G 4	6.08	6.04	
Na IX	694.147	694.4	1s2.2s $^2S_{1/2}$ - 1s2.2p $^2P_{1/2}$	22.9	1.86	0.23	G 4	6.12	5.92	
O III	702.897	702.8	2s22p2 $^3P_1$ - 2s2p3 $^3P_2$	51.3	0.95	0.11	G 4	5.02	5.04	0.42
O III	702.821		2s22p2 $^3P_1$ - 2s2p3 $^3P_0$						5.04	0.32
O III	702.891		2s22p2 $^3P_1$ - 2s2p3 $^3P_1$						5.04	0.26
O III	703.854	703.8	2s22p2 $^3P_2$ - 2s2p3 $^3P_2$	76.9	1.10	0.12	G 4	5.09	5.04	0.74
O III	703.848		2s22p2 $^3P_2$ - 2s2p3 $^3P_1$						5.04	0.24
Mg IX	706.058	705.7	2s2 $^1S_0$ - 2s.2p $^3P_1$	81.7	0.61	0.06	G 4	6.03	5.98	
Fe XVI	360.761	721.3	3s $^2S_{1/2}$ - 3p $^2P_{1/2}$	1989.7	0.78	0.08	G 4	6.35	6.34	
Fe XII	364.467	728.7	3s2.3p3 $^4S_{3/2}$ - 3s.3p4 $^4P_{5/2}$	685.7	0.88	0.10	G 4	6.18	6.16	
Mg VII	367.674	735.4	2s22p2 $^3P_2$ - 2s2p3 $^3P_2$	191.4	1.19	0.20	G 4	5.91	5.81	0.77
Mg VII	367.683		2s22p2 $^3P_2$ - 2s2p3 $^3P_1$						5.81	0.23
Mg IX	368.07	736.0	2s2 $^1S_0$ - 2s.2p $^1P_1$	2485.5	0.90	0.09	G 4	6.06	5.98	0.89 [9]
Fe XIII	368.171		3s2 3p2 $^3P_2$ - 3s 3p3 $^3D_3$						6.20	0.11
Fe XI	369.153	738.2	3s2.3p4 $^3P_1$ - 3s.3p5 $^3P_2$	416.3	0.30	0.04	G 4	6.14	6.10	[10]
N II	746.984	746.7	2s2 2p2 $^1D_2$ - 2s2 2p 3s $^1P_1$	5.8	0.94	0.41	G 4	5.21	4.77	
O V	758.675	758.6	2s.2p $^3P_1$ - 2p2 $^3P_2$	15.8	1.11	0.23	G 4	5.43	5.39	
O V	759.439	759.4	2s.2p $^3P_0$ - 2p2 $^3P_1$	15.9	0.84	0.17	G 4	5.43	5.39	
O V	760.444	760.5	2s.2p $^3P_2$ - 2p2 $^3P_2$	61.0	1.02	0.12	G 4	5.43	5.39	0.84
O V	760.225		2s.2p $^3P_1$ - 2p2 $^3P_1$						5.39	0.16
O V	762.002	762.0	2s.2p $^3P_2$ - 2p2 $^3P_1$	14.1	1.16	0.27	G 4	5.43	5.39	
N IV	765.147	765.3	2s2 $^1S_0$ - 2s 2p $^1P_1$	99.7	0.81	0.09	G 4	5.19	5.18	[11]
Ne VIII	770.409	770.7	1s2 2s $^2S_{1/2}$ - 1s2 2p $^2P_{3/2}$	339.5	1.83	0.19	G 4	6.09	5.79	[12]
Mg VIII	772.26	772.0	2p $^2P_{3/2}$ - 2s.2p2 $^4P_{5/2}$	38.3	0.68	0.10	G 4	5.95	5.90	[13]
Ne VIII	780.324	780.3	1s2 2s $^2S_{1/2}$ - 1s2 2p $^2P_{1/2}$	186.9	1.66	0.17	G 4	6.09	5.79	
Mg VIII	782.338	782.2	2p $^2P_{3/2}$ - 2s.2p2 $^4P_{3/2}$	23.8	0.64	0.11	G 4	5.95	5.90	

[9] reconstructed

[10] + ghost 765.3 Å

[11] ghosting 369.1 Å

[12] reconstructed

[13] reconstructed

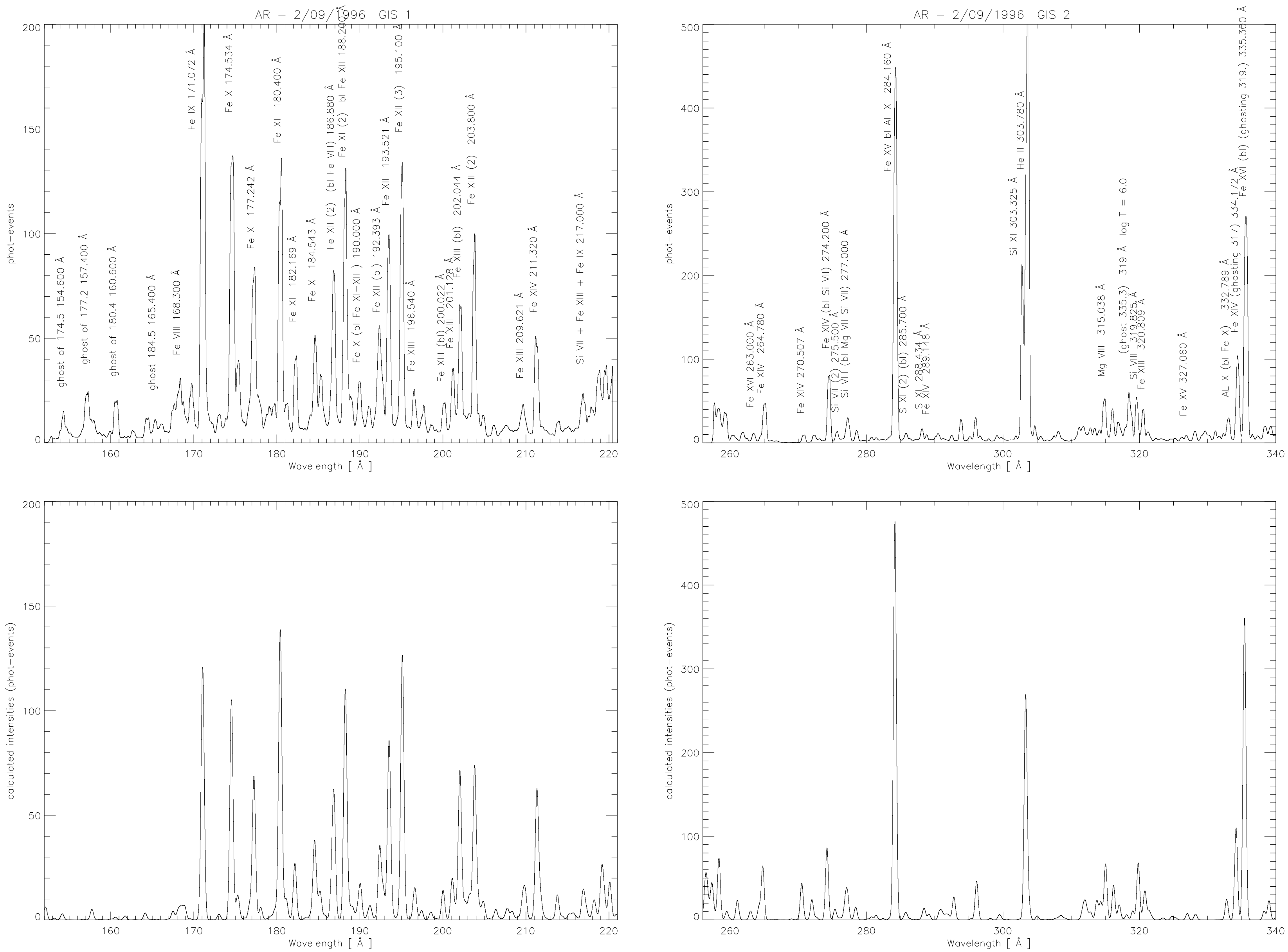

Figure 3.14: *Top: the GIS 1 and GIS 2 spectra of the active region - September 2nd 1996. Bottom: the corresponding synthetic spectra.*

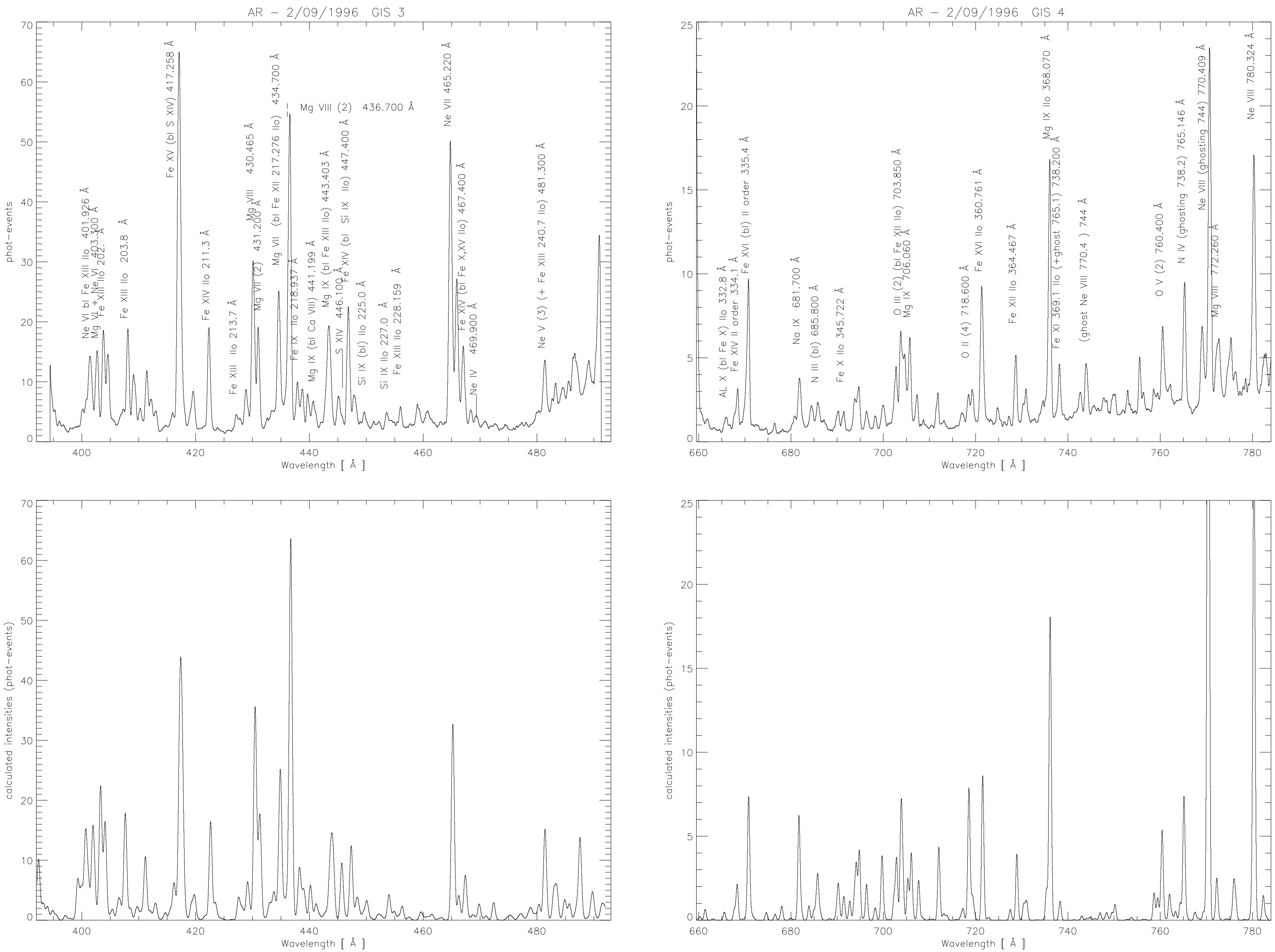

Figure 3.15: *Top: the GIS 3 and GIS 4 spectra of the active region - September 2nd 1996. Bottom: the corresponding synthetic spectra.*

3.4.5 The NIS observations for the internal intensity calibration

The following observations were selected for the internal NIS calibration:

1. An on-disc active region spectral atlas (NISAT study) on the 25th September 1997.
2. Two quiet sun spectral atlases (NISAT studies) at sun centre, on June 22nd 1997 and 19th October 1997.

These types of spectral atlases are routinely performed (see Table C.1 for details). These observations, made in June, September and October were selected, since most of the other NIS-GIS observations that are used for the NIS-GIS cross-calibration were done during those periods. Other observations have been analysed, in collaboration with S. Parenti, and the results confirm those presented in this Chapter. Below, only the the active region observation of 25th September 1997 is presented. The two other NISAT observations are 'normal' observations of the quiet sun.

The on-disc active region observation of 25th September 1997

Monochromatic images of the active region rastered by NIS on the 25th September 1997 were created. Three regions having slightly different characteristics have been selected for creating averaged spectra and subsequent analysis. In all the selected regions the high-temperature lines are the strongest lines in the spectra. In particular, the Fe XVI doublet seen in these NIS 1 (at 335.4 and 360. Å) spectra is particularly important for calibration purposes. In fact, these lines are not density-dependent and the agreement between observations and theory has already been tested in many different (solar and stellar) works. As already mentioned in Chapter 2, in normal quiet sun conditions the Fe XVI lines are very weak and the 335.4 line is mainly Mg VIII (plus a previously unidentified Fe XII line, see below), and not Fe XVI. In the examined spectra, the Mg VIII lines are very weak, as the Fe XII are, compared to the Fe XVI lines, and the 335.4 line is basically all Fe XVI.

Since the results of the DEM analyses of the various regions are very similar, only one is presented here, chosen because the high-temperature lines are not too strong, and the lower temperature ones still have a good signal. Figures 3.16 and 3.17 show the NIS averaged spectra of the chosen area. Note the strong scattered light background intensity, in particular in the NIS 1 spectrum. A complete DEM analysis on the NIS line intensities measured from the spectra shown in Figures 3.16 and 3.17 has been performed. The contribution functions (CHIANTI v.2 plus recent Fe XIV calculations, *Storey et al.*, 1999) have been

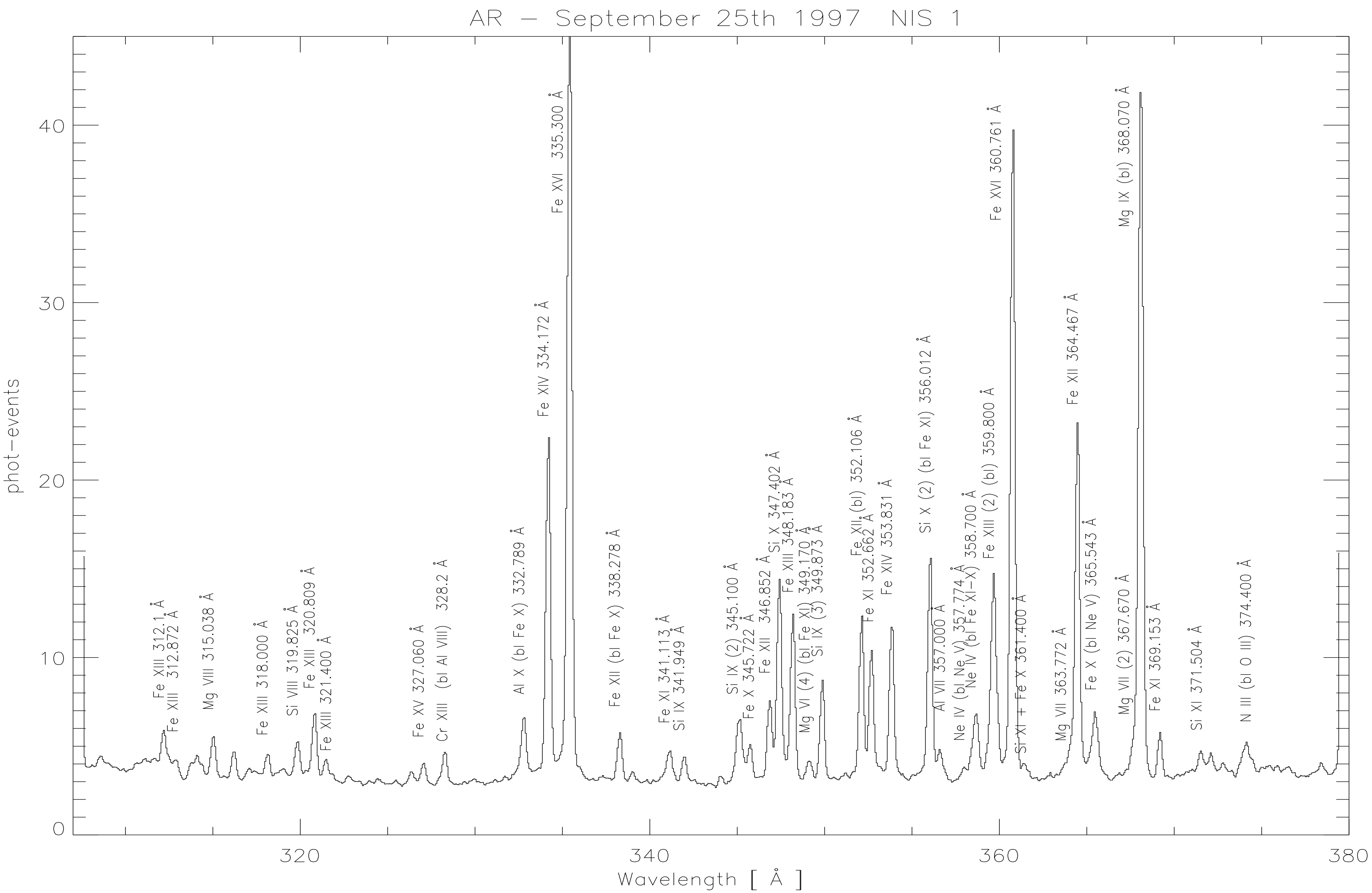

Figure 3.16: *The NIS 1 averaged spectrum of one of the examined areas of the active region observation of September 25 1997.*

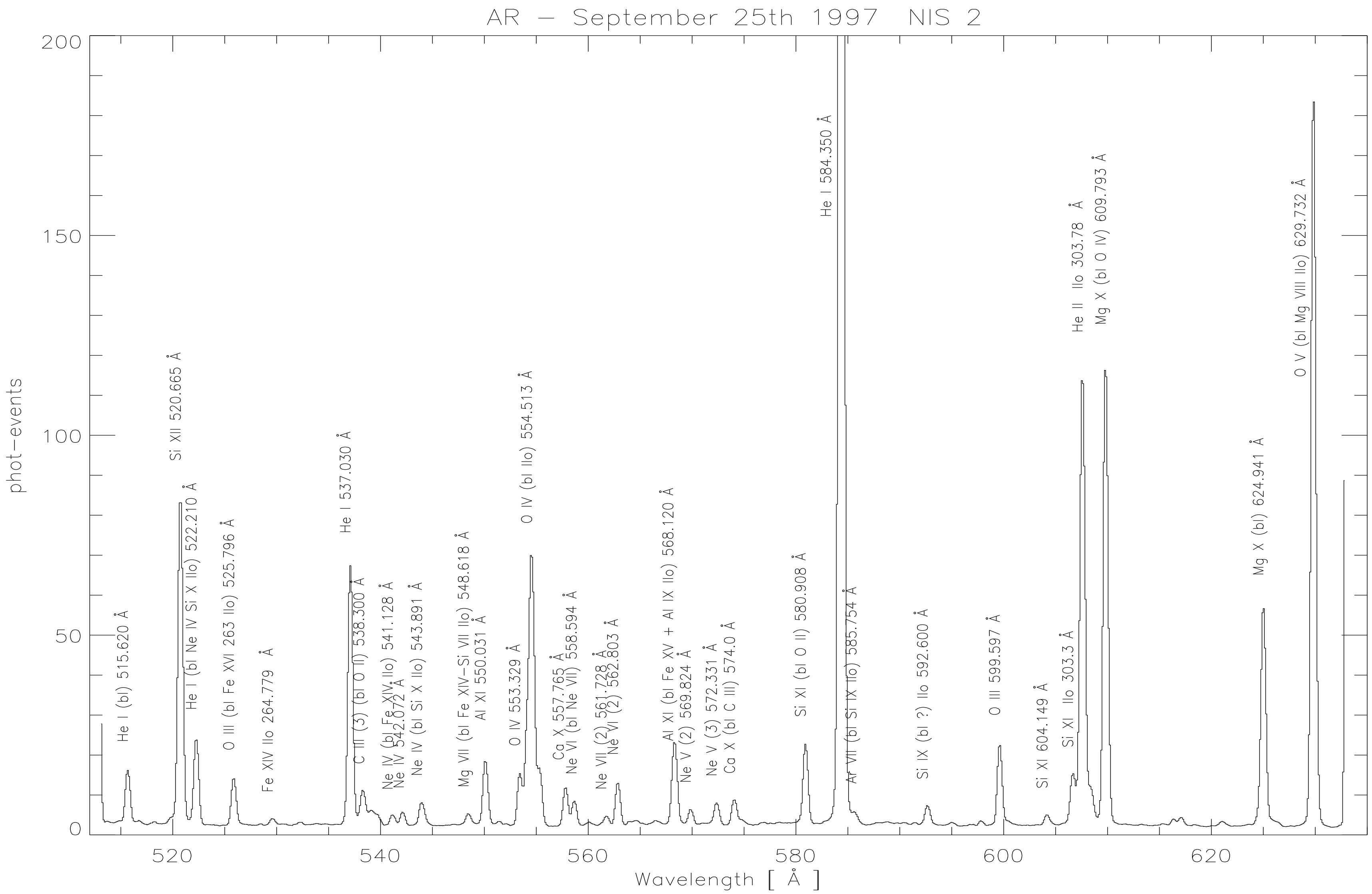

Figure 3.17: *The NIS 2 averaged spectrum of one of the examined areas of the active region observation of September 25 1997.*

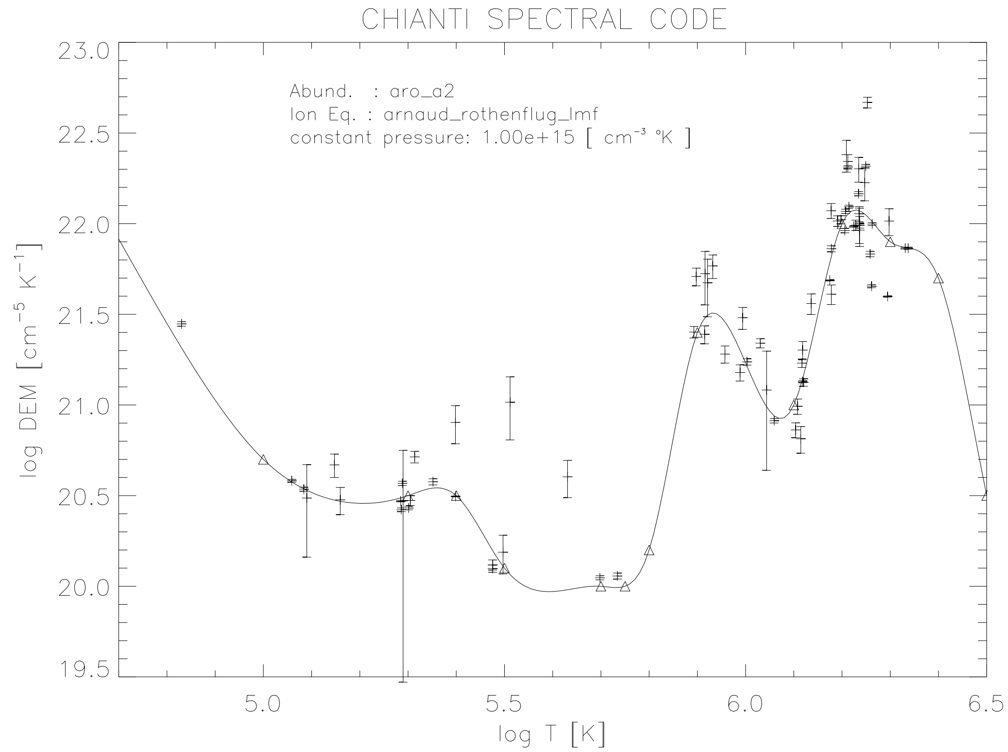

Figure 3.18: *The derived DEM for the on-disc active region observation of 25th September 1997. Note the 'usual' peak at 10^6 K, and the high-temperature peak.*

calculated at constant $N_e = 2 \text{x} 10^9$ cm^{-3}, using the *Arnaud and Rothenflug* (1985) ionization equilibrium (for all the ions) and photospheric abundances (*Grevesse and Anders*, 1991), except for the following elements (with logarithmic differences indicated in parentheses): Ne (+0.2), Al (+0.3), Ca (+0.7).

Figure 3.18 shows the *DEM* for this region, while Table 3.6 presents the results for a small selection of lines. Note:

- the 335.4 Å line intensity is only from Fe XVI. In the other regions within the raster that have been examined, the Fe XVI 335.4/ 360. Å ratio was found to be constant. The Fe XVI 335.4/ 360. Å ratio is therefore used to constrain the sensitivity ratio in NIS at those wavelengths (see Section 3.4.8 below).

- Many bright high-temperature lines, usually not seen in quiet sun or coronal hole NIS spectra, are observed (e.g., Fe XIII, Fe XV, Si XI). Many of these high-temperature lines are also contributing in second order to the NIS 2 spectrum. However, except the lines indicated in Figure 3.17, they are all blended with the strong transition region lines that are visible in NIS 2. For a better examination of them, off-limb spectra are needed.

- The higher-than-photospheric Ne and Al abundances. The Al abundance is the same as that one derived for the SERTS-89 spectrum. The high Ca abundance is based only on Ca X, and is dubious.
- The discrepancy for the Mg V ions, the same as seen in the SERTS-89 spectrum.
- The overestimation (by a factor of 2) of the Li-like Al XI and Si XII.

Table 3.6: *Some of the lines of the active region spectrum of September 25th 1997.*

Ion	λ_{th} (Å)	λ_{ob} (Å)	Transition	I_{ob}	I_{th}/I_{ob}	+/-	Det	log T_{eff}	log T_{max}	frac
O II	538.32	538.3	2s22p3 $^2D_{3/2}$ - 2s2p4 $^2P_{3/2}$	30.0	0.74	0.08	N 2	4.83	4.87	0.42
C III	538.31		2s2p $^3P_2$ - 2s3s $^3S_1$						4.96	0.29
C III	538.147		2s2p $^3P_1$ - 2s3s $^3S_1$						4.96	0.18
O III	599.597	599.6	2s22p2 $^1D_2$ - 2s2p3 $^1D_2$	70.7	0.99	0.10	N 2	5.06	5.06	
O III	525.796	525.9	2s22p2 $^1D_2$ - 2s2p3 $^1P_1$	30.6	1.01	0.10	N 2	5.08	5.07	
O III	374.435	374.5	2s22p2 $^3P_2$ - 2s22p3s $^3P_1$	3.9	1.10	0.59	N 1	5.09	5.11	0.49
N III	374.434		2s2 2p $^2P_{3/2}$ - 2s2 3d $^2D_{5/2}$						5.08	0.45
O III	374.075	374.1	2s22p2 $^3P_2$ - 2s22p3s $^3P_2$	17.2	0.64	0.11	N 1	5.15	5.11	0.60
O III	374.005		2s22p2 $^3P_0$ - 2s22p3s $^3P_1$						5.11	0.15
N III	374.198		2s2 2p $^2P_{1/2}$ - 2s2 3d $^2D_{3/2}$						5.08	0.12
O III	374.164		2s22p2 $^3P_1$ - 2s22p3s $^3P_1$						5.11	0.12
O III	597.817	597.8	2s22p2 $^1S_0$ - 2s2p3 $^1P_1$	4.4	0.98	0.19	N 2	5.16	5.07	
O IV	554.513	554.6	2s2 2p $^2P_{3/2}$ - 2s 2p2 $^2P_{3/2}$	237.0	1.04	0.10	N 2	5.28	5.27	
O IV	553.329	553.4	2s2 2p $^2P_{1/2}$ - 2s 2p2 $^2P_{3/2}$	42.1	1.16	0.12	N 2	5.29	5.27	
O IV	608.397	608.4	2s2 2p $^2P_{1/2}$ - 2s 2p2 $^2S_{1/2}$	44.0	0.84	0.09	N 2	5.29	5.27	
O III	373.805	373.8	2s22p2 $^3P_1$ - 2s22p3s $^3P_2$	2.3	1.05	0.95	N 1	5.29	5.11	
O IV	555.263	555.3	2s2 2p $^2P_{3/2}$ - 2s 2p2 $^2P_{1/2}$	43.1	1.17	0.12	N 2	5.30	5.27	
Ne IV	542.073	542.1	2s2 2p3 $^4S_{3/2}$ - 2s 2p4 $^4P_{3/2}$	11.1	1.07	0.13	N 2	5.30	5.27	
Ne IV	541.128	541.2	2s2 2p3 $^4S_{3/2}$ - 2s 2p4 $^4P_{1/2}$	9.4	0.63	0.08	N 2	5.31	5.27	
Ne IV	543.892	544.0	2s2 2p3 $^4S_{3/2}$ - 2s 2p4 $^4P_{5/2}$	20.9	0.92	0.10	N 2	5.35	5.27	
Ne IV	357.832	358.0	2s2 2p3 $^2D_{3/2}$ - 2s 2p4 $^2P_{1/2}$	20.4	0.40	0.10	N 1	5.40	5.30	0.65
Ne V	357.954		2s22p2 $^3P_0$ - 2s2p3 $^3S_1$						5.49	0.35
O V	629.73	629.8	2s2 $^1S_0$ - 2s.2p $^1P_1$	581.7	1.02	0.10	N 2	5.40	5.39	
Ne V	569.824	569.9	2s22p2 $^3P_1$ - 2s2p3 $^3D_2$	11.1	1.20	0.14	N 2	5.48	5.47	0.76
Ne V	569.753		2s22p2 $^3P_1$ - 2s2p3 $^3D_1$						5.47	0.24
Ne V	572.331	572.4	2s22p2 $^3P_2$ - 2s2p3 $^3D_3$	16.5	1.26	0.14	N 2	5.48	5.47	0.86
Ne V	572.098		2s22p2 $^3P_2$ - 2s2p3 $^3D_2$						5.47	0.14
Ne V	359.382	359.2	2s22p2 $^3P_2$ - 2s2p3 $^3S_1$	17.2	0.84	0.22	N 1	5.50	5.49	
Mg V	355.329	355.4	2p4 $^3P_1$ - 2s.2p5 $^3P_2$	11.8	0.11	0.04	N 1	5.51	5.46	
Mg V	353.092	353.1	2p4 $^3P_2$ - 2s.2p5 $^3P_2$	18.1	0.24	0.06	N 1	5.63	5.46	
Ne VI	562.803	562.9	2s2 2p $^2P_{3/2}$ - 2s 2p2 $^2D_{5/2}$	33.7	0.90	0.09	N 2	5.70	5.63	
Ne VI	558.594	558.7	2s2 2p $^2P_{1/2}$ - 2s 2p2 $^2D_{3/2}$	21.4	0.86	0.09	N 2	5.73	5.63	0.84
Ne VII	558.609		2s2p $^3P_1$ - 2p2 $^3P_2$						5.72	0.16
Ne VII	561.728	561.7	2s2p $^3P_2$ - 2p2 $^3P_2$	9.8	0.87	0.11	N 2	5.89	5.72	
Ne VII	564.528	564.5	2s2p $^3P_2$ - 2p2 $^3P_1$	5.9	0.47	0.07	N 2	5.90	5.72	
Mg VII	367.674	367.7	2s22p2 $^3P_2$ - 2s2p3 $^3P_2$	33.7	1.23	0.19	N 1	5.92	5.81	0.77
Mg VII	367.683		2s22p2 $^3P_2$ - 2s2p3 $^3P_1$						5.81	0.23
Mg VII	363.772	363.8	2s22p2 $^3P_0$ - 2s2p3 $^3P_1$	13.8	0.57	0.20	N 1	5.92	5.81	
Al VII	356.888	356.9	2s22p3 $^4S_{3/2}$ - 2s2p4 $^4P_{5/2}$	13.7	0.66	0.24	N 1	5.92	5.78	
Ne VII	559.948	560.1	2s2p $^3P_0$ - 2p2 $^3P_1$	4.5	0.55	0.10	N 2	5.93	5.72	
Mg VIII	315.039	315.0	2p $^2P_{3/2}$ - 2s.2p2 $^2P_{3/2}$	96.4	1.51	0.22	N 1	5.96	5.91	
Si VIII	319.826	319.8	2s22p3 $^4S_{3/2}$ - 2s2p4 $^4P_{5/2}$	104.5	1.33	0.19	N 1	5.99	5.91	
Fe XI	349.046	349.1	3s2.3p4 $^3P_1$ - 3s.3p5 $^3P_0$	36.2	0.61	0.10	N 1	5.99	6.11	0.38
Mg VI	349.163		2s2.2p3 $^2D_{5/2}$ - 2s.2p4 $^2D_{5/2}$						5.65	0.30
Mg VI	349.124		2s2.2p3 $^2D_{3/2}$ - 2s.2p4 $^2D_{3/2}$						5.65	0.23
Ca X	574.01	574.1	3s $^2S_{1/2}$ - 3p $^2P_{1/2}$	19.9	0.95	0.10	N 2	6.00	5.82	0.87
C III	574.279		2s2p $^1P_1$ - 2s3d $^1D_2$						4.98	0.10
Fe XI	358.621	358.6	3s2.3p4 $^3P_0$ - 3s.3p5 $^3P_1$	98.2	0.51	0.06	N 1	6.03	6.10	0.43
Ne IV	358.686		2s2 2p3 $^2D_{5/2}$ - 2s 2p4 $^2P_{3/2}$						5.30	0.19
Si XI	358.652		2s.2p $^3P_1$ - 2p2 $^3P_2$						6.20	0.18
Ne V	358.484		2s22p2 $^3P_1$ - 2s2p3 $^3S_1$						5.49	0.17
Al VIII	325.292	325.4	2p2 $^3P_1$ - 2s.2p3 $^3P_2$	13.4	0.81	0.52	N 1	6.04	5.92	0.29
Al VIII	325.276		2p2 $^3P_1$ - 2s.2p3 $^3P_0$						5.92	0.29
Al VIII	325.338		2p2 $^3P_1$ - 2s.2p3 $^3P_1$						5.92	0.24
P XI	325.516		2p $^2P_{3/2}$ - 2s.2p2 $^2D_{5/2}$						6.24	0.14
Ca X	557.765	557.8	3s $^2S_{1/2}$ - 3p $^2P_{3/2}$	31.2	1.06	0.11	N 2	6.06	5.82	
Si XI	365.433	365.5	2s.2p $^3P_2$ - 2p2 $^3P_2$	43.6	1.45	0.20	N 1	6.10	6.20	0.40
Fe X	365.543		3s2.3p5 $^2P_{1/2}$ - 3s.3p6 $^2S_{1/2}$						6.04	0.39
Ne V	365.603		2s22p2 $^1D_2$ - 2s2p3 $^1P_1$						5.49	0.21
Fe X	345.723	345.7	3s2.3p5 $^2P_{3/2}$ - 3s.3p6 $^2S_{1/2}$	50.9	1.15	0.16	N 1	6.11	6.04	
Si XI	365.433	365.3	2s.2p $^3P_2$ - 2p2 $^3P_2$	25.9	1.97	0.38	N 1	6.11	6.20	0.49

Table 3.6: *(continued)*

Ion	λ_{th} (Å)	λ_{ob} (Å)	Transition	I_{ob}	I_{th}/I_{ob}	+/-	Det	log T_{eff}	log T_{max}	frac
Mg VII	365.234		2s22p2 $^3P_1$ - 2s2p3 $^3P_2$						5.81	0.18
Mg VII	365.176		2s22p2 $^3P_1$ - 2s2p3 $^3P_0$						5.81	0.17
Mg VII	365.243		2s22p2 $^3P_1$ - 2s2p3 $^3P_1$						5.81	0.13
Si IX	345.124	345.1	2s22p2 $^3P_1$ - 2s2p3 $^3D_2$	115.7	0.79	0.09	N 1	6.12	6.03	0.79
Si IX	344.951		2s22p2 $^3P_1$ - 2s2p3 $^3D_1$						6.03	0.20
Si IX	341.949	342.0	2s22p2 $^3P_0$ - 2s2p3 $^3D_1$	48.2	0.69	0.11	N 1	6.12	6.03	
Mg IX	368.07	368.1	2s2 $^1S_0$ - 2s.2p $^1P_1$	479.6	1.04	0.10	N 1	6.12	5.98	0.73
Fe XIII	368.171		3s2 3p2 $^3P_2$ - 3s 3p3 $^3D_3$						6.20	0.27
Si IX	349.873	349.9	2s22p2 $^3P_2$ - 2s2p3 $^3D_3$	110.9	1.10	0.12	N 1	6.12	6.03	0.88
Si IX	349.794		2s22p2 $^3P_2$ - 2s2p3 $^3D_2$						6.03	0.11
Cr XIII	328.267	328.3	3s2 $^1S_0$ - 3s.3p $^1P_1$	68.8	0.60	0.10	N 1	6.14	6.19	0.58
Al VIII	328.185		2p2 $^3P_2$ - 2s.2p3 $^3P_2$						5.92	0.28
Mg X	609.793	609.8	1s2.(1s).2s $^2S_{1/2}$ - 1s2.(1s).2p $^2P_{3/2}$	443.1	1.26	0.13	N 2	6.17	6.04	0.88
O IV	609.829		2s2 2p $^2P_{3/2}$ - 2s 2p2 $^2S_{1/2}$						5.27	0.12
Fe XI	341.113	341.1	3s2.3p4 $^3P_2$ - 3s.3p5 $^3P_1$	61.9	0.55	0.08	N 1	6.18	6.10	
Fe XI	352.662	352.7	3s2.3p4 $^3P_2$ - 3s.3p5 $^3P_2$	142.0	0.90	0.10	N 1	6.18	6.11	
Al X	332.789	332.8	2s2 $^1S_0$ - 2s.2p $^1P_1$	131.9	0.83	0.10	N 1	6.19	6.09	
Fe XII	346.852	346.9	3s2.3p3 $^4S_{3/2}$ - 3s.3p4 $^4P_{1/2}$	104.5	0.92	0.10	N 1	6.20	6.16	
Si X	356.012	356.0	2p $^2P_{3/2}$ - 2s.2p2 $^2D_{5/2}$	211.7	1.17	0.12	N 1	6.21	6.13	0.88
Si X	356.05		2p $^2P_{3/2}$ - 2s.2p2 $^2D_{3/2}$						6.13	0.12
Si X	347.403	347.4	2p $^2P_{1/2}$ - 2s.2p2 $^2D_{3/2}$	223.7	0.93	0.10	N 1	6.21	6.13	
Si XI	361.412	361.4	2s.2p $^3P_0$ - 2p2 $^3P_1$	24.0	0.46	0.10	N 1	6.21	6.20	0.74
Fe X	361.406		3s2.3p4(3p).3d $^4F_{7/2}$ - 3s.3p5(3p*).3d $^4F_{7/2}$						6.04	0.21
Si XI	580.907	580.9	2s2 $^1S_0$ - 2s.2p $^3P_1$	60.2	0.55	0.06	N 2	6.21	6.19	
Fe XII	338.278	338.3	3s2.3p3 $^2D_{5/2}$ - 3s.3p4 $^2D_{5/2}$	76.6	0.51	0.07	N 1	6.21	6.16	
Fe XII	364.467	364.5	3s2.3p3 $^4S_{3/2}$ - 3s.3p4 $^4P_{5/2}$	286.4	0.92	0.09	N 1	6.21	6.16	
Mg X	624.941	625.0	1s2.(1s).2s $^2S_{1/2}$ - 1s2.(1s).2p $^2P_{1/2}$	196.7	1.23	0.12	N 2	6.22	6.04	
Fe XIII	320.809	320.8	3s2 3p2 $^3P_2$ - 3s 3p3 $^3P_2$	160.8	1.21	0.15	N 1	6.23	6.20	
Fe XIII	359.642	359.7	3s2 3p2 $^3P_1$ - 3s 3p3 $^3D_2$	250.1	0.81	0.08	N 1	6.23	6.20	0.73
Fe XIII	359.842		3s2 3p2 $^3P_1$ - 3s 3p3 $^3D_1$						6.20	0.26
Fe XIII	318.128	318.1	3s2 3p2 $^1D_2$ - 3s 3p3 $^1D_2$	68.5	0.59	0.11	N 1	6.23	6.20	
Fe XIII	312.109	312.2	3s2 3p2 $^3P_1$ - 3s 3p3 $^3P_1$	124.1	1.04	0.14	N 1	6.24	6.20	
Fe XIII	312.872	312.8	3s2 3p2 $^3P_1$ - 3s 3p3 $^3P_0$	50.0	1.18	0.29	N 1	6.24	6.20	
Fe XIII	348.183	348.2	3s2 3p2 $^3P_0$ - 3s 3p3 $^3D_1$	165.4	1.21	0.13	N 1	6.24	6.20	
Fe XIII	321.4	321.5	3s2 3p2 $^3P_2$ - 3s 3p3 $^3P_1$	47.4	1.28	0.27	N 1	6.24	6.20	
Si XI	371.503	371.6	2s.2p $^3P_2$ - 2p2 $^3P_1$	13.6	0.67	0.15	N 1	6.25	6.20	
Si XI	303.324	606.7	2s2 $^1S_0$ - 2s.2p $^1P_1$	2807.9	0.54	0.06	N 2	6.25	6.20	
Si XI	604.147	604.2	2s.2p $^1P_1$ - 2p2 $^1D_2$	13.3	0.24	0.03	N 2	6.25	6.20	
Fe XIV	353.831	353.8	3s2 3p $^2P_{3/2}$ - 3s 3p2 $^2D_{5/2}$	168.0	1.55	0.16	N 1	6.26	6.24	
Al XI	550.031	550.1	1s2.(1s).2s $^2S_{1/2}$ - 1s2.(1s).2p $^2P_{3/2}$	54.7	2.29	0.23	N 2	6.26	6.16	
Fe XIV	334.172	334.2	3s2 3p $^2P_{1/2}$ - 3s 3p2 $^2D_{3/2}$	611.8	1.03	0.11	N 1	6.26	6.24	
Si XII	520.665	520.7	1s2.2s $^2S_{1/2}$ - 1s2.2p $^2P_{1/2}$	204.6	2.06	0.21	N 2	6.29	6.26	
Fe XV	327.011	327.0	3s3p $^3P_2$ - 3p2 $^1D_2$	50.7	0.78	0.15	N 1	6.30	6.29	
Fe XVI	335.41	335.4	3s $^2S_{1/2}$ - 3p $^2P_{3/2}$	1347.8	1.01	0.10	N 1	6.33	6.34	
Fe XVI	360.761	360.8	3s $^2S_{1/2}$ - 3p $^2P_{1/2}$	630.6	1.00	0.10	N 1	6.34	6.34	

3.4.6 The observations for the NIS-GIS cross-calibration

The rationale for special observing sequences

We have already pointed out the need for near-simultaneous NIS and GIS full-wavelength observations. With this in mind, the main issues when using the Sun as a CDS calibration source are the following:

- Temporal variability. It is important to be able to estimate where and how much the solar variability considerably changes the line intensities. Knowing where and when such variations take place is better than just trying to keep the exposure times down as much as possible, because then the signal would be too poor. To do this, first, it is better to observe diffuse quiet regions rather than, for example, active regions, because the variations would be less anyway. Second, a series of repeats of NIS and GIS rasters reveal where intensity variations have taken place (if any). This can then be used to decide which data can be used/integrated.

- Raster sizes. The raster sizes should be small enough to keep the total duration of the observation as short as possible. A bigger area should be scanned by NIS, and a smaller one by GIS which takes longer.

- The solar rotation. As already mentioned, the solar rotation is such that accurate overlaying of different observations is difficult, if they are made near disc centre. Also, the fact that the accuracy of the pointing is less than the spatial resolution, complicates the situation.

- Good signal. To get sufficient signal-to-noise while keeping the time between the NIS and GIS exposures as short as possible, either spatial areas have to be averaged or the exposure time has to be sufficient without this. Also, the wider ($4''$) slits are to be preferred because of the higher signal they produce, considering that this advantage is not gained at any expense of spectral resolution.

- The location and the spatial variability. In on-disc observations, it is important to be able to cross-correlate the GIS and NIS data to get co-alignment (and correct for the solar rotation), and to compare intensities of the lines that are emitted by the same spatial regions, avoiding irregularly varying areas. To do this, there is a need to have a sufficiently large spatial region covered, and some sort of structure to get a good correlation (e.g. the solar limb, a bright point, a network boundary).

  Looking at the limb (or just off, at the limb brightening) instead gives a structure to check that the pointing for the NIS and GIS rasters is the same. The effects of the solar rotation are reduced by the large line-of-sight path, which also produces signals that are several times higher than those of the on-disc observations, which increases the signal-to-noise and allows smaller exposure times to be used. The scattered light and the continuum also disappear from the spectra in off-limb observations, leaving much cleaner spectra to analyse.

Observation sequences and data analysis

The CDS studies that were used for calibration purposes are listed in Table 4.1, and the observations performed and analysed are shown in Table C.1. Some preliminary observations on the disc were made in collaboration with M. Landini and E. Landi of the Arcetri Observatory, Italy. These used the ARC_CALN/v3 and ARC_CALG/v1 studies, repeated successively on the same region near disc centre. The drawback of these observations was that the area rastered by the GIS was larger than that observed by NIS, and count-rates were low. The observations performed on March 3rd 1997 were analysed, but were not fully usable for calibration purposes because many brightenings occurred in network regions, in all the successive observations and because of the solar rotation. Other on-disc observations were performed with the UCLAN_N1/v1 and ARC_CALG/v1 studies, in which only the NIS 1 channel and a few lines observed in NIS 2 were extracted. This was done to focus on the overlapping region between the NIS 1 and the GIS 2 channels.

The NIS observations that were developed for the observations at the limb are small rasters of full spectra using the $4''$x $240''$slit. The CDS study name is ARC_CALN/v3, covering an area of $32''$x$70''$. After rotating the spectra, this reduces to $32''$in X and about $40''$in Y. With an exposure time of 45s, it takes less than 13m to raster the whole area. The GIS observation used the CDS study DEM_GIS/v2, where the $4''$x$4''$slit is rastered in order to cover a $24''$x $24''$region with 36 spatial positions. The total duration is just under 13m, with a 20s exposure time. The ARC_CALN and DEM_GIS were repeated in succession about five times, without changing the pointing, for a total duration of about 2 hours.

The observations analysed in detail were performed on May 4th (two sets of observations), June 20th, October 1st, October 16th 1997. Most of the observations have been completely successful in terms of pointing, telemetry, good signal, and reduced time variability. Only a very few 'typical' results have been selected as examples from this very large dataset, for presentation here.

The standard corrections (e.g. cosmic ray removal and de-tilt for the NIS case) already described were applied to the data. Then, special software was written to deal with such a complex case, with a total of 40 (8x5) NIS exposures and 180 (36 x5) GIS spectra, for each set of 5 successive NIS and GIS rasters analysed. In short, this software allowed an evaluation of the temporal variations, and the possibility to select spatial areas and different observations in order to produce GIS and NIS averaged spectra emitted by the same spatial regions at times when intensity variations were at a minimum. Figure 3.19 shows as an example a sequence of GIS rasters over a region on the quiet west limb observed on May 4th 1997. This figure already shows that this region was very quiet. The NIS rasters were performed at the same position, alternating with the GIS ones.

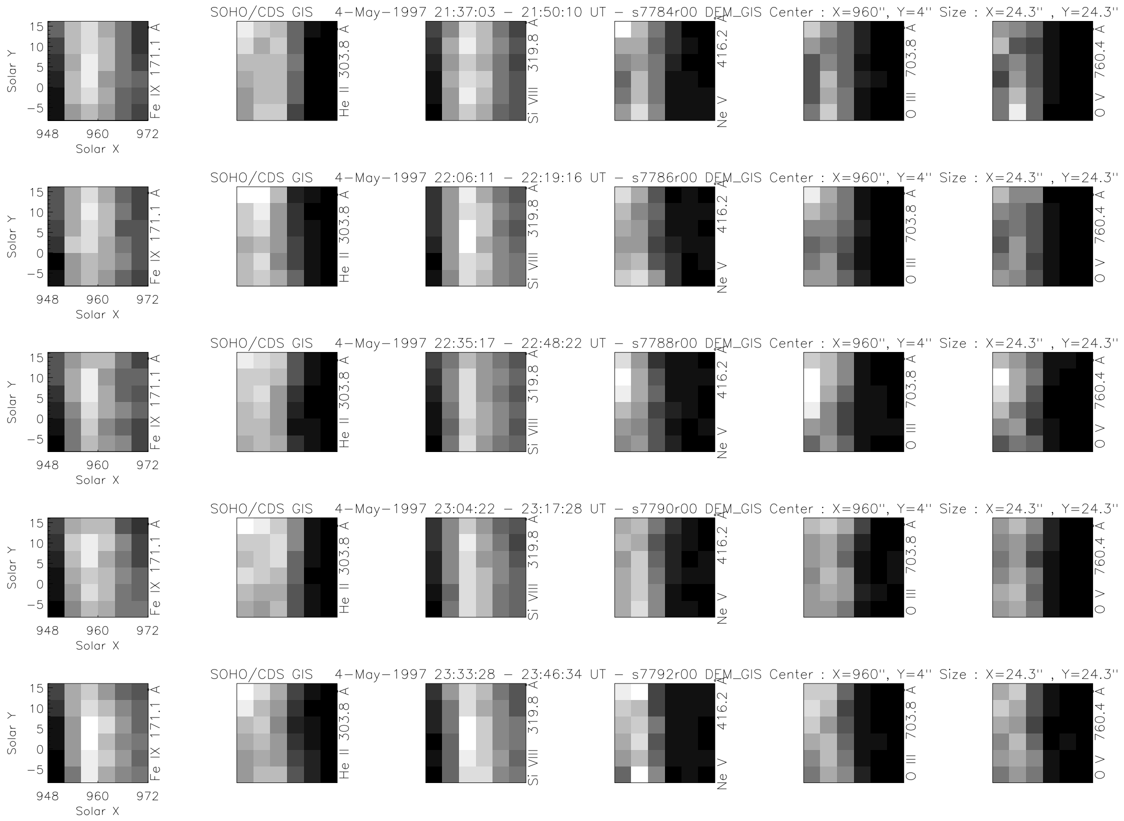

Figure 3.19: *Monochromatic images in few selected lines observed with the DEM_GIS study at the limb, on May 4th 1997. The images for each line are plotted with the same intensity scale, showing only marginal intensity variations in time.*

In order to increase the signal, and reduce the effect of the cosmic rays, averaged GIS and NIS spectra for each mirror position (i.e. for each Solar X) and for each observation (file) have been averaged selecting a spatially overlapping region along Solar Y. These spectra were fitted, and figures such as Figure 3.20 inspected in order to judge if there were observations with brightenings. Indeed some cases were found, and the corresponding files excluded. For example, only three successive NIS and GIS rasters were used for the May 4th observation, while only four NIS and GIS rasters were usable for the October 16th observation.

Once this was established for all the observations, an analysis of the time-averaged spectra

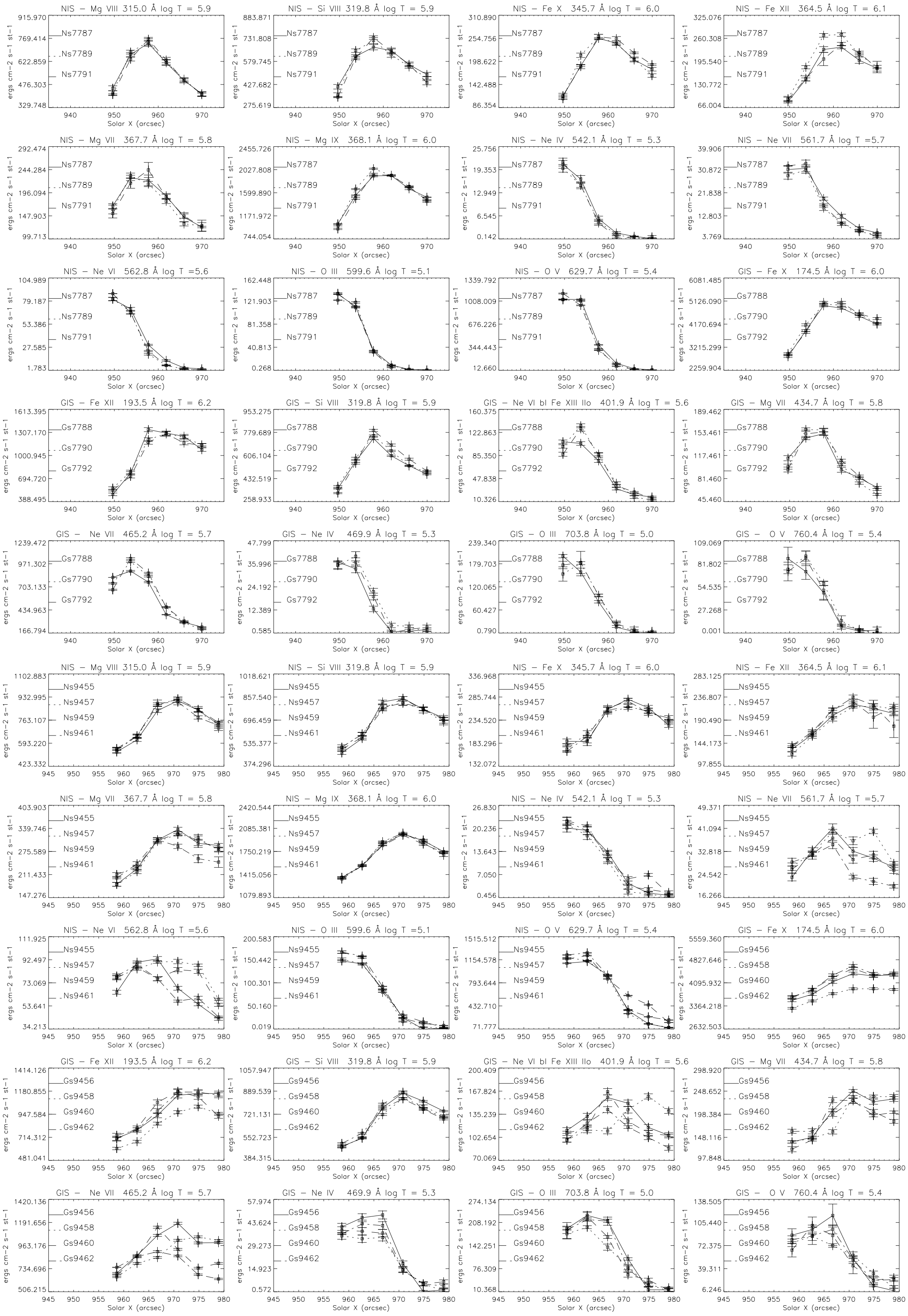

Figure 3.20: *Some intensities of NIS and GIS lines, as a function of position across the limb and time – May 4th (upper five rows) and October 16th (below), 1997. Note the limb brightening in some lines and the rapid disappearance of the 'cool' transition region lines just off-limb.*

was performed, with accurate line fitting and background subtraction, for a few spatial positions, typically one on the disc, and one off the limb. The diagnostic method was then applied to each of these many spectra, typically for each date, one on-disc and one off-limb, and the information from the two data sets combined, to find the relative calibration for each NIS and GIS channel. It was expected that the calibration would not depend on the position, in particular since the overall intensities of all the coronal lines did not change by large factors, see Figure 3.20. The only position-dependent factor is the aperture at the telescope, which was taken into account (although this correction is only about 2% for the NIS, given the small region rastered). First, however, some direct comparisons between the various observed lines were done, and are described below.

The overlapping regions between the CDS channels

The CDS detectors contain some overlapping spectral regions, where the same emission lines are observed in two channels, either in first or second order. Examples are NIS 1 (330-379 Å) with GIS 4 (second order), and NIS 1 with GIS 2 (308-340 Å), shown in Figures 3.21 and 3.22. These figures show the series of spectra superimposed, on the same scale, and demonstrate visually that temporal variations were small. The main variation is due to the scattered light in the NIS 1 channel, that is particularly evident in Figure 3.22. This comparison also shows the evident presence of ghosts in the GIS spectra. Some of the lines such as the Fe XVI blend at 335.4 Åare almost completely ghosting, and 'disappear'. It should be noted that this spectral region and these types of quiet sun observations are not the worst example, of ghosting and scattered light effects.

Direct comparisons of the line intensities give a measure of the relative calibration between the different channels. An example is given in Figure 3.23, which shows the ratio of Mg VIII and Si VIII line intensities as observed in the NIS 1 and GIS 2. These ratios have been calculated leaving out only the sensitivity factor in the intensity calibration (i.e. taking into account the other different factors between the NIS and GIS calibration), and are therefore a direct measure of the relative sensitivity. The NIS channel around 319.8 Å has a sensitivity about a factor 0.12 lower than GIS 2. Also, the same ratios for all the different dates examined have the same averaged value, meaning that **the relative calibration at 320 Å between NIS 1 and GIS 2 has not changed over six months**, which is an important result. The same applies for the other possible combinations of channels. Figure 3.23 also shows the ratio between Mg IX 368 Å, the (usually) brightest line in NIS 1, and in second order in GIS 4. Again, the ratios have not shown appreciable variations in all the spectra examined.

A puzzling aspect that was apparent in all the observations is a tendency for the ratios

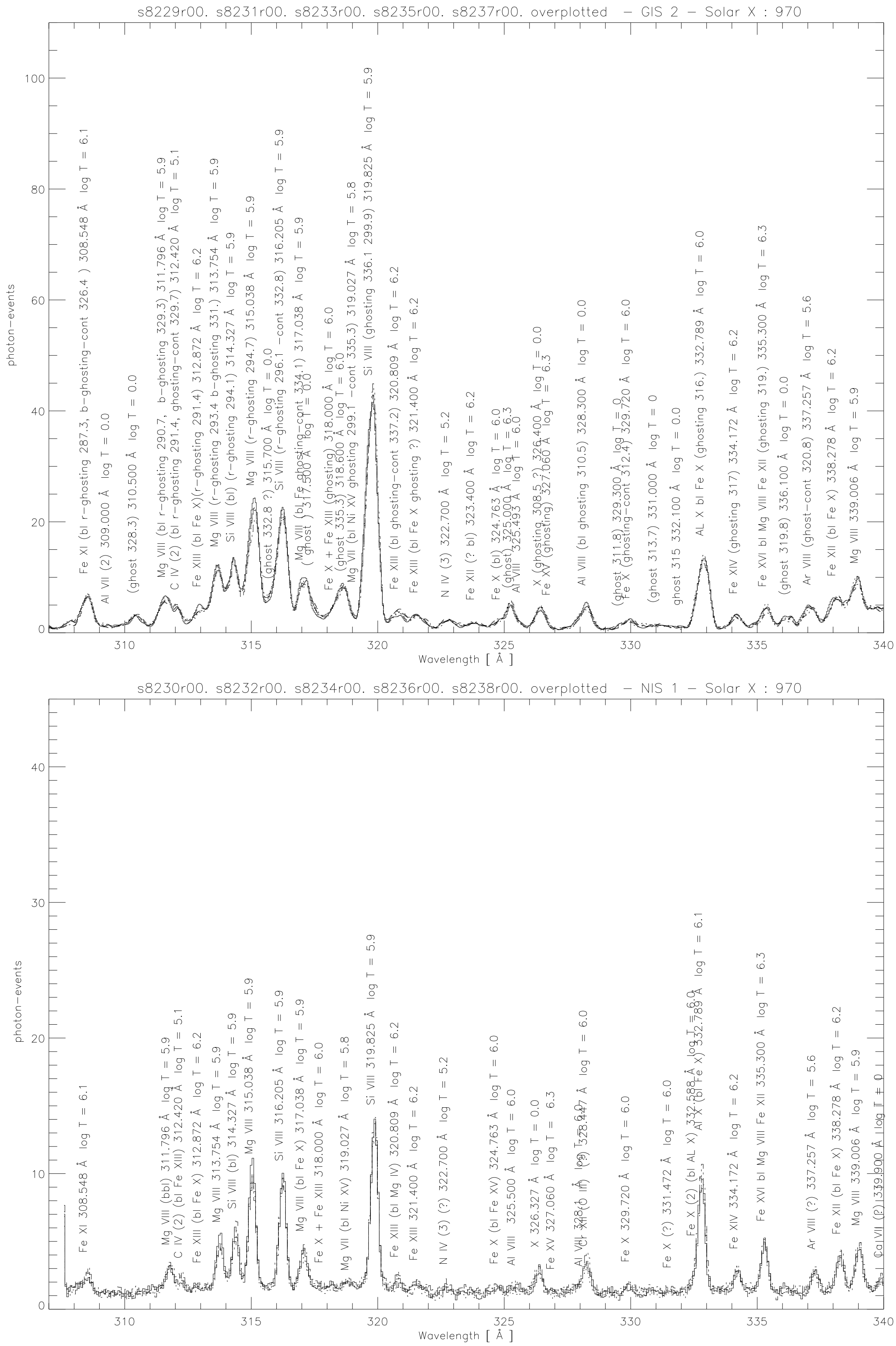

Figure 3.21: *The off-limb GIS and NIS spectra overlaid – 20th June 1997. Only the overlapping region is plotted. Note: (1) the small variation in time; (2) the large differences between the spectra, some of which can be ascribed to ghosting, other to different intensity calibration curves; (3) in particular how some of the GIS lines are depressed due to ghosting; (4) the ghosts that are present in the GIS spectrum.*

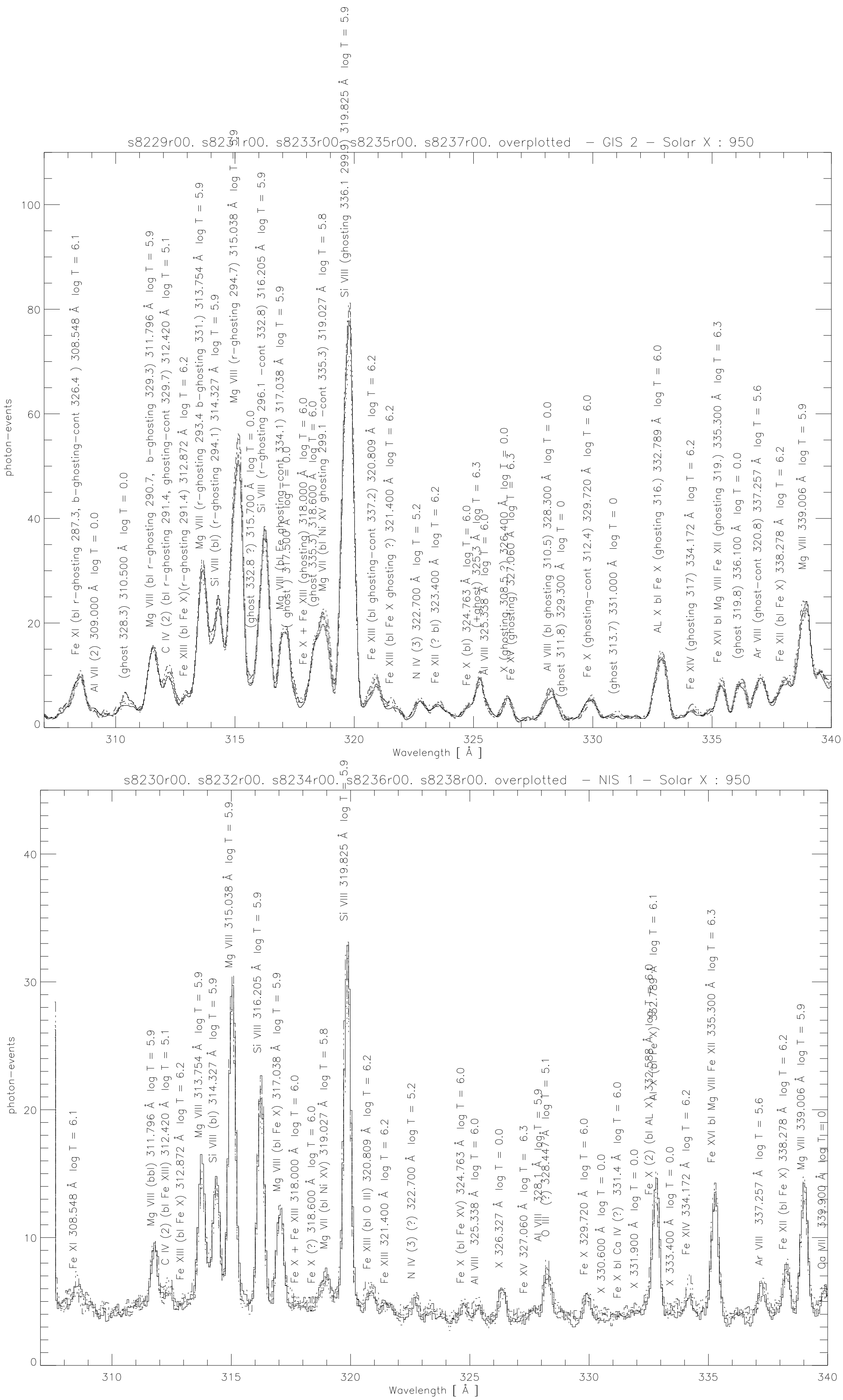

Figure 3.22: *The on-disc GIS and NIS overlapping region, as in Figure 3.21 – 20th June 1997. Note the higher background in the NIS spectrum.*

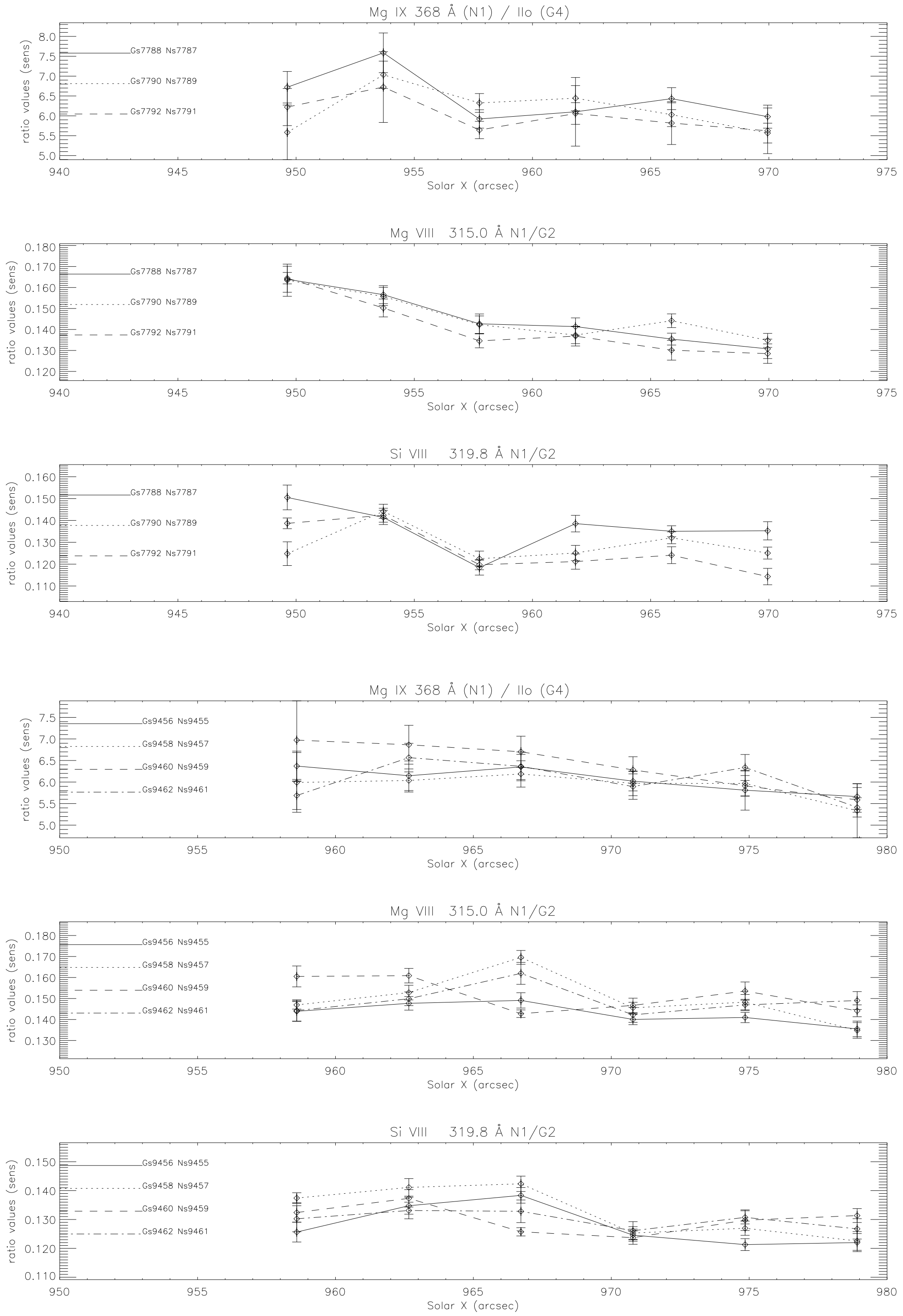

Figure 3.23: *The intensity ratios (calculated leaving out only the sensitivity factor) of the same lines observed in the NIS and GIS spectra – May 4th (upper three plots) and October 16th (below), 1997. Note: (1) how close the ratio values are for the two different dates, which is a direct confirmation of the fact that the relative sensitivities between the NIS 1 and GIS 2 (and NIS 1 and GIS 4, from the Mg IX 368 Å) channels have not significantly changed between May and October 1997; (2) a tendency for the ratios to be different on the disc; (3) that NIS 1 sensitivity at 319.8 Å is about a factor 0.12 lower than the GIS 2 one; (4) that the fact that the sensitivity ratio at 315 Å is higher implies a different wavelength dependence for the NIS 1 and GIS 2 sensitivities in that wavelength region.*

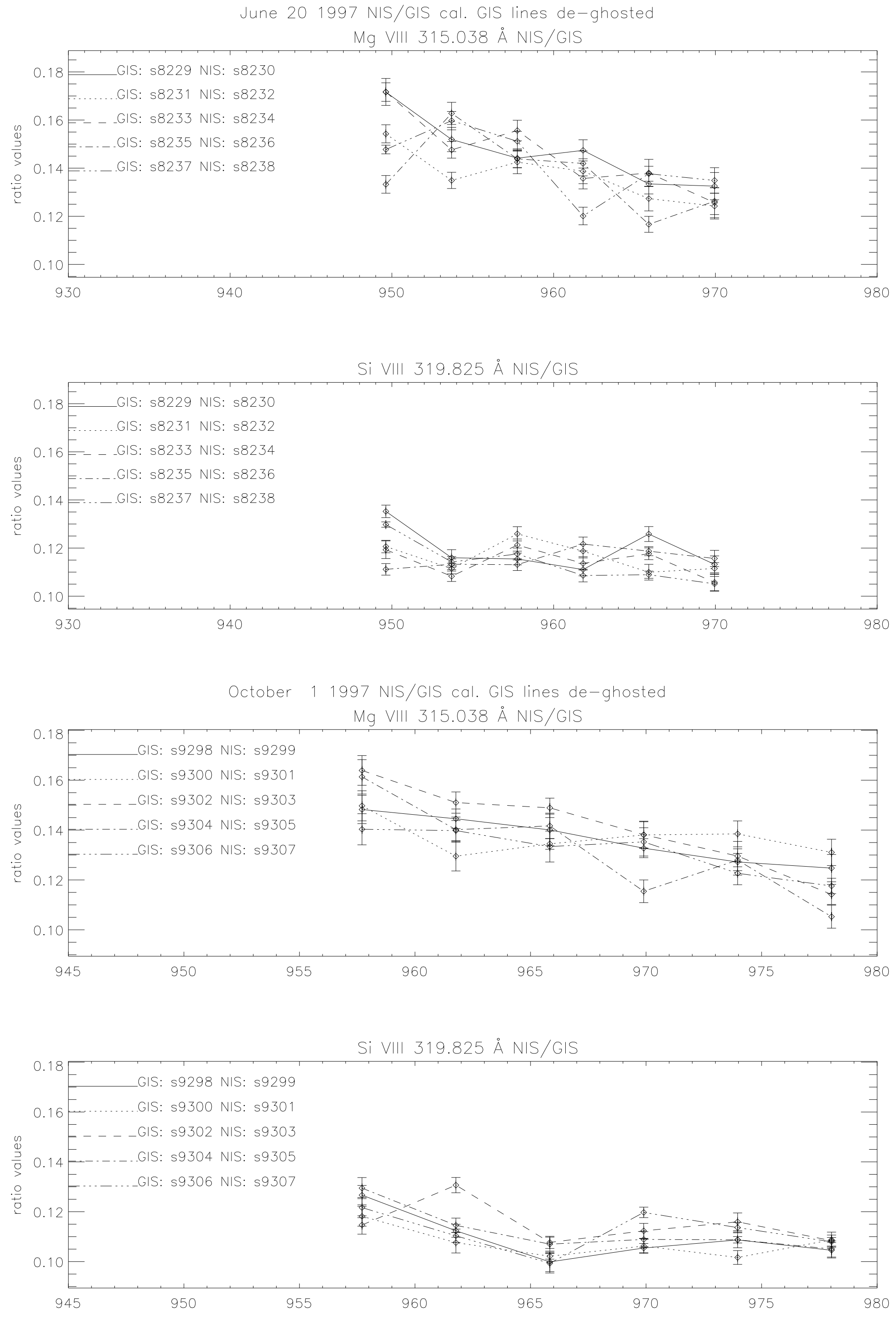

Figure 3.24: *The intensity ratios (calculated leaving out only the sensitivity factor) of the same lines observed in the NIS and GIS spectra – June 20th (upper two plots) and October 1st (below), 1997. Note that the relative sensitivities are the same as in Figure 3.23 (within the errors and the time variations) and that also in this case the sensitivity appears to be different between the on-disc and off-limb case.*

to be different on the disc, as partly shown in Figures 3.23 and 3.24. In general, all the NIS line intensities appear to be consistently shifted by a 10% as a whole, in respect to the other lines seen in the other CDS detectors. Apparently, the NIS 1 sensitivity varies between the on-disc and the off-limb observation by this amount. This effect will need a more complete analysis to be assessed. A brief discussion of it can be found in Section 3.4.8 below.

The lines of the same ion seen in different channels

Another step in the calibration was the analysis of temporal and spatial variations of all the principal lines observed in all the spectra, to find for each ion the best un-blended and not too density-sensitive lines, and for each date the best set of data. Figures 3.25,3.26, and 3.27 show some examples. These lines can be grouped in three classes:

1. Coronal lines. These lines appear in all the CDS spectra with the same characteristics. Some of these are shown by the constancy in space and time of their ratio values (see Figure 3.25).

2. Transition region (cool) lines. These lines are 'crucial' for a relative calibration of the NIS 1 and NIS 2 channels. In fact, as already mentioned, most of the NIS 1 lines are coronal lines, and most of those observed by NIS 2 are transition region ones, and these two channels can only be properly calibrated with the use of the GIS spectra, that observe both transition region and coronal lines in each channel, in particular in GIS 3. Unfortunately, some of these lines are partly density-dependent and, more important, present large intensity variations in time (on time-scales of minutes), and only a careful temporal analysis allows these lines to be used for calibration purposes. Figure 3.26 shows some of these ratios.

3. Blended lines. Among the brightest lines in the CDS spectra are the doublets, which are useful for calibration purposes, but that unfortunately, in most cases are blended with other lines. We have already seen the Fe XVI 335.4 complex case. Other examples are Al XI, Ca X and Mg X, the strongest lines in NIS 2 off-limb spectra which are blended with cool lines, as is evident from Figure 3.27. Therefore, only off-limb observations of these lines can be used for calibration purposes (unless the contribution from the cool line is theoretically removed, as many authors have done in the literature). The Ne VIII doublet of bright lines is not blended, but is shown in Figure 3.27 for comparison. These lines do not show appreciable spatial variation, and therefore show that if departures from the optically thin limit are present, they are very small, because the Ne VIII ratio is close to 2 (see *Doschek et al.*, 1981). On

the other hand, *Doschek et al.* (1998b) have found (from SUMER spectra) this ratio to have values of $\simeq 1.4$ at the limb in coronal holes, with an implication of opacity effects. It is also assumed that no opacity effect is present in the other doublets, and indeed the CDS intensity calibration has been adjusted in order for these ratios to be 2 in the off-limb spectra.

Ghosting and the reconstruction of some lines

Some ghosts have been definitively identified, and the lines reconstructed. Table 3.4.6 presents an example of some of the ghosting reconstruction applied to a GIS observation, i.e. a list of some of the brightest 'pure' ghosts found, in which case it was possible to directly deghost some of the lines. The most impressive example of a ghost is the line at 744 Å, the ghost of the Ne VIII 770.409 Å. Typically, the intensity of these ghosts is more than 40% that one of the observed line. A reconstruction of the line permits to achieve an agreement with the other Ne VIII 780.324 Å line. The counts of each ghost have been transferred to the relative parent line. In some cases, a parent line created both red and blue-shifted ghosts. In many cases, these parent lines are contaminated by ghosts of other lines, and therefore their restored intensity should be taken with caution.

More complete reconstructions have been performed for the time-averaged spectra. More information on ghosting can be found in the Appendix, where some sample quiet sun on-disc and off-limb spectra are presented. Other examples of ghosting will be given throughout this thesis.

The NIS and GIS spectra of the quiet sun observations

Figures C.1, C.2, C.3, C.4, C.5, C.6 show the averaged off-limb CDS spectra of one of the two sets of May 4th 1997 observations. The pointing was sufficiently high above the limbs that all the transition region lines are completely absent. Also the stray light is almost absent, as can be judged by the disappearance of the bright chromospheric lines (e.g. the He I lines). These spectra are therefore very suitable for a study of the quiet sun off-limb spectra. Almost all the hundreds of lines have been identified with the diagnostic method, and are indicated in the figures.

Figures C.11, C.12, C.13, C.14, C.15, C.16 show the averaged on-disc CDS spectra of the October 16th 1997 observations.

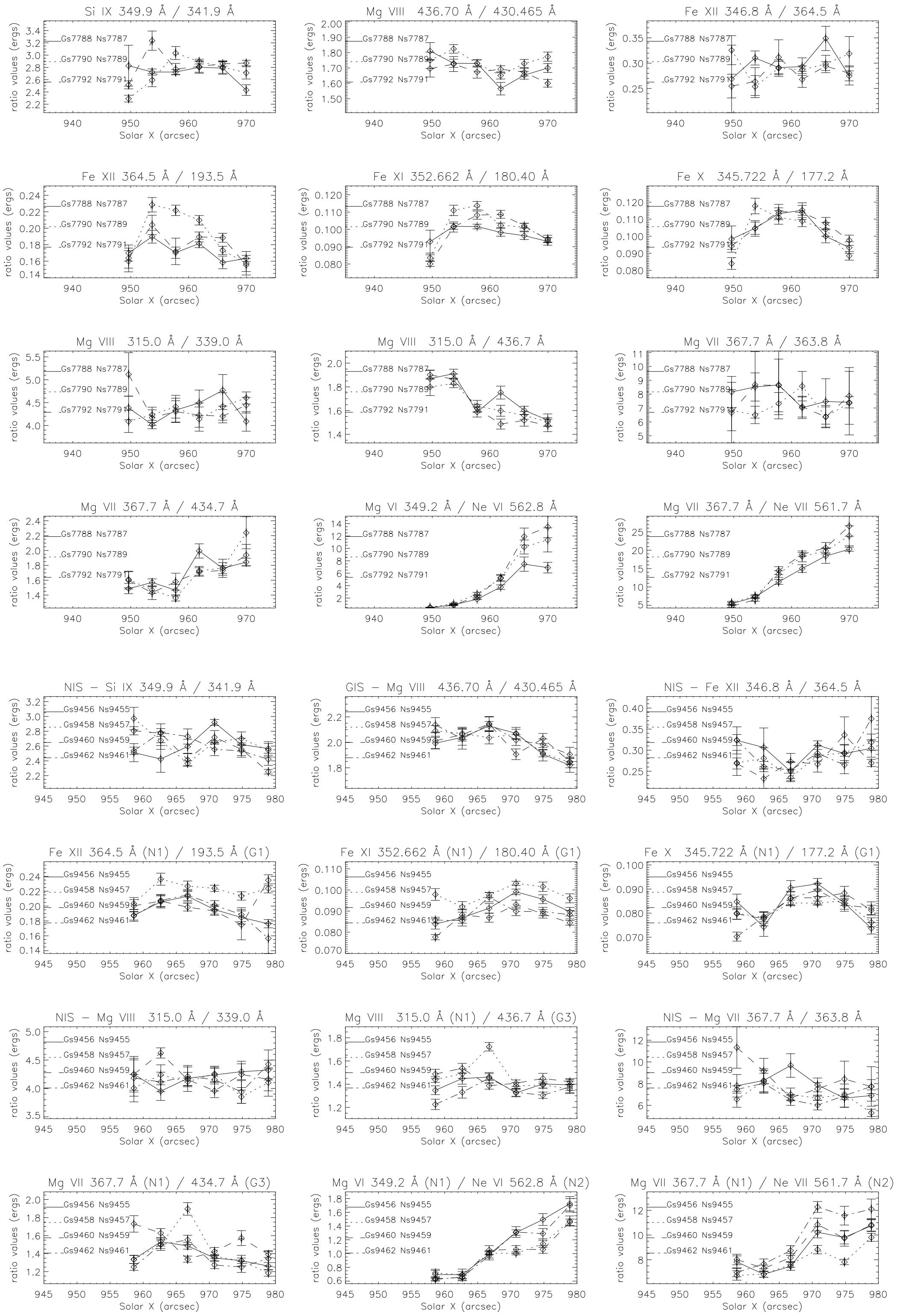

Figure 3.25: *Some intensity ratios of NIS and GIS lines, useful for the NIS/GIS cross-calibration, and for internal calibration within each detector – May 4th (upper four rows) and October 16th (below), 1997. The same intensity calibration has been applied for the two dates. Note: (1) that the density is fairly constant, as shown by the Si IX and Mg VIII ratios (first two figures on the left top corner); (2) that the relative sensitivities between the presented lines, originating from the same ion, and seen either within the same channel or in different ones, is relatively constant in time and in space (middle figures), and are therefore usable for calibration purposes; (3) that lines originating from different ions, as the Mg VI/Ne VI and Mg VII/Ne VII, are not usable for calibration purposes, as their ratio spatially varies by large factors (last two figures, bottom right).*

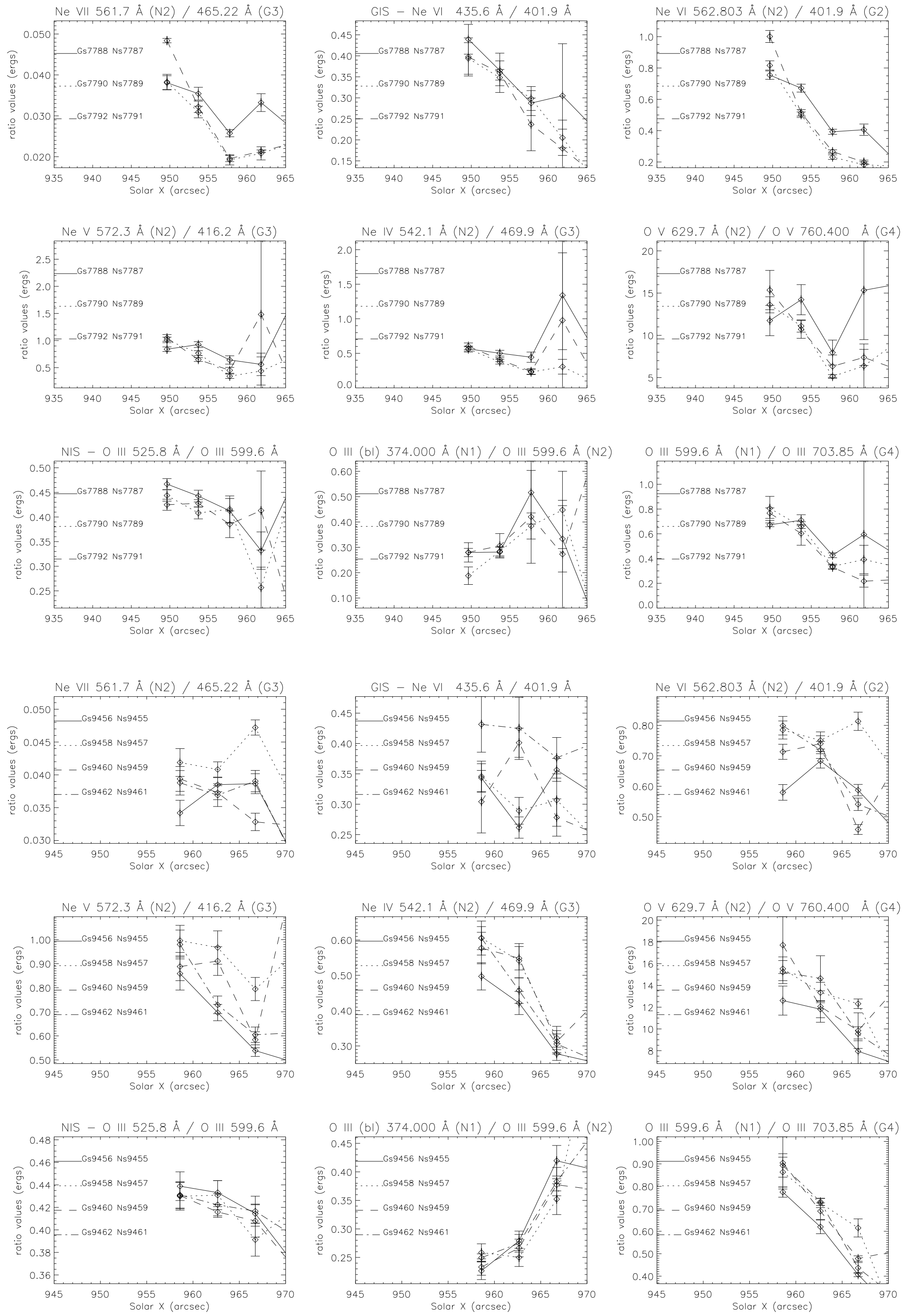

Figure 3.26: *Some ratios of intensities of NIS and GIS transition region lines, useful for the NIS/GIS cross-calibration, and for internal calibration within each detector – May 4th (upper three rows) and October 16th (below), 1997. The same intensity calibration has been applied for the two dates. Note: (1) how temporal variations are small, considering that these cool lines alway present large intensity variations; (2) how close the ratio values are for the two different dates, confirming that the relative sensitivities for the lines shown have been constant in time. These lines (among other not shown here) are therefore suitable for relative calibration purposes, for these observations. Only the values on the disc were used for the calibration (the first point, at Solar X $\simeq$ 950$''$, 960$''$), since these lines disappear above the limb, see Figure 3.20.*

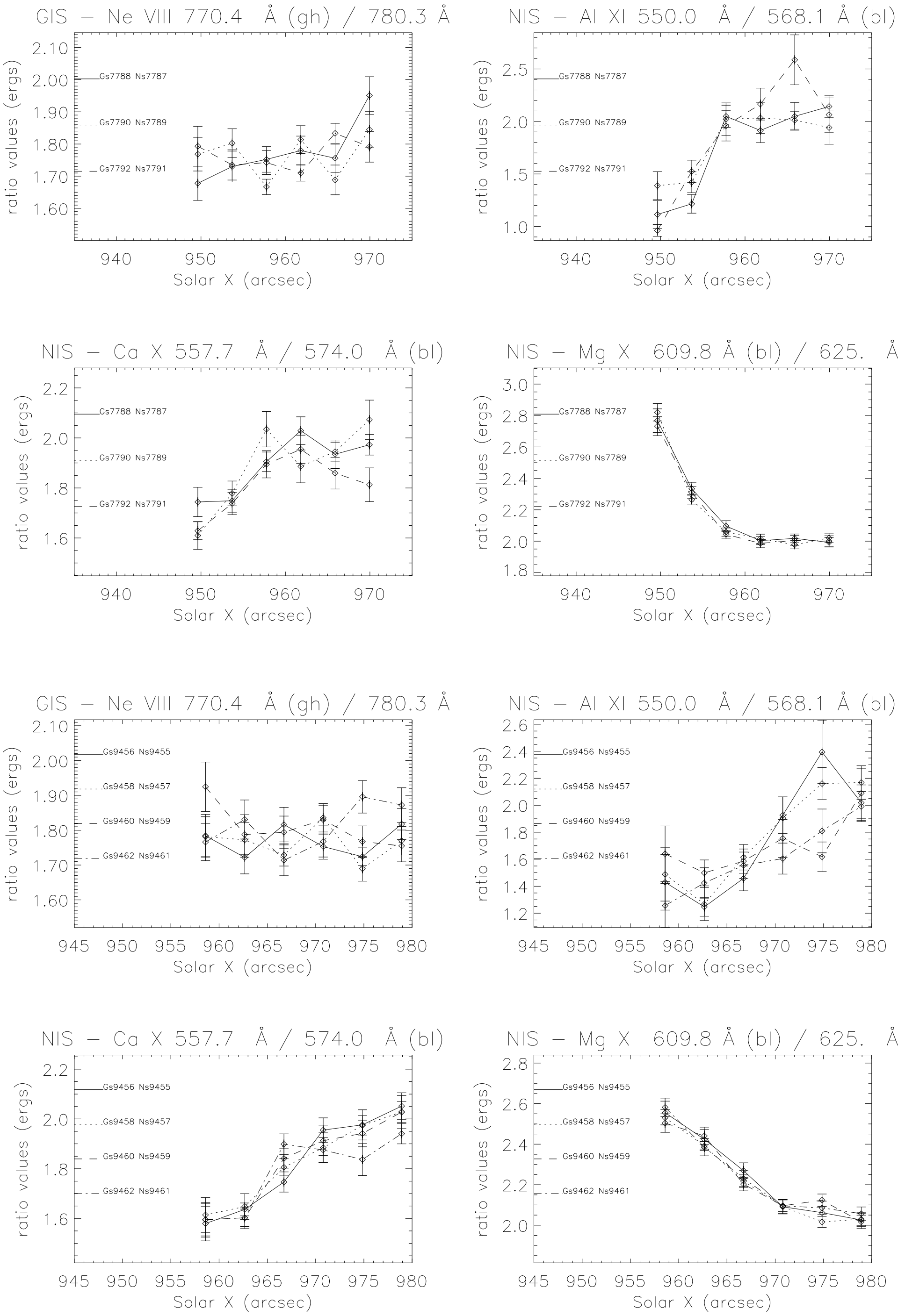

Figure 3.27: *The intensity ratios of the doublets (Li- and Na-like) seen in NIS and GIS – May 4th (upper four figures) and October 16th (below), 1997. The same intensity calibration has been applied for the two dates. The Al XI, Ca X and Mg X are the strongest lines in NIS 2 off-limb spectra and are useful for the internal calibration of NIS 2. Note: (1) the GIS line at 770.4 Å has been reconstructed from ghosting (by 40-70%); (2) that the Ne VIII ratio do not show much variation across the limb, suggesting small (if any) opacity; also, that the ratio value is close to the theoretical value of 2; (3) that in all the other three ratios one of the transition is strongly blended with an on-disc line, and is only off-limb that the blend disappears, and the ratios level toward the theoretical value of 2.*

Table 3.7: *Some of the ghosting reconstruction applied to the GIS observation s7792r00 (a) of May 4th, 1997 and s9462r00 (b) on October 16th, 1997. Each column gives the amount of correction applied for each of the six spatial locations. The corrections applied to the other spectra are similar to the (a) and (b) cases. The averaged positions of the ghost and ghosting lines are indicated. Then, for each spatial position, the ratio of the intensity of the ghost with that one of the ghosting line (in counts) is presented, together with the intensity of the ghosting line (in counts), in brackets. Note that the correction for ghosting is important for many lines. Some lines (Fe XVI 335.4 Å, and Mg VIII 436.7 Å) have been corrected twice, while some (Si VIII 319.8 Å) have been corrected for both the red- and blue-shifted ghosts. Also note that the amount of ghosting varies with the intensity of the ghosting line, for each observation, and that for some reasons ghosting was much higher for the October 16th observations (all the NIS-GIS observations presented in this Section had the same GSET_ID applied).*

ghost (157.24 Å) of Fe X 177.25 Å						
(a)	0.34 (727)	0.40 (1059)	0.43 (1345)	0.41 (1325)	0.40 (1212)	0.34 (1163)
(b)	0.63 (856)	0.70 (887)	0.74 (1039)	0.79 (1029)	0.74 (1026)	0.64 (1056)
ghost (160.63 Å) of Fe XI (bl Fe X) 180.47 Å						
(a)	0.20 (952)	0.22 (1314)	0.24 (1901)	0.24 (1976)	0.24 (1796)	0.21 (1722)
(b)	0.36 (1121)	0.39 (1239)	0.41 (1407)	0.40 (1556)	0.40 (1542)	0.35 (1561)
ghost (294.05 Å) of Si VIII 314.36 Å						
(a)	0.31 (146)	0.31 (224)	0.32 (311)	0.30 (284)	0.27 (256)	0.29 (216)
(b)	0.38 (200)	0.45 (219)	0.47 (276)	0.46 (323)	0.50 (300)	0.45 (263)
ghost (294.80 Å) of Mg VIII 315.1 Å						
(a)	0.28 (456)	0.35 (726)	0.37 (946)	0.33 (793)	0.29 (682)	0.25 (586)
(b)	0.49 (576)	0.50 (657)	0.55 (807)	0.57 (919)	0.56 (782)	0.45 (759)
ghost (296.99 Å) of Mg VIII (bl) 317.09 Å						
(a)	0.63 (123)	0.77 (202)	0.65 (300)	0.64 (270)	0.60 (218)	0.58 (186)
(b)	0.89 (176)	1.06 (172)	1.20 (226)	1.13 (243)	1.06 (230)	0.80 (255)
ghost (300.08 Å) of Si VIII 319.77 Å						
(a)	0.05 (533)	0.07 (872)	0.05 (1321)	0.04 (1179)	0.03 (999)	0.03 (837)
(b)	0.07 (808)	0.07 (915)	0.08 (1182)	0.07 (1350)	0.07 (1232)	0.05 (1154)
ghost (336.24 Å) of Si VIII 319.77 Å						
(a)	0.06 (559)	0.08 (931)	0.05 (1387)	0.03 (1221)	0.03 (1031)	0.04 (864)
(b)	0.08 (864)	0.09 (975)	0.09 (1271)	0.06 (1442)	0.06 (1314)	0.06 (1207)
ghost (318.1 Å) of Fe XVI (bl Mg VIII Fe XII) 335.33 Å						
(a)	0.47 (38)	0.80 (67)	0.36 (99)	0.45 (84)	0.66 (67)	0.29 (80)
(b)	1.45 (24)	0.73 (55)	1.30 (59)	0.66 (79)	0.64 (74)	0.92 (55)
ghost (318.67 Å) of Fe XVI (bl Mg VIII Fe XII) 335.33 Å						
(a)	2.96 (56)	1.98 (122)	2.53 (134)	2.15 (122)	1.82 (112)	1.61 (103)
(b)	4.34 (59)	3.17 (94)	2.63 (135)	3.08 (131)	3.00 (122)	2.87 (106)
ghost (408.61 Å) of Mg VIII (2) 436.8 Å						
(a)	0.07 (558)	0.08 (877)	0.11 (1212)	0.08 (1091)	0.06 (849)	0.05 (720)
(b)	0.12 (964)	0.10 (1053)	0.14 (1299)	0.16 (1399)	0.13 (1277)	0.10 (1173)
ghost (409.0 Å) of Mg VIII (2) 436.8 Å						
(a)	0.03 (594)	0.05 (944)	0.06 (1345)	0.06 (1177)	0.07 (902)	0.05 (756)
(b)	0.05 (1078)	0.08 (1156)	0.06 (1482)	0.07 (1619)	0.07 (1440)	0.05 (1289)
ghost (704.67 Å) of Mg IX (368.070 IIo) 736.0 Å						
(a)	0.13 (93)	0.19 (130)	0.23 (194)	0.15 (191)	0.18 (172)	0.10 (161)
(b)	0.20 (139)	0.07 (153)	0.22 (170)	0.24 (192)	0.06 (193)	0.18 (183)
ghost (744.16 Å) of Ne VIII 770.77 Å						
(a)	0.48 (366)	0.47 (528)	0.48 (747)	0.43 (625)	0.43 (503)	0.36 (447)
(b)	0.69 (337)	0.64 (426)	0.72 (412)	0.65 (497)	0.60 (456)	0.57 (398)

3.4.7 The physical characteristics of the off-limb (1997 May 4) and on-disc (1997 October 16) regions

Table 3.8 presents as an example the densities and temperatures derived from the 16th October (on-disc) and May 4 (off-limb) 1997 averaged spectra. All the other spectra examined, in October and June, have similar values. Note:

- that the densities and temperatures deduced from different ions and line ratios are close. In particular, the direct measurements from the temperature-sensitive Si XI 580.9 Å/ 303.3 Å(IIo) ratio are close to the other values which assume ionization equilibrium. However, the Si XI 580.9 Å/ 604.1 Å ratio instead gives higher temperatures, independent of the calibration used. Also, the density deduced from the Si IX ratios is similar to that obtained from the Si X ratio, thus suggesting that no corrections due to photoionization are therefore necessary for Si IX, at these densities.
- how a different calibration affects the physical parameters. The different sensitivity curve adopted has the effect of changing absolute values of densities, temperatures, and element abundances deduced from line ratios, although these changes can be within the errors when both lines fall in the same detector. In any case, it is important to consider how a different calibration could affect the physical parameters.

  Table 3.8 shows that the differences due to the use of the second standard NIS calibration (1999) are small, within the errors in most cases (the first NIS standard calibration – 1996-1998 – produced larger differences).

3.4.8 The NIS 1 internal calibration

The information from all of the observations mentioned above was used to constrain the NIS 1 sensitivity, i.e. find the wavelength dependence with the use of the diagnostic method. The resulting calibration is presented in figure 3.28, with other calibrations, for comparison.

The other curves represent:

- the first CDS standard calibration, which was based on the ground calibration (*Bromage et al.*, 1996 and *Lang et al.*, 1999). The data from *Lang et al.* (1999) are also displayed in the figure. It is evident that the ground calibration was obtained at only a few wavelengths. The two measurements around 360 Å suggested a constant sensitivity in this region. The wavelength dependence is that determined from theoretical calculations of various intensity ratios.

Table 3.8: *Table of some of the densities and temperatures deduced from the 16th October (on-disc) and May 4 (off-limb) 1997 averaged spectra. Temperatures were calculated at constant density* $N_{\rm e} = 3.5\text{x}10^8$ *and with the ionization equilibrium calculations of* Arnaud and Rothenflug *(1985). In some cases, the values deduced from the NIS second standard calibration (1999) are also shown.*

	on-disc ratio (counts)	on-disc ratio (calibrated)	on-disc value	off-limb ratio (counts)	off-limb ratio (calibrated)	off-limb value	
$N_{\rm e}$(Fe XIV 353.831 / 334.172 Å)	1.45±0.35	0.85±0.20	$1.4\text{x}10^{10}\pm1.9\text{x}10^{10}$	0.99±0.14	0.58±0.08	$5.0\text{x}10^{9}\pm2.1\text{x}10^{9}$	
(standard calibration)					0.75±0.11	$1.0\text{x}10^{10}\pm4.1\text{x}10^{9}$	
$N_{\rm e}$(Fe XIII 359.8 / 348.183 Å)	0.75±0.06	0.71±0.06	$9.4\text{x}10^{8}\pm1.8\text{x}10^{8}$	0.68±0.03	0.65±0.03	$7.9\text{x}10^{8}\pm9.7\text{x}10^{7}$	
(standard calibration)					0.57±0.03	$6.0\text{x}10^{8}\pm7.3\text{x}10^{7}$	
$N_{\rm e}$(Fe XII 338.278/364.467 Å)	0.19±0.02	0.31±0.03	$1.4\text{x}10^{10}\pm4.7\text{x}10^{9}$	0.14±0.01	0.23±0.01	$6.3\text{x}10^{9}\pm1.2\text{x}10^{9}$	
(standard calibration)					0.21±0.01	$4.7\text{x}10^{9}\pm8.9\text{x}10^{8}$	
$N_{\rm e}$(Si X 356./347.4 Å)	0.76±0.02	0.73±0.01	$5.3\text{x}10^{8}\pm3.1\text{x}10^{7}$	0.65±0.01	0.62±0.01	$4.0\text{x}10^{8}\pm2.2\text{x}10^{7}$	
(standard calibration)					0.57±0.01	$3.3\text{x}10^{8}\pm1.9\text{x}10^{7}$	
$N_{\rm e}$(Si IX 349.9/341.9 Å)	3.06±0.07	2.71±0.06	$5.0\text{x}10^{8}\pm3.0\text{x}10^{7}$	2.57±0.05	2.27±0.04	$3.3\text{x}10^{8}\pm2.0\text{x}10^{7}$	
(standard calibration)					2.29±0.04	$3.3\text{x}10^{8}\pm2.0\text{x}10^{7}$	
$N_{\rm e}$(Si IX 349.9/345.1 Å)	1.09±0.02	1.03±0.01	$4.7\text{x}10^{8}\pm2.8\text{x}10^{7}$	1.00±0.01	0.95±0.01	$3.5\text{x}10^{8}\pm2.1\text{x}10^{7}$	
(standard calibration)					0.93±0.01	$3.3\text{x}10^{8}\pm2.0\text{x}10^{7}$	
$N_{\rm e}$(Mg VIII 315.038 / 317.038 Å)	3.04±0.13	3.07±0.13	$1.2\text{x}10^{8}\pm3.1\text{x}10^{7}$	2.83±0.12	2.86±0.12	$8.9\text{x}10^{7}\pm1.7\text{x}10^{7}$	
$N_{\rm e}$(Mg VIII 315.038 / 313.754 Å)	2.39±0.09	2.38±0.09	$1.9\text{x}10^{8}\pm6.3\text{x}10^{7}$	2.23±0.09	2.22±0.09	$1.3\text{x}10^{8}\pm3.5\text{x}10^{7}$	
$N_{\rm e}$(Mg VII 319.027 / 367.67 Å)	0.12±0.02	0.36±0.06	$9.4\text{x}10^{8}\pm3.1\text{x}10^{8}$	0.10±0.01	0.28±0.04	$6.7\text{x}10^{8}\pm1.4\text{x}10^{8}$	
(standard calibration)		0.24±0.04	$5.3\text{x}10^{8}\pm1.8\text{x}10^{8}$				
$N_{\rm e}$(O IV 625.853/608.397 Å)	0.07±0.01	0.06±0.00	$2.2\text{x}10^{10}\pm3.6\text{x}10^{9}$				
(standard calibration)		0.07±0.01	$2.5\text{x}10^{10}\pm4.0\text{x}10^{9}$				
$N_{\rm e}$(Fe XIII 203.8 (2) / 202.0 Å)	0.37±0.06	0.37±0.06	$1.8\text{x}10^{8}\pm1\text{x}10^{8}$	0.29±0.08	0.30±0.08	$1.8\text{x}10^{8}\pm1\text{x}10^{8}$	
$N_{\rm e}$(Fe X 175.3 (2) / 174.53	0.14±0.01	0.13±0.01	$1\text{x}10^{9}\pm2\text{x}10^{8}$	0.11±0.01	0.11±0.01	$6.7\text{x}10^{8}\pm8\text{x}10^{7}$	?
$N_{\rm e}$(Mg VIII 436.7 (2) / 430.465	1.42±0.11	1.79±0.12	$9.4\text{x}10^{8}\pm5\text{x}10^{8}$	1.39±0.08	1.61±0.09	$3.3\text{x}10^{8}\pm1.7\text{x}10^{8}$	
(436.7 Ånot ghost-corrected)	1.42±0.11	1.48±0.11	$2.1\text{x}10^{8}\pm1.\text{x}10^{8}$	1.39±0.08	1.45±0.08	$1.9\text{x}10^{8}\pm6\text{x}10^{7}$	
$N_{\rm e}$(Mg VII 280.7 / 431.2 (2) Å)	0.09±0.03	0.19±0.07	$5.3\text{x}10^{8}\pm2.5\text{x}10^{8}$				
$T_{\rm e}$(Si XII 520.7 Å/ Mg X 624.9 Å)	0.04±0.00	0.03±0.00	$1.2\text{x}10^{6}\pm2.8\text{x}10^{3}$	0.07±0.00	0.05±0.00	$1.2\text{x}10^{6}\pm1.0\text{x}10^{4}$	[a]
(standard calibration)					0.06±0.00	$1.2\text{x}10^{6}\pm2.9\text{x}10^{3}$	
$T_{\rm e}$(Si XII 520.7 Å/ Si XI 580.91 Å)	0.55±0.05	0.45±0.04	$1.0\text{x}10^{6}\pm1.1\text{x}10^{4}$	0.84±0.03	0.69±0.03	$1.1\text{x}10^{6}\pm7.3\text{x}10^{3}$	
(standard calibration)					0.73±0.03	$1.1\text{x}10^{6}\pm7.4\text{x}10^{3}$	
$T_{\rm e}$(Si XI 580.9 Å/ 303.3 Å) (IIo)	1.18±0.09	0.02±0.00	$3.5\text{x}10^{6}\pm6.4\text{x}10^{5}$	1.60±0.09	0.02±0.00	$1.6\text{x}10^{6}\pm2.8\text{x}10^{5}$	
$T_{\rm e}$(Si XI 580.9 Å/ 604.1 Å)	4.92±0.57	3.94±0.46	$7.0\text{x}10^{6}\pm1\text{x}10^{6}$	7.34±0.87	5.89±0.70	$4.1\text{x}10^{6}\pm5.9\text{x}10^{5}$	
$T_{\rm e}$(Fe XIV 334.2 Å/ Fe XIII 348.2 Å)	0.34±0.08	0.56±0.13	$1.5\text{x}10^{6}\pm9.0\text{x}10^{4}$	0.29±0.03	0.48±0.06	$1.5\text{x}10^{6}\pm4.2\text{x}10^{4}$	
(standard calibration)					0.35±0.04	$1.4\text{x}10^{6}\pm3.6\text{x}10^{4}$	
$T_{\rm e}$(Fe XIII 348.183 Å/ Fe XII 364.467 Å)	0.27±0.02	0.31±0.02	$1.1\text{x}10^{6}\pm1.8\text{x}10^{4}$	0.23±0.01	0.27±0.01	$1.1\text{x}10^{6}\pm1.0\text{x}10^{4}$	
$T_{\rm e}$ (Mg X 624.9 Å/ Mg IX 368 Å)	0.59±0.00	0.16±0.00	$9.7\text{x}10^{5}\pm2.2\text{x}10^{3}$	0.62±0.01	0.17±0.00	$9.8\text{x}10^{5}\pm2.3\text{x}10^{3}$	
(standard calibration)					0.16±0.00	$9.6\text{x}10^{5}\pm2.2\text{x}10^{3}$	
$T_{\rm e}$ (Mg IX 368 Å/ Mg VII 367.7 Å)	7.44±0.22	7.23±0.22	$8.8\text{x}10^{5}\pm4.1\text{x}10^{3}$	12.90±0.51	12.53±0.49	$9.5\text{x}10^{5}\pm4.4\text{x}10^{3}$	
$T_{\rm e}$ (Mg IX 368.07 Å/ Mg VIII 315.04 Å)	7.22±0.13	2.39±0.04	$9.1\text{x}10^{5}\pm4.2\text{x}10^{3}$	12.10±0.24	4.01±0.08	$1.0\text{x}10^{6}\pm4.7\text{x}10^{3}$	
(standard calibration)					5.82±0.11	$1.1\text{x}10^{6}\pm5.1\text{x}10^{3}$	
$T_{\rm e}$ (Fe XII 364.47 Å/ Fe X 345.72 Å)	0.81±0.03	0.67±0.03	$1.1\text{x}10^{6}\pm7.6\text{x}10^{3}$	1.25±0.03	1.04±0.03	$1.2\text{x}10^{6}\pm5.4\text{x}10^{3}$	
$T_{\rm e}$ (Fe XII 364.47 Å/ Fe XI 352.66 Å)	0.69±0.03	0.60±0.02	$1.1\text{x}10^{6}\pm1.0\text{x}10^{4}$	0.90±0.02	0.78±0.02	$1.2\text{x}10^{6}\pm8.3\text{x}10^{3}$	
$T_{\rm e}$(Fe XI 352.66 Å/ Fe X 345.72 Å)	1.18±0.02	1.11±0.02	$1.1\text{x}10^{6}\pm7.5\text{x}10^{3}$	1.39±0.02	1.32±0.02	$1.1\text{x}10^{6}\pm7.9\text{x}10^{3}$	
$T_{\rm e}$(O V 629.732 Å/ O IV 608.397 Å)	17.06±0.16	14.81±0.14	$2.3\text{x}10^{5}\pm5.3\text{x}10^{2}$				

[a] assuming photospheric abundances

- The *Landi et al.* (1997a) calibration, increased by a factor of 2. *Landi et al.* (1997a) were not able to assess an absolute value of the sensitivity, but suggested that the NIS 1 sensitivities needed to be increased by a factor of between 2.5 and 5, relative to NIS 2.

- The second CDS standard calibration, introduced into the CDS software in December 1998. The absolute value at 368 Å, where the brightest NIS 1 line is, was derived from the *Brekke et al.* (1999) study (with a reported accuracy of 25%). However, the coarse resolution ($\simeq$ 5 Å) of the rocket flight spectrum, and the low signal-to-noise, did not allow a measurement of the wavelength dependence for NIS 1.

Superimposed on the off-limb calibration (thick solid line), some of the lines used to determine the wavelength dependence, are shown. The results from the on-disc observations, are not shown, since there is not much difference from the off-limb case (most of the NIS 1 lines are coronal), and the off-limb spectra have the advantage that they are not affected by scattered light blending with cool lines. The line identifications can be found in Table C.2.

For each ratio of two lines from the same ion, it was possible to determine the sensitivity ratio between the values at the wavelengths where the lines are, directly from the observed intensities (in phot-events) and the theoretical emissivity, *independent of element abundances, differential emission measure distribution, and ionization equilibrium.* These ratio values have been normalized and are shown in Figure 3.28. The following groups of lines were found suitable for calibration purposes, because they are well represented in CHIANTI-SERTS comparisons, are bright and do not appear to be blended in off-limb quiet sun observations:

- **Fe XVI** (335.41, 360. Å)

  Intensities from active region observations were used. In these cases, the 335.4 Å is all Fe XVI. Note that this measurement constrains the sensitivity ratio between those wavelengths. The *Landi et al.* (1997a) calibration also is also consistent with this line ratio.

- **Fe XII** (346.852, 352.106, 364.467 Å)

  These lines have already been described in Chapter 2. They are bright lines, free of blends in the off-limb spectra, and the agreement between CHIANTI and SERTS data is excellent. There is no reason why differences in the CDS observations should arise. These indicate an almost constant sensitivity at those wavelengths. The 352.106 Å line was used to normalize the ratio values of the lines shown in Figure 3.28.

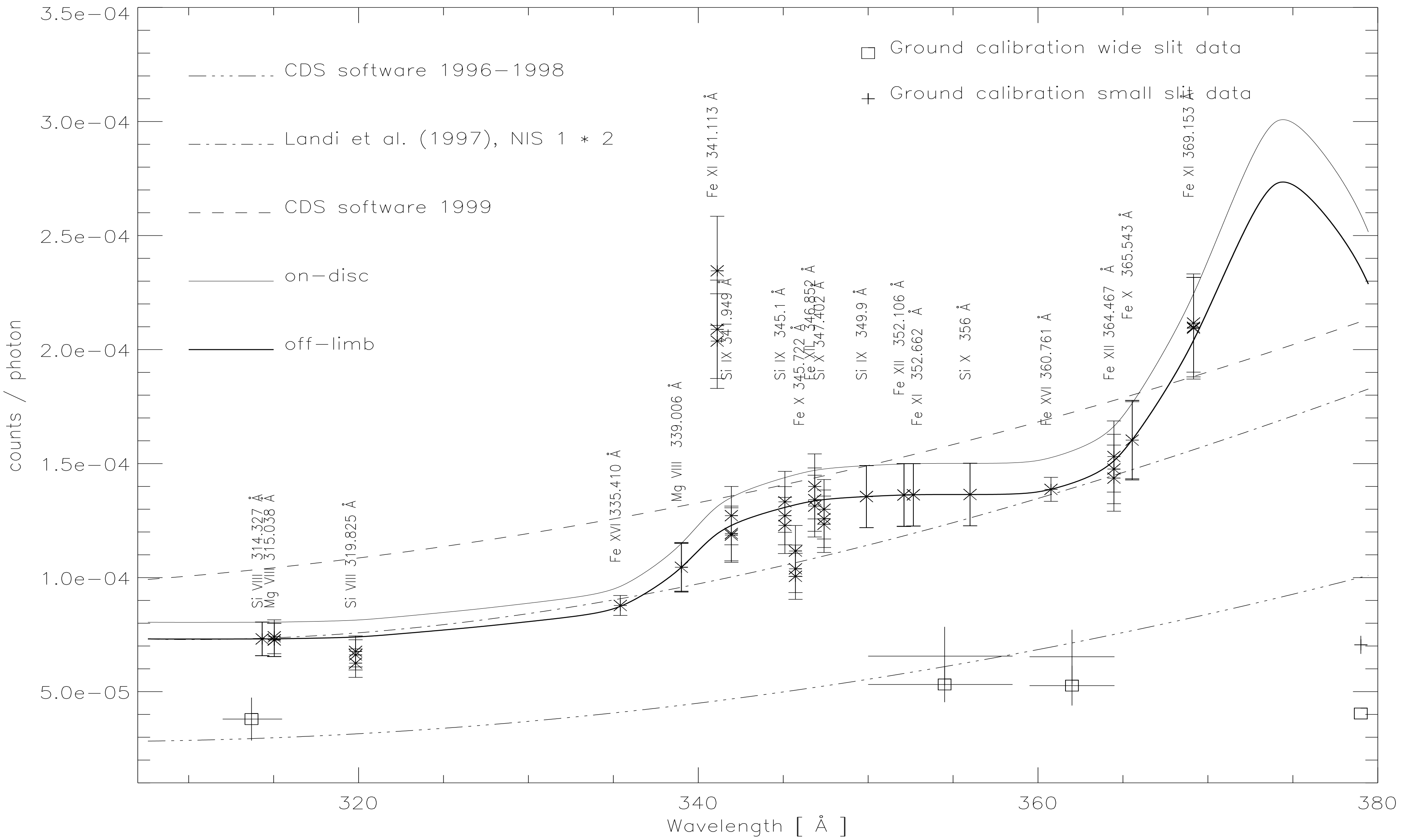

Figure 3.28: *The proposed CDS NIS 1 sensitivities (solid line), compared with the other calibrations.*

- **Fe XI** (341.113, 352.662, 356.519, 369.153 Å)

  The 369.153/352.662 is a branching ratio, well represented in the SERTS-89 observations. These lines are bright and well resolved, in particular in off-limb spectra, and require a large increase in the sensitivity toward the higher wavelengths. The Fe XI 341.113 Å is a bright well resolved line, that furthermore is well represented in the SERTS-89 case (also noted by *Young et al.*, 1998). However, in *all* the CDS spectra examined, this line is not well represented, and would require a much higher sensitivity than in the curve presented in Figure 3.28, where the 352.662 Å line was used as a reference line to normalize the other lines. The Fe XI 341.113 Å line therefore, must be blended in the CDS spectra. In the SERTS-89 spectrum, a very weak unidentified line is reported at 340.969 Å, with an intensity 0.17 times the intensity of the Fe XI line. Off-limb radial intensity profiles of the ratio of the 341.113 Å with the other Fe XI lines (not shown here), although changing, do not present large variations, and therefore the unidentified line that blends the 341.113 Å line must be a coronal line, and moreover not a high-temperature line (otherwise it would not contribute in the quiet sun on-disc or off-limb spectra). This therefore still leaves more than 30% of the observed line un-accounted for. This discrepancy would increase if a lower sensitivity at 341 Å is adopted. The 356.519 Å line is blended with an Fe XIV 356.641 Å line and is not directly usable.

- **Fe X** (345.722, 365.543 Å)

  These two bright lines form a branching ratio. The 365.543 is blended with a bright Ne V line in on-disc observations. In the off-limb observations, this line should be free of blending, and can be used in conjunction with the 345.722 Å to constrain the relative sensitivity between those wavelengths. This branching ratio would require a lower sensitivity at 345 Å than is presented here, and is therefore not in agreement with the results, unlike the SERTS-89 case. The region between 340 and 350 Å therefore has inconsistencies that will require more investigations.

- **Mg VIII** (315.038, 335.253, 339.006 Å)

  The Mg VIII (315.038, 339.006) lines always show a constant ratio (within few %), independently of the observed region and provide a good constraint on the relative sensitivity between those wavelengths. The 335.253 Å line is only usable as a check, because even when the Fe XVI contribution is absent, there is a non-negligible contribution from a previously unidentified Fe XII line, as explained below.

Also note:

- **Si IX and Si X**

Although the Si IX and Si X lines are density-sensitive, and were therefore not used as calibration lines, their normalised ratios are also plotted in Figure 3.28, to show that, within the errors, these ratios are all consistent with the curve of sensitivity that is presented here. As already shown, however, for the purposes of density diagnostics, a different sensitivity curve in the 340-360 Å region does not significantly affect the results. If Fe X is to be believed, then the sensitivity curve should be less constant, with effect of having slightly lower densities as derived from the Si IX and the Si X ratios. However, this would leave unexplained why the Fe XI and Fe XII would be wrong (being the Fe XII well represented in other spectra as SERTS).

- In most of the observations analysed the above lines provide similar ratios (only some are shown in Figure, and show the small scatter in the ratio values from different observations).

- The apparently unconstrained regions of the sensitivity curve are in fact constrained by lines of other ions, that are not shown in the figure. Among them are all the Fe XIII, Fe XIV, Fe XV lines that span almost the *whole* NIS 1 channel (from 308 to 373 Å), already shown in the active region spectrum. These confirm the calibration proposed here. Also, there are related lines in other channels which constrain the NIS sensitivity subject to the calibration of the other detectors. For example, the group of O III/N III lines $\sim$ 374 Å can be used in conjunction with the O III lines seen in GIS 4 and NIS 2. These also indicate much increased sensitivity at these wavelengths. The (uncertain) downturn at the end of the detector is constrained by the presence of the Ca IX-Na VII blend at 378 Å.

- The absolute values of the NIS 1 calibration are deduced from a relative calibration study that is described in Section 3.4.10.

- The absolute values almost coincide at 368 Å with the only reliable NIS 1 measurement cited in *Brekke et al.* (1999), producing *excellent agreement* with the rocket flight calibration.

In all the on-disc observations examined the sensitivity of all the NIS channel apparently increases by about 10%, as already indicated by the direct NIS 1 / GIS 2 comparison of the overlapping region (Section 3.4.6). These variations cannot be ascribed to variations in effective areas, nor to non-linear effects, for example, and remain unexplained. Departures from the optically thin limit can be ruled out, as are variations of the physical conditions for the coronal lines that are present in NIS 1, that are not substantially changing, as shown in Figure 3.25. The only effect that affects the NIS 1 channel as a whole is the scattered light (see e.g. Figure 3.38), which could therefore be related to this peculiar fact.

In fact, different selections of the background can easily account for a change in the line intensities up to factors of 15%. However, a 10% difference, even if real, is still well within all the other uncertainties in the observations and atomic physics (that are intrinsically difficult to estimate), that can be summed to at least 20-30%.

3.4.9 The NIS 2 internal calibration (first order)

Unlike the NIS 1 channel, there are not many lines emitted by the same ion that are seen in NIS 2. Moreover, some of these lines are complex blends between 'cool and hot' lines, and with second order lines, as already shown. The useful lines can be grouped into two classes:

1. The chromospheric and transition region (cool) lines that are only visible in on-disc quiet sun observations. Active region observations have to be avoided because of strong blending with second order lines.
2. Coronal lines observed in off-limb quiet sun observations. The active region observations produce second order lines that blend with some of the lines in the off-limb observations. The off-limb observations are required to eliminate the contribution from the cool lines to the coronal lines, as already shown in Section 3.4.6 (see e.g. Figure 3.27).

All the on-disc quiet sun NIS observations analysed have been used to constrain the sensitivity using the first group of lines, while all the off-limb quiet sun observations have been used in the other case. The information from such off-limb and on-disc observations is summarised in Figure 3.29, proposing a new calibration, scaled to match the *Brekke et al.* (1999) value at 584 Å. As in the NIS 1 case, the result is compared with the other calibrations in the last three years:

- the first CDS standard calibration, that was based on the ground calibration of *Bromage et al.* (1996). The most reliable measurements obtained there were from the wide slit He I (584.3, 537 Å) observations. Both these observations indicated the same sensitivity value of 0.00040. The measurement at 537 Å was adopted, and a linear variation along the detector was introduced to explain the O III (525.8/599.6 Å) ratio observed in-flight. The ground He I measurements were therefore not in agreement with the in-flight observations.
- The *Landi et al.* (1997a) calibration. The main features are an almost constant sensitivity along the central part of the channel, with an increase at the shorter wavelengths and a downturn at the end of the detector.

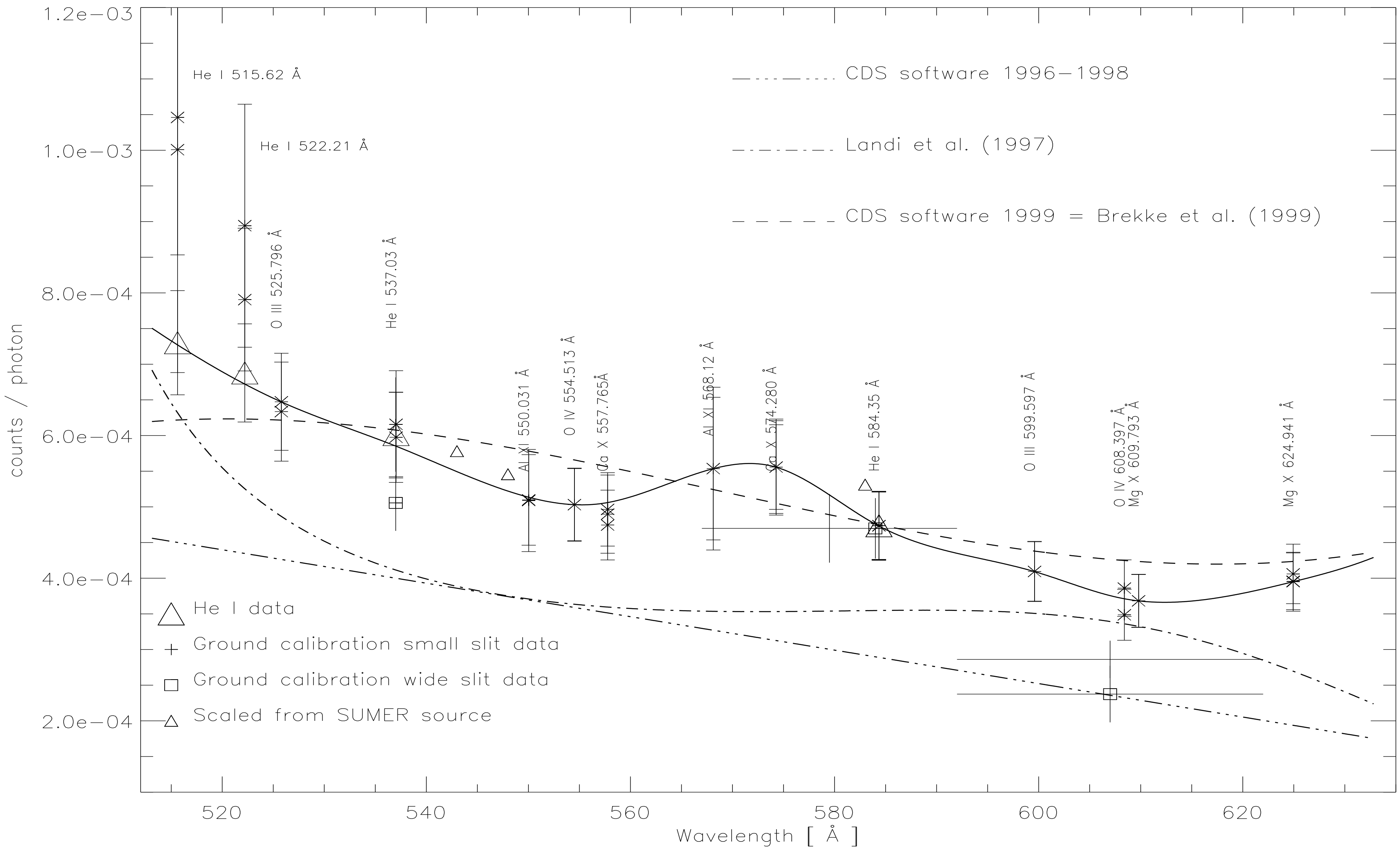

Figure 3.29: *The proposed CDS NIS 2 sensitivities (solid line), compared with the other calibrations.*

- The second CDS standard calibration, introduced into the CDS software in December 1998. This calibration is based on the *Brekke et al.* (1999) study. For the NIS 2 channel, in fact, the signal was sufficient to allow an estimate of the background intensity. The main features are an increased absolute sensitivity, by a factor of 1.6 compared to the previous ground calibration, a rise at the high wavelength and a downturn at wavelengths below 530 Å. The cited accuracy in terms of absolute values ranges from 15% at 584 Å, to 25% at either end of the spectrum. However, additional uncertainties (although ruled out in their paper) could be due to the fact that the rocket flight observed the sun as a star, and the CDS observations were not simultaneous.

- The revised ground calibration data of *Lang et al.* (1999) are displayed in the figure, with the same symbols as in their report. The main changes, compared to the previous ground calibration, are an increase in the absolute values of the wide slit He I data. In addition other measurements (done with wide and narrow slit). It should be noted that the measured values reported in *Lang et al.* (1999) are not in good agreement with the expected theoretical curve. The revised absolute value at 584 Å is instead in excellent agreement with the value derived by *Brekke et al.* (1999), suggesting that the NIS 2 sensitivity did not appreciably change over a long period of time (unlike the NIS 1 one). However, the other He I value at 537 Å (square box in the figure), nor the measurements around 610 Å(that indicate a very low sensitivity), are not in agreement with the value measured by *Lang et al.* (1999), as the Figure shows. While the measurement at 610 Å is not reliable (B. Bromage, 1999, priv. comm.), the He I measurement is, and the discrepancy cannot be easily explained, unless in-flight modifications of the NIS 2 sensitivity have taken place.

The transition region and chromospheric lines

The useful lines are:

O III (525.796, 599.597 Å) lines. Note that in active region spectra the 525.796 Å line is partly blended with Fe XVI 263 (second order). There is also an O III line at 597.817 Å which is weak and might be blended, although it is always in good agreement with the other two lines.

O IV lines. The O IV 608.397 was used in conjunction with any of the other O IV lines at 553-556 Å. The O IV line (three transitions) visible at 617.0 Å is very weak and partly blended with second order lines.

He I lines (515.62, 522.21, 537.03, 584.35 Å).

As noted by previous authors (e.g. *Andretta and Jones*, 1997, and *Macpherson and Jordan*, 1999), all the lines of the sequence present similar characteristics, independent of the type of solar region observed. In particular, the ratios of the line intensities versus the 584.35 Å intensity is very constant, as shown in Table 3.9, which reproduces the calibrated He I averaged intensities of *Vernazza and Reeves* (1978), together with the theoretical values in the optically thin approximation (using the Arcetri spectral code). This finding has been confirmed by the analysis of the on-disc NIS 2 spectra. This fact makes these lines suitable for an in-flight calibration. Unfortunately, there are no well calibrated recent He I line intensities, and the only set of well calibrated values are indeed those reported in *Vernazza and Reeves* (1978), which rely partly on previous rocket flights. However, assuming that the calibration is correct, then the CDS observations imply that the sensitivities at those wavelengths are those indicated by the large triangles in Figure 3.29(the values have been normalized at 584 Å). The values that the sensitivities should have if the He I emission is optically thin (a strong assumption for the He I lines, see the above-cited studies of *Andretta and Jones*, 1997, and *Macpherson and Jordan*, 1999, and references therein), are also shown in the Figure. It is interesting to note that:

- the 584 and 537 Å lines appear to be effectively optically thin.
- the sensitivity at 537 Å, derived from the *Vernazza and Reeves* (1978) calibrated values (and from the theoretical emissivities) are in excellent agreement with the *Brekke et al.* (1999) value, but not with the ground calibration value.
- The *Vernazza and Reeves* (1978) of the other two He I lines require an upturn of the sensitivity at the shorter wavelengths, and not an upturn, as suggested by *Brekke et al.* (1999). However, this upturn is not as steep as suggested by the *Landi et al.* (1997a) study.

Table 3.9: *The ratios of the calibrated He I intensities of* Vernazza and Reeves *(1978) for the various solar regions (QS: quiet sun; CH: coronal hole; AR: active region; cc: cell centres; net: network), with the theoretical ratios, calculated assuming optically thin emission. Note the small variations of these ratios, and how close they are with the predicted values. At the bottom, the calibrated intensity of the 584.35 Å is reported, to show the large variations of the observed intensities.*

ratio	QS avg	QS cc	QS net	CH avg	CH cc	CH net	AR	AR active	calculated
515.62/584.35 Å	0.028	0.028	0.031	0.024	0.022	0.032	0.027	0.027	0.021
522.21/584.35 Å	0.050	0.048	0.053	0.054	0.054	0.055	0.043	0.045	0.044
537.03/584.35 Å	0.130	0.128	0.132	0.136	0.132	0.142	0.113	0.115	0.133
I (584.35 Å)	544.98	426.22	827.71	250.12	221.93	300.94	5470.68	7233.50	

The coronal lines

NIS 2 observes the bright doublets: Ca X (557.765, 574.010 Å); Al XI (550.031, 568.12 Å) and Mg X (609.793, 624.941Å). In on-disc observations the Ca X 574.010 Å is blended with a C III 574.279 Å and the Mg X 609.793 is blended with a bright O IV 609.829 Å line. The Al XI 568.12 line is blended in active region observations with two second order lines (Fe XV and Al IX at 284.1 Å), and in on-disc observations with Ne V at 568.417 Å. In particular, the two Mg X lines have been used to determine the relative calibration between 610 Åand 625 Å, using off-limb observations.

Other lines

As in the NIS 1 case, other lines have been used to obtain a consistent calibration relative to the other CDS channels, and are not shown for simplicity in Figure 3.29. These are emitted from other ions that produce lines seen in the other CDS detectors. More details of the relative calibration are given in Section 3.4.10. Just as an example, the upturn at the longer wavelengths has the effect of reducing the calibrated intensity of one of the brightest lines in NIS 2, O V 629.732 Å, by almost a factor of 2. Only with this upturn it is possible to find a good agreement with the multiplet O V lines seen in GIS 4 $\simeq$ 760 Å. Also, when deducing emission measure (or DEM) the O V 629.732 Å line is out by a factor of 2 in intensity, compared to the other lines, when using the first standard CDS calibration.

Concluding comments on the NIS 1 and NIS 2 sensitivities

The only direct in-flight absolute calibration study is that of *Brekke et al.* (1999). In considering a detailed comparison with the diagnostic study presented here, it should be noted that the coarse resolution ($\simeq$ 5 Å) of the rocket flight spectrum limited the evaluation of the instrumental background, increasing the uncertainty. The spectra have been binned into six wavelength regions, and the background estimated from the (very) few regions free of line emission. With this in mind, the main differences (almost within the errors) between the in-flight calibration study of *Brekke et al.* (1999) and the NIS 2 relative calibration presented here are:

- the upturn in the calibration presented here at the shorter wavelengths. However, the downturn at wavelengths below 530 Å is regarded as uncertain by these authors, because of low signal.

- a decreased sensitivity at 610 Å, as derived from the O III and O IV lines. However, the region around 600 Å proved difficult to fit and was discarded in their work.

- The region between the He I 537 and 584 Å shows more variation in sensitivity in the calibration proposed here. However, one of the six wavelength bins (the central one) in the *Brekke et al.* (1999) study spanned the 545-575 Å range, and therefore the two calibrations are not in disagreement (the averaged sensitivity in the 545-575 Å range is similar).

Note that the upturn at the longer wavelengths was not expected from theoretical calculations of the sensitivity. In general, most of the ground calibration measurements, and the theoretical variation of the sensitivity are not in accordance with either direct in-flight (*Brekke et al.*, 1999) cross-calibrations, nor with the in-flight diagnostic study presented here. Therefore, there is no sensible reason why the even fewer ground measurements or theoretical curves for the NIS 1 channel (and the GIS ones for that matter) should be reliable, at least if accuracies of 20-30% are sought. Also, in terms of relative values between NIS 1 and NIS 2, the ground calibration data imply a much lower sensitivity than that one measured in flight, by both the present and the (*Brekke et al.*, 1999) study, by factors of more than 2. These differences could be due to the reflectivity of the optical parts (e.g. mirrors, gratings) having changed in-flight, or to the different illuminations, for example. The theoretical curves, based on the expected reflectivity of the optical parts were also not very accurate, probably, or in any case can not be directly applied to the in-flight data. Similarly, also the second order NIS sensitivities, and the GIS sensitivities presented here significantly differ from the pre-flight measurements, as Figure 3.30 shows.

More comments on the NIS 1 and 2 calibration can be found in Sections 3.4.11 and 3.4.12, where particular observations are presented.

3.4.10 The cross-calibration between all the NIS and GIS channels, first and second order

The whole process is an iterative one, only briefly outlined below. First, the internal calibration within each GIS channel was studied, following the same method explained in detail for the NIS 1 and NIS 2 case. However, only in the GIS 1 and GIS 2 spectra are there pairs of lines emitted by the same ion, which can be used for this purpose. The complete calibration of all the GIS spectra therefore relies on the cross-calibration with the NIS detectors. Also, the relative calibration between NIS 1 and NIS 2 depends on the GIS calibration. The procedure was to assume valid the internal NIS 1 and NIS 2 sensitivity curves shown above, and then cross-calibrate each GIS channel.

Cross-calibration between the NIS 1 and GIS 2

The cross-calibration in the overlapping region is straightforward, since both channels detect the same lines. The Si VIII 319.825 Å has been used to scale the relative sensitivities. This line has been chosen because it is the brightest line, is un-blended, not density-dependent, and is the only one in the overlapping region that is not significantly affected by the ghosting. In fact, it creates two weak ghosts in regions free of lines, and therefore it was possible to reconstruct this line. The values of the relative NIS 1/ GIS 2 sensitivity at 319.825 Å (as in Figure 3.23) have been deduced from the off-limb observations, where the contribution from the scattered light, that not only creates a background diffuse light, but is variable in time, is not present. The May, June, and October 1997 off-limb observations are all in accordance, suggesting that in that period the relative sensitivity between NIS 1 and GIS 2 had not appreciably changed. As already mentioned, the on-disc observations are not in close agreement with the off-limb ones, and present an apparent decrease of the GIS / NIS sensitivity of about 10%.

Other lines in the GIS 2 channel were used to derive the wavelength dependence. These include lines from Fe XIV, Fe XV, Fe XVI, Si X, Si VIII, Mg VII, using off-limb NIS/GIS and GIS active region observations.

Cross-calibration between NIS 1 and GIS 1

This is also relatively straightforward, since NIS 1 and GIS 1 observe in any on-disc or off-limb case many Fe X, XI, XII, and, in active region spectra, also bright Fe XIII and Fe XIV lines. Density-sensitivity is an issue for many of these lines, so the off-limb quiet sun spectra are again the best, because the density there is well established. Some of the useful bright lines are:

- Fe X: 345.722, 365.543 Å (NIS 1); 174.534, 177.242, 184.543, 190.0 Å (GIS 1).
- Fe XI: 352.662, 356.519, 369.153 Å (NIS 1); 180.4, 182.169, 188.2 (188.232+188.299) Å (GIS 1).
- Fe XII: 346.852, 352.106, 364.467 Å (NIS 1); 192.393, 193.521, 195.100 Å (GIS 1).
- Fe XIV: 334.172 Å (NIS 1); 211.320 Å (GIS 1).

Cross-calibration between NIS 1 and GIS 3

The calibration of the central part of GIS 3 was carried out using the bright Mg VIII and Mg VII lines visible in the 429-437 Å region with the Mg VIII and Mg VII lines seen in

NIS 1. The quiet sun off-limb observations are the most suitable, because the ghosting of the GIS lines can be checked (see below), and because blending with second order lines is negligible. The Mg VIII lines are more suitable than the Mg VII lines, because they vary much less with time.

GIS 3 also observes many Mg IX lines (439.176, 441.199, 443.973, 448.293 Å) that could be used in conjunction with the bright resonance 368.070 Å line observed in NIS 1. However, although excellent agreement among the GIS lines was found, no agreement with the 368.070 Å line could be found, confirming the SERTS-89 results described above.

Cross-calibration between the NIS 1 and NIS 2

The diagnostic method is almost unapplicable, since in NIS 1 and NIS 2 there are only a few cool lines emitted by the same ions. Only quiet sun on-disc observations, where the scattered light adds uncertainty in the measurements, can be used. Furthermore, these lines are weak and partly blended. The lines observed in NIS 1 are:

(1) a blend of Ne IV and Ne V at 357.8 Å. Some observations suggest that these lines are further blended.

(2) A weak and blended Ne V 359.382 Å line.

(3) a complex group of O III and N III transitions observed at 374 Å.

These lines were used as a cross-check of the relative NIS 1/ NIS 2 calibration in conjunction with the Ne IV (541.128, 542.072, 543.891 Å), Ne V (568.417, 569.824, 572.331), and O III (525.796, 599.597 Å) lines observed in NIS 2 (the N/O relative abundance can be checked using the N III and O III lines observed in GIS 4). Agreement with the results obtained from the other cross-calibrations was found in most cases.

On-disc cross-calibration between NIS 2, GIS 3, GIS 4

Since most of the NIS 2 lines are transition region lines, and the second order sensitivity is non-negligible, only the quiet sun on-disc observations could be used. Careful examination of any temporal changes had to be considered here, as already explained with the example in Figure 3.26 (above). The lines used for both the internal GIS 3 and GIS 4 calibration, and for the cross-calibration are (note that some of them are density-sensitive and were given lower importance in the iteration process) :

- O III: 702.8 (2), 703.8 (2) Å (GIS 4); 525.796, 597.817 (bl Ca VIII), 599.597 Å (NIS 2).

- O V: 758.676, 759.441, 760.4 (2), 761.127, 762.003 Å (GIS 4); 629.732 Å (NIS 2).
- Ne IV: 469.9 (4) Å (GIS 3); 541.128 (bl Fe XIV IIo 270.507), 542.072, 543.891 (bl Si X IIo 271.98) Å (NIS 2).
- Ne V: 416.194, 481.3, 482.982 Å (GIS 3); 568.4 (bl), 569.8 (2), 572.3 (3) Å (NIS 2). The lines observed in GIS are of limited use, for various reasons.
- Ne VI: 399.821 (bl), 401.136 (bl), 401.926, 435.648 Å (GIS 3); 558.594 (bl Ne VII), 562.803 (NIS 2).
- Ne VII: 465.22 Å (GIS 3); 559.948, 561.7 (2), 564.528 (bl) Å (NIS 2).
- S IV 661.4 (2), 748.392, 750.220, 753.759 (GIS 4).

Cross-calibration between NIS 1 and GIS 4 (first and second order)

The first order cross-calibration was not really possible, since only a few lines (with temperature and density effects) could be used: Mg IX 706.060, 749.551 Å (GIS 4) with the 368 Å (NIS 1), and the weak 782.338 Å at the very end of GIS 4, with the Mg VIII lines seen in NIS 1.

The cross-calibration of the second order GIS 4 sensitivity, however, is straightforward, since almost all the second order lines in GIS 4 are also observed in NIS 1. However, these lines are heavily blended with on-disc lines, and therefore only the off-limb quiet sun observations were usable.

Other cross-calibrations (first and second order)

Many other cross-calibrations and checks were possible, using many other lines.

The quiet sun off-limb observations were used to directly cross-calibrate the NIS 2 second order sensitivity (at the higher wavelengths), with the same lines, observed in first order in NIS 1 (and also to cross-calibrate with GIS 2). The rest of the NIS 2 second order sensitivity was directly cross-calibrated using the same lines seen in first order in GIS 2 (although strong ghosting limited part of the GIS 2). To do this, Off-limb quiet sun and active region spectra were used.

Part of the second order GIS 3 sensitivity was derived with a direct cross-calibration of the same lines seen in first order in GIS 1, using off-limb quiet sun spectra and active region spectra (these lines, in fact, are otherwise: (1) blended in the GIS 3 spectra with cool lines; (2) not visible, since they are all high-temperature lines (Fe XII, Fe XIII, Fe XIV)).

The rest of the GIS 3 second order could only be inferred from theoretical predictions of the lines intensities, with the use of DEM analyses of active regions and off-limb quiet sun regions.

Many other indirect cross-calibrations could be possible, using for example lines that have similar contribution functions, emitted by different elements, whenever it was possible to independently check the relative element abundance, and with the use of DEM analyses. Just as a simple example, the Mg/Si abundance can easily be checked using the two 315.038 (Mg VIII) and 316.205 (Si VIII) Å lines, observed in NIS 1 (in GIS 2 the Si VIII 316.205 has serious problems of ghosting and contaminations and cannot be used). These lines are close in wavelength and therefore their ratio of intensity does not depend on the calibration. Once the Mg/Si is known, then the Si VII line seen in GIS 2 $\sim$ 275.5 Å (others are blended, in some cases, with lines and ghosts) were used to cross-calibrate that spectral region with all the other regions (GIS 3, NIS 1) where all the Mg VII lines are seen, using DEM analyses to account for the (small) differences in the contribution functions the Si VII and Mg VII have.

Final results and comments

Figure 3.30 shows the CDS first and second order sensitivities that were derived from all the cross-calibrations from all the data analysed. These sensitivities have been applied to all the spectra presented in this thesis, unless explicitly stated otherwise.

Since it is virtually impossible to present all the observations, fits to the data, $DEMs$, cross-calibrations done, what has been done instead is to use all the spectra presented throughout this thesis to show the validity of this calibration. Examples in the form of Tables and synthetic spectra have already been given, while others (some more detailed) are given in the following Sections and in the Appendices. With this calibration, most of the lines are well represented within a 20% or so, at least for the lines emitted by the same ion (examples of lines emitted by different ions and that are not in agreement with theory have also been and will be given throughout the rest of this thesis). Considering all the uncertainties in either the atomic physics, the observations, the ghosting problem in the GIS spectra, this is already an achievement. However, this does not mean that this calibration can be considered to be correct within a 20% throughout all the channels. There are spectral regions where direct cross-calibrations were possible, and where suitable observations were analysed in order to derive direct sensitivity ratios, using bright lines. These regions are therefore well constrained. Other regions were also well constrained by having a large number of lines for a cross-calibration. Many other regions in the GIS spectra were so heavily affected by cross-ghosting that was not possible to use them

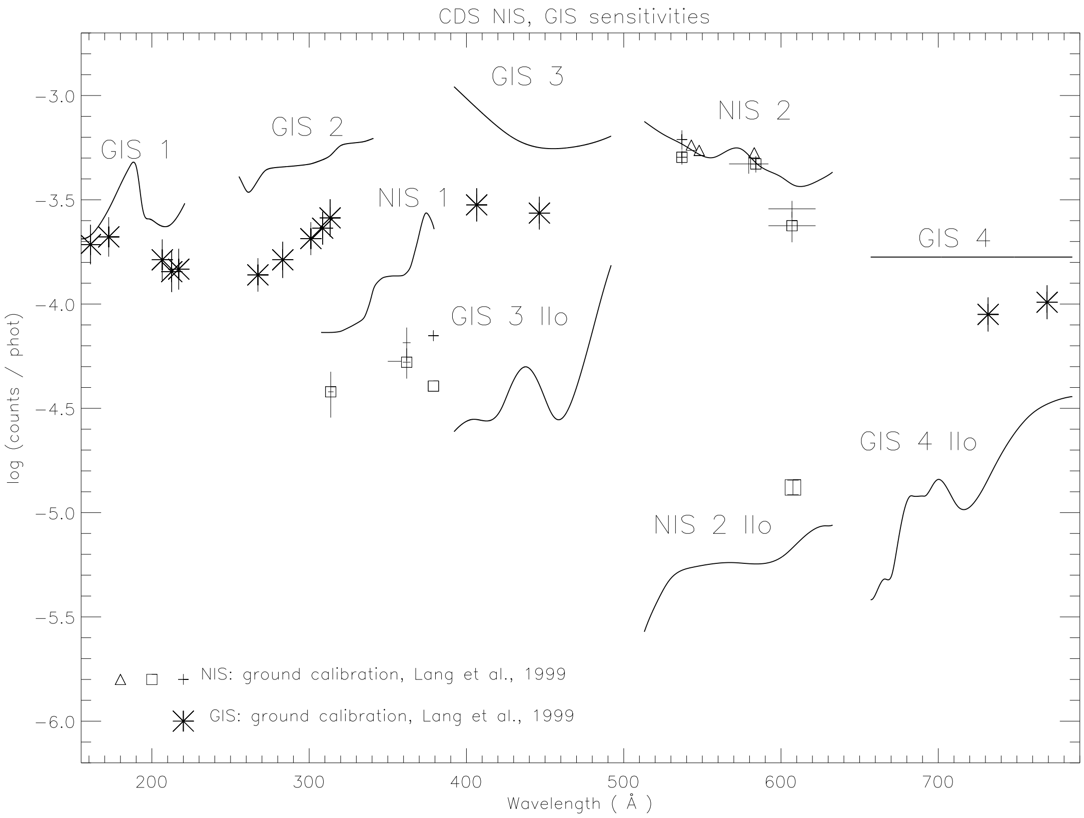

Figure 3.30: *The CDS NIS and GIS sensitivities (solid lines), first and second order, applied to the data presented in this thesis. All the pre-flight NIS and GIS measurements (*Lang *et al., 1999) are also displayed.*

to constrain the sensitivity. Wherever possible, a smooth sensitivity curve (within each channel) was sought.

The main features worth noting, comparing the calibration presented here with the pre-flight measurements (*Lang et al.*, 1999), keeping in mind that all the cross-calibration was based on fixing the absolute value at 584 Å to be in agreement, are:

- much higher sensitivities in NIS 1 and in all the GIS channels.
- A much lower second order NIS 2 sensitivity (the only pre-flight measurement of the NIS 2 sensitivity, at 608 Å, is shown in Figure).

It is also interesting to note:

- on average, the relative sensitivities between all the GIS channels (and the NIS 1) do not differ much between the pre-flight ones and this in-flight study.
- The variations with wavelength, within each GIS channel, can be regarded as consistent with the pre-flight GIS measurements, except for GIS 2 where a steeper wavelength dependence was measured on the ground.
- The same GIS wavelength variations follow the predicted sensitivities (see, e.g., Figure 36 in *Bromage et al.* (1996) and Figure 33 in *Lang et al.*, 1999), in most spectral regions. The predicted sensitivities were evaluated from the reflectivities of the telescope, the scan mirror, the grating, and the efficiencies of the detectors. They present a minimum sensitivity at 210 Å, followed by a rise with a sharp drop at 270 Å followed by a shallow increase until 380 Å, where the sensitivity decreases again, to reach a minimum in GIS 3 around 430 Å, and to then increase again at higher wavelengths. The GIS 4 spectral region was expected to have a constant sensitivity.
- The second order curves suggest that most of the sensitivity variations are due to the telescope and scan mirror reflectivities, rather than to the grating efficiency in second order. In fact, their wavelength variations are consistently similar to the correspondent first order variations (that have been derived independently).

3.4.11 The off-limb observation of May 4th 1997. The effect of different calibrations and ionization equilibrium calculations. Full list of identified lines

Since all the GIS off-limb spectra examined have shown similar characteristics (i.e. DEM, abundances, densities), only the results from the May 4th 1997 observation are presented here. These off-limb spectra are particularly simple to model, because they represent a simple structure. The plasma along the line of sight is almost isothermal, and has almost constant density. These spectra are therefore particularly suitable not only for calibration purposes (because variations in the line intensities due to temperature and/or density effects are minimised), but also as a check for the ionization state of the plasma, as described below.

The contribution functions have been calculated at constant density $N_{\rm e}$ = 3.5x10^8, as deduced from the observed lines (Table 3.8), except for two Fe XII transitions (338.278 and 335.339 Å) for which a constant density $N_{\rm e}$ = 2x10^{10} was assumed (for reasons that are described below). Note that an error in the calibration does not significantly affect the derived density. The *Arnaud and Rothenflug* (1985) ionization equilibrium calculations have been used, with CHIANTI version 2.0 (plus recent Fe XIV calculations, *Storey et al.*, 1999, and Mg IX calculations, P. Young, priv. comm.). The photospheric abundances of *Grevesse and Anders* (1991) have been adopted, except for Na (+0.2), Al (+0.2), and Ca (+0.6) [numbers in parentheses are usual differences in dex from photospheric values].

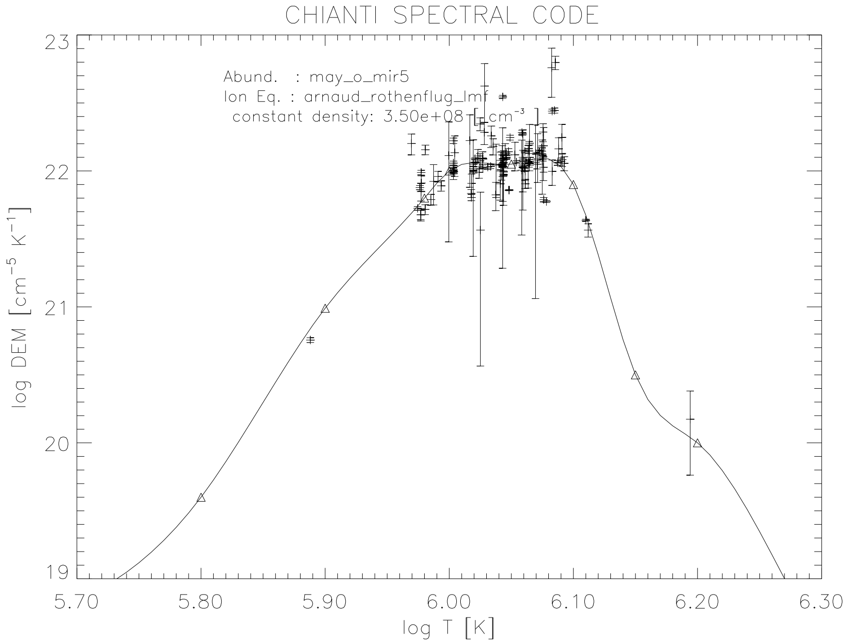

Figure 3.31: *The derived DEM for the off-limb quiet sun observation of May 4th 1997.*

Figure 3.31 shows the DEM that was found. The lack of (or weak) emission in cool (e.g. chromospheric and transition region) and hot (Fe XVI) lines constrains the DEM values away of a well-defined peak, around a million degree. However, The 'width' of the DEM shows that the plasma is not strictly isothermal. However, the peak temperature of the DEM distribution is in agreement with the temperatures derived from the line ratios (shown in Table 3.8).

Table 3.10: *Results of the analysis for the lines (first and second order) from the off-limb quiet sun observation of May 4th 1997. Some of the lines used for the calculation of the DEM of Figure 3.31, those used for cross-calibration between detectors (and orders), and a few other ones, are shown. The calculations were at constant density* $N_e = 3.5\text{x}10^8$*, with the* Arnaud and Rothenflug *(1985) ionization equilibrium. Note the good agreement between lines of the same ion (confirming the adopted calibration), between lines of the same element (confirming the DEM), and between lines of different elements (confirming the adopted abundances). For some lines, the corresponding values obtained using the 'second standard CDS calibration (CDS software, 1999)' are shown. Note that: (1) no lines were observed at either higher and lower temperatures; the lines having log* $T_{\text{eff}} < 6$ *were weak, and suffered from intensity variations with time, and were not used for the cross-calibration. (2) considering the doublet lines and in general lines of the same ion, the 'second standard' calibration has larger relative deviations (up to 30%); (3) considering particular wavelength regions, the 'second standard' calibration produces deviations up to 50%, as is the case for the bright lines at the shortest wavelengths in NIS 1 (e.g. Mg VIII 315.0 Å and Si VIII 319.8 Å.*

Ion	λ_{th} (Å)	λ_{ob} (Å)	Transition	I_{ob}	I_{th}/ I_{ob}	+/-	Det	log T_{eff}	log T_{max}	frac
O IV	555.263	555.1	2s2 2p $^2P_{3/2}$ - 2s 2p2 $^2P_{1/2}$	0.8	0.68	0.12	N 2	5.37	5.27	
Ne VI	562.803	562.9	2s2 2p $^2P_{3/2}$ - 2s 2p2 $^2D_{5/2}$	2.9	1.21	0.13	N 2	5.89	5.63	
Ne VII	561.728	561.7	2s2p $^3P_2$ - 2p2 $^3P_2$	4.6	1.04	0.11	N 2	5.97	5.72	0.83
Ne VII	561.378		2s2p $^3P_1$ - 2p2 $^3P_1$						5.72	0.17
Ne VII	465.22	465.2	2s2 $^1S_0$ - 2s2p $^1P_1$	142.2	0.76	0.08	G 3	5.98	5.72	
Mg VII	434.917	434.9	2s22p2 $^3P_2$ - 2s2p3 $^3D_3$	36.9	1.23	0.16	G 3	5.98	5.80	0.87
Mg VII	434.72		2s22p2 $^3P_2$ - 2s2p3 $^3D_2$						5.80	0.13
Mg VII	431.313	431.3	2s22p2 $^3P_1$ - 2s2p3 $^3D_2$	25.0	1.23	0.18	G 3	5.98	5.80	0.78
Mg VII	431.188		2s22p2 $^3P_1$ - 2s2p3 $^3D_1$						5.80	0.22
Mg VII	429.14	429.2	2s22p2 $^3P_0$ - 2s2p3 $^3D_1$	12.5	0.84	0.15	G 3	5.98	5.80	
Mg VII	367.674	367.7	2s22p2 $^3P_2$ - 2s2p3 $^3P_2$	84.7	0.61	0.07	N 1	5.98	5.81	0.77
Mg VII	367.683		2s22p2 $^3P_2$ - 2s2p3 $^3P_1$						5.81	0.23
Mg VII	363.772	363.8	2s22p2 $^3P_0$ - 2s2p3 $^3P_1$	13.7	0.73	0.12	N 1	5.98	5.81	
Mg VII	365.234	365.1	2s22p2 $^3P_1$ - 2s2p3 $^3P_2$	26.2	1.23	0.16	N 1	5.98	5.81	0.36
Mg VII	365.176		2s22p2 $^3P_1$ - 2s2p3 $^3P_0$						5.81	0.33
Mg VII	365.243		2s22p2 $^3P_1$ - 2s2p3 $^3P_1$						5.81	0.26
Mg VII	278.402	278.4	2s22p2 $^3P_2$ - 2s2p3 $^3S_1$	52.9	1.17	0.16	G 2	5.99	5.81	0.68
Si VII	278.443		2p4 $^3P_1$ - 2s.2p5 $^3P_2$						5.77	0.29
Mg VII	276.154	276.1	2s22p2 $^3P_0$ - 2s2p3 $^3S_1$	18.1	0.91	0.31	G 2	5.99	5.81	0.51
Si VII	275.667		2p4 $^3P_1$ - 2s.2p5 $^3P_1$						5.77	0.45
Si VII	275.353	275.3	2p4 $^3P_2$ - 2s.2p5 $^3P_2$	60.6	0.91	0.12	G 2	5.99	5.77	
Na VIII	411.166	411.1	2s2 $^1S_0$ - 2s.2p $^1P_1$	22.8	1.13	0.15	G 3	5.99	5.86	
Mg VIII	782.338	781.9	2p $^2P_{3/2}$ - 2s.2p2 $^4P_{3/2}$	6.7	0.77	0.59	G 4	6.00	5.90	
Mg VIII	430.465	430.5	2p $^2P_{1/2}$ - 2s.2p2 $^2D_{3/2}$	104.0	1.04	0.11	G 3	6.00	5.91	
Mg VIII	315.039	315.0	2p $^2P_{3/2}$ - 2s.2p2 $^2P_{3/2}$	264.8	1.05	0.11	N 1	6.00	5.91	
			(standard calibration)	185.8	1.50	0.15	N 1			
Mg VIII	315.039	630.0	2p $^2P_{3/2}$ - 2s.2p2 $^2P_{3/2}$	443.7	0.63	0.07	N 2	6.00	5.91	
Mg VIII	315.039	315.1	2p $^2P_{3/2}$ - 2s.2p2 $^2P_{3/2}$	290.8	0.96	0.10	G 2	6.00	5.91	
Mg VIII	313.754	313.7	2p $^2P_{1/2}$ - 2s.2p2 $^2P_{1/2}$	119.2	0.92	0.10	N 1	6.00	5.92	
Mg VIII	313.754	627.6	2p $^2P_{1/2}$ - 2s.2p2 $^2P_{1/2}$	100.5	1.09	0.16	N 2	6.00	5.92	
Mg VIII	339.006	339.0	2p $^2P_{3/2}$ - 2s.2p2 $^2S_{1/2}$	62.5	1.07	0.11	N 1	6.00	5.92	
			(standard calibration)	49.7	1.34	0.14	N 1			
Mg VIII	428.319	428.2	2s.2p2 $^2D_{5/2}$ - 2p3 $^2D_{5/2}$	4.3	0.78	0.27	G 3	6.00	5.92	0.55
Mg VIII	428.245		2s.2p2 $^2D_{3/2}$ - 2p3 $^2D_{3/2}$						5.92	0.35
Al VIII	387.957	775.4	2p2 $^3P_2$ - 2s.2p3 $^3D_3$	39.9	0.69	0.38	G 4	6.02	5.92	0.84
Al VIII	387.822		2p2 $^3P_2$ - 2s.2p3 $^3D_2$						5.92	0.14
Ne VIII	780.324	780.1	1s2 2s $^2S_{1/2}$ - 1s2 2p $^2P_{1/2}$	157.7	1.69	0.20	G 4	6.02	5.79	

Table 3.10: *(continued)*

Ion	λ_{th} (Å)	λ_{ob} (Å)	Transition	I_{ob}	I_{th}/I_{ob}	+/-	Det	log T_{eff}	log T_{max}	frac
Ne VIII	770.409	770.8	1s2 2s $^2S_{1/2}$ - 1s2 2p $^2P_{3/2}$	294.1	1.81	0.20	G 4	6.02	5.79	
Al VIII	325.276	325.4	2p2 $^3P_1$ - 2s.2p3 $^3P_0$	13.5	1.42	0.28	N 1	6.02	5.92	0.37
Al VIII	325.292		2p2 $^3P_1$ - 2s.2p3 $^3P_2$						5.92	0.33
Al VIII	325.338		2p2 $^3P_1$ - 2s.2p3 $^3P_1$						5.92	0.29
Si VIII	314.327	314.4	2s22p3 $^4S_{3/2}$ - 2s2p4 $^4P_{1/2}$	125.0	1.03	0.11	N 1	6.02	5.91	
Si VIII	314.327	628.8	2s22p3 $^4S_{3/2}$ - 2s2p4 $^4P_{1/2}$	107.7	1.20	0.91	N 2	6.02	5.91	
Si VIII	319.826	319.8	2s22p3 $^4S_{3/2}$ - 2s2p4 $^4P_{5/2}$	335.9	1.11	0.12	G 2	6.02	5.91	
Si VIII	319.826	319.9	2s22p3 $^4S_{3/2}$ - 2s2p4 $^4P_{5/2}$	323.0	1.15	0.12	N 1	6.02	5.91	
			(standard calibration)	220.3	1.69	0.17	N 1			
Ca X	574.01	574.1	3s $^2S_{1/2}$ - 3p $^2P_{1/2}$	20.9	0.94	0.10	N 2	6.02	5.82	
			(standard calibration)	23.0	0.85	0.09	N 2			
Ca X	557.765	557.8	3s $^2S_{1/2}$ - 3p $^2P_{3/2}$	39.6	1.00	0.10	N 2	6.02	5.82	
			(standard calibration)	36.1	1.10	0.11	N 2			
Fe IX	244.909	489.1	3p6 $^1S_0$ - 3p5.3d $^3P_1$	69.9	0.90	0.14	G 3	6.02	5.94	
Fe IX	241.739	483.3	3p6 $^1S_0$ - 3p5.3d $^3P_2$	140.8	1.18	0.16	G 3	6.02	5.94	
Al VIII	328.185	328.2	2p2 $^3P_2$ - 2s.2p3 $^3P_2$	34.3	0.97	0.16	N 1	6.02	5.92	0.69
Al VIII	328.232		2p2 $^3P_2$ - 2s.2p3 $^3P_1$						5.92	0.23
Mg IX	706.058	705.8	2s2 $^1S_0$ - 2s.2p $^3P_1$	45.8	0.52	0.08	G 4	6.02	5.98	
Na IX	694.147	694.2	1s2.2s $^2S_{1/2}$ - 1s2.2p $^2P_{1/2}$	6.0	3.13	2.84	G 4	6.03	5.92	
Mg IX	368.07	736.0	2s2 $^1S_0$ - 2s.2p $^1P_1$	1069.1	0.92	0.14	G 4	6.03	5.98	
Fe IX	171.073	171.1	3p6 $^1S_0$ - 3p5.3d $^1P_1$	3766.6	1.09	0.11	G 1	6.03	5.96	
Mg IX	368.07	368.1	2s2 $^1S_0$ - 2s.2p $^1P_1$	1060.8	0.94	0.09	N 1	6.03	5.98	
S VIII	198.553	198.7	2s2.2p5 $^2P_{3/2}$ - 2s.2p6 $^2S_{1/2}$	140.0	0.60	0.13	G 1	6.03	5.88	0.66
Fe XI	198.545		3s2.3p4 $^1D_2$ - 3s2.3p3(2d*).3d $^3P_1$						6.11	0.32
Mg IX	749.55	749.7	2s.2p $^1P_1$ - 2p2 $^1D_2$	9.0	0.27	0.13	G 4	6.03	5.99	
Si X	277.255	277.0	2p $^2P_{3/2}$ - 2s.2p2 $^2S_{1/2}$	213.5	1.07	0.12	G 2	6.03	6.13	0.38
Si VIII	277.054		2s22p3 $^2D_{5/2}$ - 2s2p4 $^2D_{5/2}$						5.90	0.30
Si VIII	276.838		2s22p3 $^2D_{3/2}$ - 2s2p4 $^2D_{3/2}$						5.90	0.13
Mg VII	277		2s22p2 $^3P_1$ - 2s2p3 $^3S_1$						5.81	0.11
Mg VIII	335.253	335.3	2p $^2P_{1/2}$ - 2s.2p2 $^2S_{1/2}$	73.1	1.05	0.11	N 1	6.03	5.92	0.65
Fe XII	335.339		3s2.3p3 $^2D_{3/2}$ - 3s.3p4 $^2D_{3/2}$						6.16	0.33 [14]
O VI	184.117	184.0	1s2 2p $^2P_{3/2}$ - 1s2 3s $^2S_{1/2}$	72.4	0.62	0.13	G 1	6.03	5.51	0.67
O VI	183.937		1s2 2p $^2P_{1/2}$ - 1s2 3s $^2S_{1/2}$						5.51	0.33
O VI	173.079	173.1	1s2 2p $^2P_{3/2}$ - 1s2 3d $^2D_{5/2}$	116.2	0.74	0.13	G 1	6.04	5.51	0.60
O VI	172.935		1s2 2p $^2P_{1/2}$ - 1s2 3d $^2D_{3/2}$						5.51	0.33
S IX	221.241	442.5	2s2.2p4 $^3P_2$ - 2s.2p5 $^3P_1$	46.4	1.01	0.44	G 3	6.04	6.00	
Al IX	286.377	286.6	2s2.2p $^2P_{3/2}$ - 2s.2p2 $^2P_{1/2}$	15.5	1.39	0.36	G 2	6.04	6.03	
Al IX	282.422	282.6	2s2.2p $^2P_{1/2}$ - 2s.2p2 $^2P_{1/2}$	28.9	0.93	0.17	G 2	6.04	6.03	
Al IX	305.045	305.3	2s2.2p $^2P_{3/2}$ - 2s.2p2 $^2S_{1/2}$	14.3	1.00	0.26	G 2	6.04	6.03	
Si IX	349.873	349.9	2s22p2 $^3P_2$ - 2s2p3 $^3D_3$	226.6	1.00	0.10	N 1	6.04	6.03	0.84
Si IX	349.794		2s22p2 $^3P_2$ - 2s2p3 $^3D_2$						6.03	0.16
Si IX	349.873	699.8	2s22p2 $^3P_2$ - 2s2p3 $^3D_3$	267.1	0.85	0.17	G 4	6.04	6.03	0.84
Si IX	349.794		2s22p2 $^3P_2$ - 2s2p3 $^3D_2$						6.03	0.16
Si IX	341.949	342.0	2s22p2 $^3P_0$ - 2s2p3 $^3D_1$	99.4	1.03	0.10	N 1	6.04	6.03	
Si IX	341.949	684.4	2s22p2 $^3P_0$ - 2s2p3 $^3D_1$	103.8	0.98	0.82	G 4	6.04	6.03	
Si IX	296.117	592.6	2s22p2 $^3P_2$ - 2s2p3 $^3P_2$	949.9	0.32	0.03	N 2	6.04	6.03	0.72 [15]
Si IX	296.213		2s22p2 $^3P_2$ - 2s2p3 $^3P_1$						6.03	0.28
Si IX	345.124	345.1	2s22p2 $^3P_1$ - 2s2p3 $^3D_2$	238.6	1.03	0.10	N 1	6.04	6.03	0.77
Si IX	344.951		2s22p2 $^3P_1$ - 2s2p3 $^3D_1$						6.03	0.23
Si IX	345.124	690.3	2s22p2 $^3P_1$ - 2s2p3 $^3D_2$	200.4	1.23	0.44	G 4	6.04	6.03	0.77
Si IX	344.951		2s22p2 $^3P_1$ - 2s2p3 $^3D_1$						6.03	0.23
Si IX	292.8	585.7	2s22p2 $^3P_1$ - 2s2p3 $^3P_0$	230.7	0.90	0.11	N 2	6.04	6.03	0.40
Si IX	292.856		2s22p2 $^3P_1$ - 2s2p3 $^3P_1$						6.03	0.32
Si IX	292.763		2s22p2 $^3P_1$ - 2s2p3 $^3P_2$						6.03	0.27
Si IX	225.024	450.2	2s22p2 $^3P_1$ - 2s2p3 $^3S_1$	230.3	1.04	0.19	G 3	6.04	6.04	0.69
S IX	225.22		2s2.2p4 $^3P_1$ - 2s.2p5 $^3P_1$						6.00	0.11
Si IX	227	454.0	2s22p2 $^3P_2$ - 2s2p3 $^3S_1$	288.2	0.97	0.16	G 3	6.04	6.04	
Fe X	365.543	365.6	3s2.3p5 $^2P_{1/2}$ - 3s.3p6 $^2S_{1/2}$	74.2	0.93	0.10	N 1	6.04	6.04	
			(standard calibration)	66.0	1.04	0.11	N 1			
Fe X	345.723	345.7	3s2.3p5 $^2P_{3/2}$ - 3s.3p6 $^2S_{1/2}$	133.9	1.19	0.12	N 1	6.04	6.04	
			(standard calibration)	124.5	1.28	0.13	N 1			
Fe X	345.723	691.5	3s2.3p5 $^2P_{3/2}$ - 3s.3p6 $^2S_{1/2}$	141.0	1.13	0.50	G 4	6.04	6.04	
Fe X	225.161		3s2.3p5 $^2P_{3/2}$ - 3s2.3p4(1d).3d $^2D_{5/2}$						6.04	0.20
Fe X	324.763	324.7	3s2.3p4(3p).3d $^4D_{7/2}$ - 3s.3p5(3p*).3d $^4F_{9/2}$	13.3	0.84	0.19	N 1	6.05	6.04	
Fe X	177.243	177.3	3s2.3p5 $^2P_{3/2}$ - 3s2.3p4(3p).3d $^2P_{3/2}$	2133.2	0.83	0.08	G 1	6.05	6.05	

[14] First identification

[15] Must be a blend with an unidentified line in first order

Table 3.10: *(continued)*

Ion	λ_{th} (Å)	λ_{ob} (Å)	Transition	I_{ob}	I_{th}/ I_{ob}	+/-	Det	log T_{eff}	log T_{max}	frac	
Fe X	174.534	174.7	3s2.3p5 $^2P_{3/2}$ - 3s2.3p4(3p).3d $^2D_{5/2}$	3375.8	0.90	0.09	G 1	6.05	6.05		
Fe X	184.543	184.6	3s2.3p5 $^2P_{3/2}$ - 3s2.3p4(1d).3d $^2S_{1/2}$	759.0	0.88	0.09	G 1	6.05	6.05		
Fe XII	186.884	186.8	3s2.3p3 $^2D_{5/2}$ - 3s2.3p2(3p).3d $^2F_{7/2}$	261.9	0.81	0.09	G 1	6.05	6.16	0.49	
FE VIII	186.599								5.64	0.36	AC
Fe XII	186.851		3s2.3p3 $^2D_{3/2}$ - 3s2.3p2(3p).3d $^2F_{5/2}$						6.16	0.14	
Mg X	609.793	609.8	1s2.(1s).2s $^2S_{1/2}$ - 1s2.(1s).2p $^2P_{3/2}$	364.2	1.55	0.15	N 2	6.05	6.04		
			(standard calibration)	316.7	1.78	0.18	N 2				
Mg X	624.941	625.0	1s2.(1s).2s $^2S_{1/2}$ - 1s2.(1s).2p $^2P_{1/2}$	180.4	1.55	0.16	N 2	6.05	6.04		
			(standard calibration)	168.3	1.66	0.17	N 2				
Fe XI	202.706	202.7	3s2.3p4 $^1D_2$ - 3s2.3p3(2d*).3d $^1P_1$	180.6	0.86	0.22	G 1	6.05	6.11	0.75	
S VIII	202.61		2s2.2p5 $^2P_{1/2}$ - 2s.2p6 $^2S_{1/2}$						5.88	0.16	
Fe XI	358.621	358.6	3s2.3p4 $^3P_0$ - 3s.3p5 $^3P_1$	40.8	0.98	0.10	N 1	6.05	6.11	0.75	
Fe X	358.413		3s2.3p4(3p).3d $^4F_{9/2}$ - 3s.3p5(3p*).3d $^4F_{9/2}$						6.04	0.23	
S X	776.373	776.3	2s22p3 $^4S_{3/2}$ - 2s22p3 $^2P_{3/2}$	6.0	1.15	0.78	G 4	6.06	6.11		
Fe XI	182.169	182.3	3s2.3p4 $^3P_1$ - 3s2.3p3(4s*).3d $^3D_2$	459.1	0.61	0.07	G 1	6.06	6.11	0.85	
Fe X	182.31		3s2.3p5 $^2P_{1/2}$ - 3s2.3p4(3p).3d $^2P_{3/2}$						6.05	0.15	
Fe XI	341.113	341.1	3s2.3p4 $^3P_2$ - 3s.3p5 $^3P_1$	75.4	0.63	0.06	N 1	6.06	6.11		
Fe XI	352.662	705.2	3s2.3p4 $^3P_2$ - 3s.3p5 $^3P_2$	176.2	1.11	0.39	G 4	6.06	6.11		
Fe XI	369.153	369.2	3s2.3p4 $^3P_1$ - 3s.3p5 $^3P_2$	54.7	1.07	0.11	N 1	6.06	6.11		
			(standard calibration)	59.2	0.99	0.10	N 1				
Fe XI	369.153	738.1	3s2.3p4 $^3P_1$ - 3s.3p5 $^3P_2$	62.9	0.93	0.56	G 4	6.06	6.11		
Fe XI	352.662	352.7	3s2.3p4 $^3P_2$ - 3s.3p5 $^3P_2$	177.1	1.10	0.11	N 1	6.06	6.11		
			(standard calibration)	156.8	1.24	0.12	N 1				
Fe XI	180.408	180.5	3s2.3p4 $^3P_2$ - 3s2.3p3(4s*).3d $^3D_3$	2182.8	0.98	0.10	G 1	6.06	6.11		
Al X	332.789	332.8	2s2 $^1S_0$ - 2s.2p $^1P_1$	104.1	1.14	0.13	N 1	6.06	6.09		
			(standard calibration)	70.4	1.68	0.19	N 1				
Fe XI	188.232	188.3	3s2.3p4 $^3P_2$ - 3s2.3p3(2d*).3d $^3P_2$	1406.5	0.85	0.09	G 1	6.06	6.11	0.72	
Fe XI	188.299		3s2.3p4 $^3P_2$ - 3s2.3p3(2d*).3d $^1P_1$						6.11	0.26	
S X	259.496	519.2	2s22p3 $^4S_{3/2}$ - 2s2p4 $^4P_{3/2}$	129.2	1.19	0.21	N 2	6.06	6.13		
Si X	356.012	711.8	2p $^2P_{3/2}$ - 2s.2p2 $^2D_{5/2}$	127.6	1.05	0.38	G 4	6.06	6.13	0.76	
Si X	356.05		2p $^2P_{3/2}$ - 2s.2p2 $^2D_{3/2}$						6.13	0.24	
Si X	356.012	356.0	2p $^2P_{3/2}$ - 2s.2p2 $^2D_{5/2}$	129.9	1.03	0.10	N 1	6.06	6.13	0.76	
Si X	356.05		2p $^2P_{3/2}$ - 2s.2p2 $^2D_{3/2}$						6.13	0.24	
Si X	258.372	258.5	2p $^2P_{3/2}$ - 2s.2p2 $^2P_{3/2}$	321.0	0.86	0.09	G 2	6.06	6.13		
Si X	261.063	261.2	2p $^2P_{3/2}$ - 2s.2p2 $^2P_{1/2}$	133.3	1.06	0.13	G 2	6.06	6.13		
Si X	258.372	516.8	2p $^2P_{3/2}$ - 2s.2p2 $^2P_{3/2}$	353.8	0.78	0.09	N 2	6.06	6.13		
Si X	347.403	347.4	2p $^2P_{1/2}$ - 2s.2p2 $^2D_{3/2}$	208.4	1.06	0.11	N 1	6.06	6.13		
Si X	347.403	694.7	2p $^2P_{1/2}$ - 2s.2p2 $^2D_{3/2}$	293.1	0.76	0.29	G 4	6.06	6.13		
Si X	271.983	272.0	2p $^2P_{1/2}$ - 2s.2p2 $^2S_{1/2}$	105.4	1.03	0.12	G 2	6.07	6.13		
Si IX	227.361		2s22p2 $^1D_2$ - 2s2p3 $^1P_1$						6.03	0.31	
Al IX	284.042	284.5	2s2.2p $^2P_{3/2}$ - 2s.2p2 $^2P_{3/2}$	79.7	1.11	0.14	G 2	6.07	6.03	0.76	
Fe XV	284.16		3s2 $^1S_0$ - 3s3p $^1P_1$						6.29	0.24	
Fe XII	227.406	454.9	3s2.3p3 $^2P_{1/2}$ - 3s2.3p2(3p).3d $^2P_{1/2}$	20.7	1.07	0.97	G 3	6.07	6.16	0.62	
Fe XII	346.852	346.9	3s2.3p3 $^4S_{3/2}$ - 3s.3p4 $^4P_{1/2}$	51.7	0.90	0.09	N 1	6.07	6.16		
			(standard calibration)	48.1	0.97	0.10	N 1				
Fe XII	352.106	352.1	3s2.3p3 $^4S_{3/2}$ - 3s.3p4 $^4P_{3/2}$	102.4	0.92	0.09	N 1	6.07	6.16		
			(standard calibration)	91.3	1.04	0.10	N 1				
Fe XII	364.467	364.5	3s2.3p3 $^4S_{3/2}$ - 3s.3p4 $^4P_{5/2}$	138.3	0.95	0.10	N 1	6.07	6.16		
			(standard calibration)	117.7	1.11	0.11	N 1				
Fe XII	352.106	704.2	3s2.3p3 $^4S_{3/2}$ - 3s.3p4 $^4P_{3/2}$	101.5	0.92	0.37	G 4	6.07	6.16		
Fe XII	364.467	728.5	3s2.3p3 $^4S_{3/2}$ - 3s.3p4 $^4P_{5/2}$	123.7	1.05	0.47	G 4	6.07	6.16		
Fe XII	193.521	193.6	3s2.3p3 $^4S_{3/2}$ - 3s2.3p2(3p).3d $^4P_{3/2}$	828.5	0.84	0.09	G 1	6.07	6.16		
Fe XII	338.278	338.3	3s2.3p3 $^2D_{5/2}$ - 3s.3p4 $^2D_{5/2}$	32.1	0.89	0.10	N 1	6.07	6.16		
Fe XII	195.118	195.2	3s2.3p3 $^4S_{3/2}$ - 3s2.3p2(3p).3d $^4P_{5/2}$	1103.8	0.99	0.10	G 1	6.08	6.16		
Fe XIII	321.4	321.6	3s2 3p2 $^3P_2$ - 3s 3p3 $^3P_1$	14.0	1.17	0.26	G 2	6.08	6.20	0.66	
Fe X	321.732		3s2.3p4(3p).3d $^4D_{5/2}$ - 3s.3p5(3p*).3d $^4F_{7/2}$						6.04	0.23	
Fe XIII	240.696	481.4	3s2 3p2 $^3P_0$ - 3s 3p3 $^3S_1$	29.1	0.81	0.30	G 3	6.08	6.20	0.84	
Al VII	240.777		2s22p3 $^2D_{5/2}$ - 2s2p4 $^2P_{3/2}$						5.78	0.14	
Al XI	568.12	568.2	1s2.(1s).2s $^2S_{1/2}$ - 1s2.(1s).2p $^2P_{1/2}$	6.4	2.02	0.22	N 2	6.08	6.16		
			(standard calibration)	6.7	1.92	0.20	N 2				
Al XI	550.031	550.1	1s2.(1s).2s $^2S_{1/2}$ - 1s2.(1s).2p $^2P_{3/2}$	12.5	2.08	0.21	N 2	6.08	6.16		
			(standard calibration)	11.1	2.34	0.24	N 2				
Si XI	580.907	580.9	2s2 $^1S_0$ - 2s.2p $^3P_1$	12.5	0.44	0.05	N 2	6.08	6.19		
S XI	281.401	281.5	2s22p2 $^3P_0$ - 2s2p3 $^3D_1$	17.8	1.21	0.28	G 2	6.08	6.24		
Si XI	303.324	606.7	2s2 $^1S_0$ - 2s.2p $^1P_1$	560.5	0.42	0.05	N 2	6.08	6.20		
Si XI	604.147	604.3	2s.2p $^1P_1$ - 2p2 $^1D_2$	2.1	0.19	0.03	N 2	6.09	6.20		
Fe XIII	359.842	359.7	3s2 3p2 $^3P_1$ - 3s 3p3 $^3D_1$	24.5	0.99	0.11	N 1	6.09	6.20	0.55	

Table 3.10: *(continued)*

Ion	λ_{th} (Å)	λ_{ob} (Å)	Transition	I_{ob}	I_{th}/I_{ob}	+/-	Det	log T_{eff}	log T_{max}	frac
Fe XIII	359.642		3s2 3p2 $^3P_1$ - 3s 3p3 $^3D_2$						6.20	0.43
Fe XIII	320.809	320.8	3s2 3p2 $^3P_2$ - 3s 3p3 $^3P_2$	13.2	0.77	0.18	G 2	6.09	6.20	
Fe XIII	348.183	348.2	3s2 3p2 $^3P_0$ - 3s 3p3 $^3D_1$	55.0	0.92	0.11	N 1	6.09	6.20	
Fe XIII	202.044	202.1	3s2 3p2 $^3P_0$ - 3s2 3p 3d $^3P_1$	493.9	0.87	0.13	G 1	6.09	6.21	
Fe XIV	274.2	274.1	3s2 3p $^2P_{1/2}$ - 3s 3p2 $^2S_{1/2}$	37.5	0.89	0.14	G 2	6.09	6.25	0.81
Si VII	274.174		2p4 $^3P_1$ - 2s.2p5 $^3P_0$						5.77	0.19
Si XII	520.665	520.8	1s2.2s $^2S_{1/2}$ - 1s2.2p $^2P_{1/2}$	8.6	1.09	0.11	N 2	6.11	6.26	
Fe XIV	334.172	334.2	3s2 3p $^2P_{1/2}$ - 3s 3p2 $^2D_{3/2}$	18.2	1.14	0.17	N 1	6.11	6.24	
			(standard calibration)	12.3	1.68	0.25	N 1			

Table 3.10 presents a selection of lines, with some of those used for the calculation of the DEM of Figure 3.31, and those useful for cross-calibration between detectors (and between first and second order). Note:

- the good agreement (in most cases within 10%) between lines of the same ion, also including the lines seen in second order, thus confirming the validity of the adopted NIS/GIS calibration.
- The good agreement between lines of the same element, thus confirming the validity of the DEM.
- The good agreement between lines of different elements, thus confirming the validity of the adopted abundances.
- The problems with the Li-like ions Ne VIII, Mg X, Al XI, Na IX (and also O VI, although only partially). See below for a discussion of it.
- The 1999 standard CDS calibration fails to represent the doublet lines well nor in general pairs of lines of the same ion, with deviations from expected intensities of up to 30%. Note that density- or temperature- dependent effects of this size can be ruled out as a cause. So, unless all the theoretical intensities of all the ions are wrong, or basic assumptions (such as the fact that the lines are optically thin) fail, the 1999 standard CDS calibration appear to be at fault (the first standard CDS calibration was even less accurate).
- Considering particular wavelength regions, the 1999 CDS standard calibration produces intensity deviations of up to 50-60%, as is the case for all the bright lines at the shortest wavelengths in NIS 1 (e.g. Mg VIII 315.0 Åand Si VIII 319.8 Å which appear weaker than expected). These deviations are independent of the ionization equilibrium calculations, since only particular spectral regions are affected while other lines of the same ions, observed in the different CDS channels, are well represented.

- Many lines exhibit the same deviations as were found in the SERTS-89 (and other) spectra. For example, with the adopted calibration, the Fe XII 338.278 Å transition is not well represented. To increase the theoretical intensity a much higher density is required, as already noted in the SERTS spectra. Assuming a density $N_e = 2\text{x}10^{10}$, this line becomes well represented. But the Fe XII transition predicted by CHIANTI at 335.339 Å is also density dependent as is the 338.278 Å line, and there is no reason why the 335.339 Å should not show the same observed characteristics as the 338.278 Å line. In fact, assuming a higher density for the 335.339 Å line increases the contribution of this line by up to a third, a non-negligible effect never reported before. This *first identification* of the line explains the problem with the 335.4 Å blend. In fact, in active region spectra the Fe XVI dominates, while in spectra such as those examined in this Section, any Fe XVI contribution is obviously ruled out, because the other un-blended Fe XVI line of the doublet is absent, and the Mg VIII 335.253 is not sufficient to explain the observed intensity.

- The complete list of identified lines of these spectra is given in Table C.2.

A comparison of different ionization equilibrium calculations

In these quiet sun equatorial regions the plasma is expected to be in ionization equilibrium, and since the thermal distribution is almost isothermal, and many lines from different sequences and ions are observed, this type of observations allow a direct check of the ionization equilibrium calculations, something that has not previously been done in detail. In fact, very few such attempts have been made, only comparing a few ions. For example, *Brickhouse et al.* (1995) presented a comparison between the results obtained from using only the Fe lines with the *Arnaud and Rothenflug* (1985) and *Arnaud and Raymond* (1992) calculations, but with no definite conclusions.

Table 3.11: *A selection of lines from the off-limb quiet sun observation of May 4th 1997, showing the comparisons of the results when using different ionization equilibrium calculations. For each observed line, the first line gives the results as calculated with* Arnaud and Rothenflug *(1985). All of them have been calculated at the same constant density $N_e = 3.5\text{x}10^8$ and with the same DEM shown in Figure 3.31. Note the large differences for the different ionization equilibrium calculations.*

Ion	λ_{th} (Å)	λ_{ob} (Å)	Transition	I_{ob}	I_{th}/I_{ob}	+/-	Det	log T_{eff}	log T_{max}	frac
Ne VII	465.22	465.2	2s2 $^1S_0$ - 2s2p $^1P_1$	142.2	0.76	0.08	G 3	5.98	5.72	
			(*Mazzotta et al.*, 1998)		1.21	0.13		5.98	5.71	
Mg VII	367.674	367.7	2s22p2 $^3P_2$ - 2s2p3 $^3P_2$	84.7	0.61	0.07	N 1	5.98	5.81	0.77
			(*Mazzotta et al.*, 1998)		0.48	0.05		5.98	5.81	
Mg VII	367.683		2s22p2 $^3P_2$ - 2s2p3 $^3P_1$						5.81	0.23
Ca IX	466.239	466.3	3s2 $^1S_0$ - 3s.3p $^1P_1$	39.8	0.45	0.06	G 3	5.98	5.78	
			(*Mazzotta et al.*, 1998)		2.02	0.26		6.00	5.80	
Si VII	275.353	275.3	2p4 $^3P_2$ - 2s.2p5 $^3P_2$	60.6	0.91	0.12	G 2	5.99	5.77	
			(*Mazzotta et al.*, 1998)		1.25	0.17		6.00	5.77	
Na VIII	411.166	411.1	2s2 $^1S_0$ - 2s.2p $^1P_1$	22.8	1.13	0.15	G 3	5.99	5.86	
			(*Mazzotta et al.*, 1998)		1.57	0.21		6.00	5.86	
Mg VIII	315.039	315.0	2p $^2P_{3/2}$ - 2s.2p2 $^2P_{3/2}$	264.8	1.05	0.11	N 1	6.00	5.91	

Table 3.11: *(continued)*

Ion	λ_{th} (Å)	λ_{ob} (Å)	Transition	I_{ob}	I_{th}/I_{ob}	+/-	Det	log T_{eff}	log T_{max}	frac
			(*Mazzotta et al.*, 1998)		0.97	0.10		6.00	5.91	
Ne VIII	770.409	770.8	1s2 2s $^2S_{1/2}$ - 1s2 2p $^2P_{3/2}$	294.1	1.81	0.20	G 4	6.02	5.79	
			(*Mazzotta et al.*, 1998)		1.86	0.21		6.02	5.80	
Si VIII	319.826	319.9	2s22p3 $^4S_{3/2}$ - 2s2p4 $^4P_{5/2}$	323.0	1.15	0.12	N 1	6.02	5.91	
			(*Mazzotta et al.*, 1998)		1.66	0.17		6.03	5.93	
Ca X	557.765	557.8	3s $^2S_{1/2}$ - 3p $^2P_{3/2}$	39.6	1.00	0.10	N 2	6.02	5.82	
			(*Mazzotta et al.*, 1998)		3.24	0.33		6.03	5.86	
Fe IX	171.073	171.1	3p6 $^1S_0$ - 3p5.3d $^1P_1$	3766.6	1.09	0.11	G 1	6.03	5.96	
			(*Mazzotta et al.*, 1998)		0.93	0.09		6.01	5.85	
			(*Arnaud and Raymond*, 1992)		0.94	0.10		6.01	5.85	
Mg IX	368.07	736.0	2s2 $^1S_0$ - 2s.2p $^1P_1$	1069.1	0.92	0.14	G 4	6.03	5.98	
			(*Mazzotta et al.*, 1998)		1.32	0.13		6.03	5.98	
O VI	173.079	173.1	1s2 2p $^2P_{3/2}$ - 1s2 3d $^2D_{5/2}$	116.2	0.74	0.13	G 1	6.04	5.51	0.60
			(*Mazzotta et al.*, 1998)		0.74	0.12		6.04	5.51	
O VI	172.935		1s2 2p $^2P_{1/2}$ - 1s2 3d $^2D_{3/2}$						5.51	0.33
Al IX	282.422	282.6	2s2.2p $^2P_{1/2}$ - 2s.2p2 $^2P_{1/2}$	28.9	0.93	0.17	G 2	6.04	6.03	
			(*Mazzotta et al.*, 1998)		0.72	0.13		6.04	6.04	
Si IX	341.949	342.0	2s22p2 $^3P_0$ - 2s2p3 $^3D_1$	99.4	1.03	0.10	N 1	6.04	6.03	
			(*Mazzotta et al.*, 1998)		0.90	0.09		6.05	6.06	
Fe X	345.723	345.7	3s2.3p5 $^2P_{3/2}$ - 3s.3p6 $^2S_{1/2}$	133.9	1.19	0.12	N 1	6.04	6.04	
			(*Mazzotta et al.*, 1998)		1.17	0.12		6.03	5.98	
			(*Arnaud and Raymond*, 1992)		1.16	0.12		6.03	5.98	
Mg X	609.793	609.8	1s2.(1s).2s $^2S_{1/2}$ - 1s2.(1s).2p $^2P_{3/2}$	364.2	1.55	0.15	N 2	6.05	6.04	
			(*Mazzotta et al.*, 1998)		1.47	0.15		6.05	6.05	
Fe XI	352.662	352.7	3s2.3p4 $^3P_2$ - 3s.3p5 $^3P_2$	177.1	1.10	0.11	N 1	6.06	6.11	
			(*Arnaud and Raymond*, 1992)		1.35	0.14		6.05	6.06	
			(*Mazzotta et al.*, 1998)		1.36	0.14		6.05	6.06	
Al X	332.789	332.8	2s2 $^1S_0$ - 2s.2p $^1P_1$	104.1	1.14	0.13	N 1	6.06	6.09	
			(*Mazzotta et al.*, 1998)		1.34	0.15		6.06	6.10	
Si X	271.983	272.0	2p $^2P_{1/2}$ - 2s.2p2 $^2S_{1/2}$	105.4	1.03	0.12	G 2	6.07	6.13	
			(*Mazzotta et al.*, 1998)		0.75	0.09		6.07	6.14	
Al IX	284.042	284.5	2s2.2p $^2P_{3/2}$ - 2s.2p2 $^2P_{3/2}$	79.7	1.11	0.14	G 2	6.07	6.03	0.76
			(*Mazzotta et al.*, 1998)		1.04	0.13		6.08	6.04	0.63
Fe XV	284.16		3s2 $^1S_0$ - 3s3p $^1P_1$						6.29	0.24
			(*Mazzotta et al.*, 1998)						6.32	0.37
Fe XII	364.467	364.5	3s2.3p3 $^4S_{3/2}$ - 3s.3p4 $^4P_{5/2}$	138.3	0.95	0.10	N 1	6.07	6.16	
			(*Arnaud and Raymond*, 1992)		1.71	0.18		6.07	6.13	
			(*Mazzotta et al.*, 1998)		1.70	0.17		6.07	6.14	
Al XI	550.031	550.1	1s2.(1s).2s $^2S_{1/2}$ - 1s2.(1s).2p $^2P_{3/2}$	12.5	2.08	0.21	N 2	6.08	6.16	
			(*Mazzotta et al.*, 1998)		1.88	0.19		6.08	6.16	
Si XI	580.907	580.9	2s2 $^1S_0$ - 2s.2p $^3P_1$	12.5	0.44	0.05	N 2	6.08	6.19	
			(*Mazzotta et al.*, 1998)		.48	0.05		6.09	6.20	
Fe XIII	348.183	348.2	3s2 3p2 $^3P_0$ - 3s 3p3 $^3D_1$	55.0	0.92	0.11	N 1	6.09	6.20	
			(*Arnaud and Raymond*, 1992)		1.86	0.22		6.08	6.20	
			(*Mazzotta et al.*, 1998)		1.82	0.21		6.08	6.20	
Si XII	520.665	520.8	1s2.2s $^2S_{1/2}$ - 1s2.2p $^2P_{1/2}$	8.6	1.09	0.11	N 2	6.11	6.26	
			(*Mazzotta et al.*, 1998)		0.85	0.09		6.11	6.28	
Fe XIV	334.172	334.2	3s2 3p $^2P_{1/2}$ - 3s 3p2 $^2D_{3/2}$	18.2	1.14	0.17	N 1	6.11	6.24	
			(*Arnaud and Raymond*, 1992)		2.01	0.30		6.10	6.26	
			(*Mazzotta et al.*, 1998)		1.93	0.29		6.10	6.26	

Table 3.11 presents a further selection of lines, representative of some of the principal ions observed, together with a comparison of the results that are obtained with different ionization equilibrium calculations (*Arnaud and Rothenflug*, 1985 and *Mazzotta et al.*, 1998 for all the ions, and *Arnaud and Raymond*, 1992 for the Fe ions). All the theoretical intensities have been calculated at the same constant density $N_e = 3.5 \times 10^8$ and with the DEM shown in Figure 3.31. The following conclusions can be drawn:

- the *Arnaud and Raymond* (1992) calculations for Fe are in disagreement with those derived from the *Arnaud and Rothenflug* (1985), both using Fe and other elements. In particular, all the higher Fe ionization states (Fe XI, Fe XII, Fe XIII, Fe XIV) present increasing disagreements up to almost a factor of 2.

- The recent calculations of *Mazzotta et al.* (1998) present a completely different picture. The intensities of all the Fe ions are in general agreement with those of *Arnaud and Raymond* (1992), while most of the ions of the other elements are changed by large factors, when compared to *Arnaud and Rothenflug* (1985). This comparison shows how much the ionization equilibrium affects the calculations. Unfortunately, even these recent calculations do not produce consistent results. The intensities of all the 'hotter' Fe ions are increased by large factors, cancelling the disagreement between these lines and the Li-like ions Mg X, Al XI. However, other ions such as Si X (or Mg VIII) have decreased theoretical intensities, making it impossible to find a different DEM that could well represent the brightest lines from the observed ions. It should be noted that the *Mazzotta et al.* (1998) calculations as a consequence imply different element abundances. For example, for Ca IX and Ca X, the differences are to increase the theoretical intensities by large factors, thus cancelling the need to increase the Ca abundance from its photospheric value, needed if *Arnaud and Rothenflug* (1985) is used. For the Na and Al ions, the differences are not so large and not consistent for each element, and the element abundances deduced from the *Arnaud and Rothenflug* (1985) are probably correct.

In conclusion, the old *Arnaud and Rothenflug* (1985) ionization equilibrium calculations better represent the majority of the ions, and should not be used in conjunction with the *Arnaud and Raymond* (1992) calculations. The recent *Mazzotta et al.* (1998) results indicate that some element abundances deduced by the use of *Arnaud and Rothenflug* (1985) are probably wrong (Ca in particular), and that some of the disagreement between the Li-like ions and all the others may also be due to incorrect ionization equilibrium calculations (if indeed there is equilibrium at all). However, the *Mazzotta et al.* (1998) calculations do not produce a coherent picture and are not used in the rest of this thesis. Note that these conclusions are the same independently on the adopted calibration, since the differences between the calibration presented in this thesis and the CDS standard one are smaller.

The line identifications and the theoretical spectra

Table C.2 presents a list of the principal lines identified in the spectra, with comments. Only those lines that are a complex combination of first and second order lines, and the few unidentified ones are not displayed in the Table. Figures 3.32,3.34, 3.35,3.36 show the calculated synthetic spectra, that consider both first and second order lines, with the observed spectra displayed for comparison. The agreement is excellent, confirming that overall, the instrument calibration and the various assumptions are reasonable. The evident disagreements are in all cases due to either ghosting problems in the GIS or in the case of lines of Li-like ions. Figure 3.33 shows the NIS 1 synthetic spectrum, in physical units, and visually confirms the much reduced NIS 1 sensitivity at the shorter wavelengths. These types of figures were created for all the observations analysed, all the detectors and for the first and second order, and used as a general check.

The GIS ghosts

Figures C.7,C.8,C.9,C.10 show the off-limb GIS spectra (May 4th 1997) with the blue- and red-shifted and the likely ghosting areas, while Table C.2.1 presents the corrections for ghosting that have been applied. Many lines are complex combinations of contaminations and ghosting and have not been corrected. The GIS 2 detector is the worst case, although strong ghosting is also present in GIS 1 and GIS 4.

These off-limb spectra are particularly useful to check the ghosting (or not) of some lines. As an example, the ghosting of the lines in the 430-440 Å region into the 400-410 Å region can be almost completely ruled out, because no bright ghosts are observed. In any on-disc spectra, the 400-410 Å region has bright transition region lines, that could have masked the presence of ghosts. On the other hand, ghosting of the lines in the 400-410 Å region toward the 430-440 Å region can not be ruled out completely (and furthermore is impossible to observationally check, because the lines in the 430-440 Å region are always visible when those in the 400-410 Å region are. More details on which lines have ghosting or are contaminated can be found in the Table, which also lists the 'pure ghosts' identified (see the comparison observed-versus-synthetic spectra for a direct visual identification of the brightest ghosts).

3.4.12 The on-disc observation of October 16th 1997. Full list of identified lines

A *DEM* analysis was performed on the on-disc spectra of 1997 October 16. A constant pressure $P_\mathrm{e} = 4\mathrm{x}10^{14}$ (cm^{-3} K) was used for the calculation of the contribution functions. Figure 3.37 shows the resulting *DEM*, that has a peak at 1.1 $\mathrm{x}10^6$ K. The photospheric abundances of *Grevesse and Anders* (1991) were used, except for Ne (+0.2), Al (+0.3), Ca (+0.6) [numbers in parentheses are usual differences in dex from photospheric values].

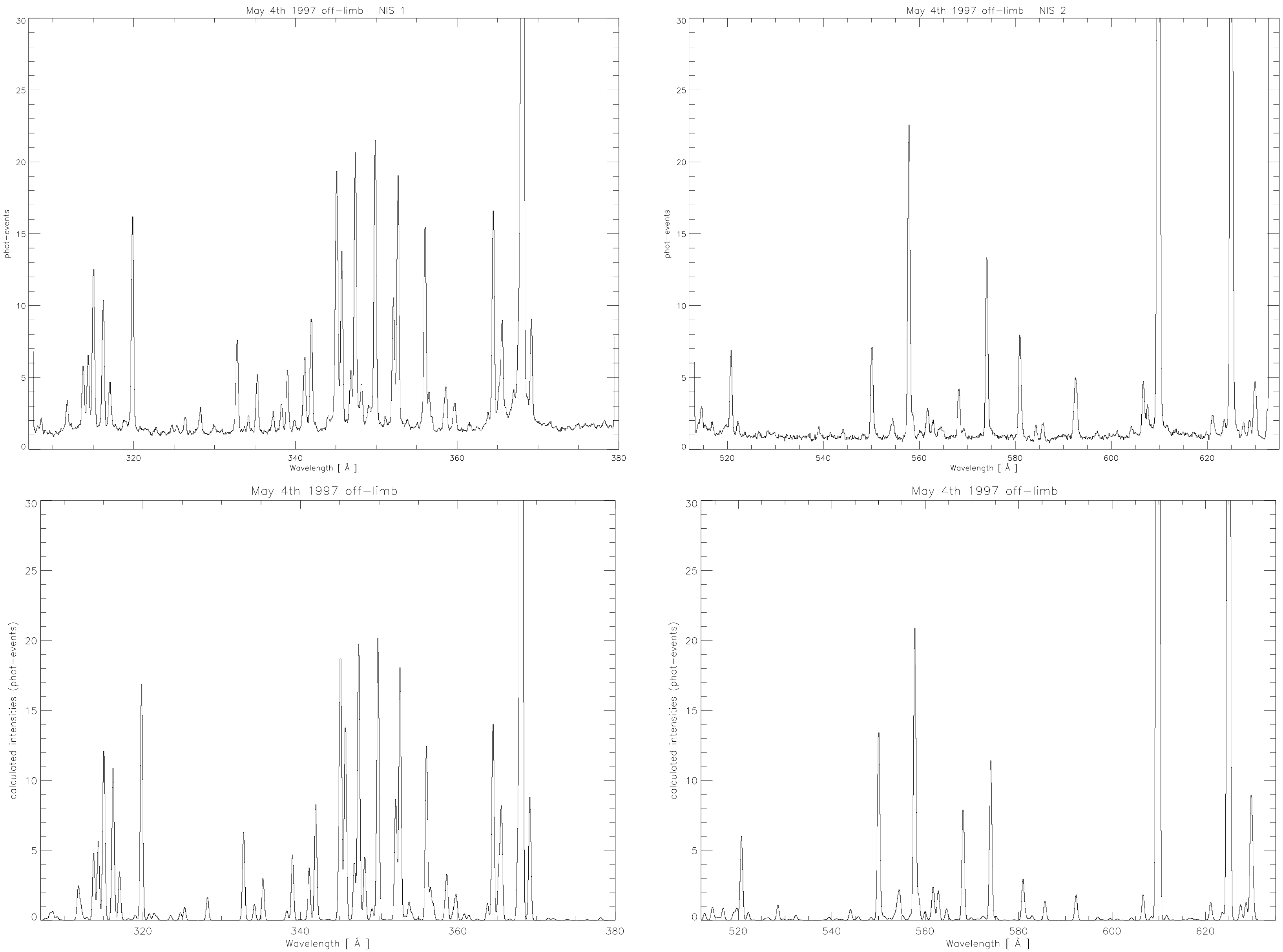

Figure 3.32: *Top: the NIS 1 and NIS 2 spectra of the off-limb quiet sun observation of May 4th 1997. Bottom: the corresponding synthetic spectra.*

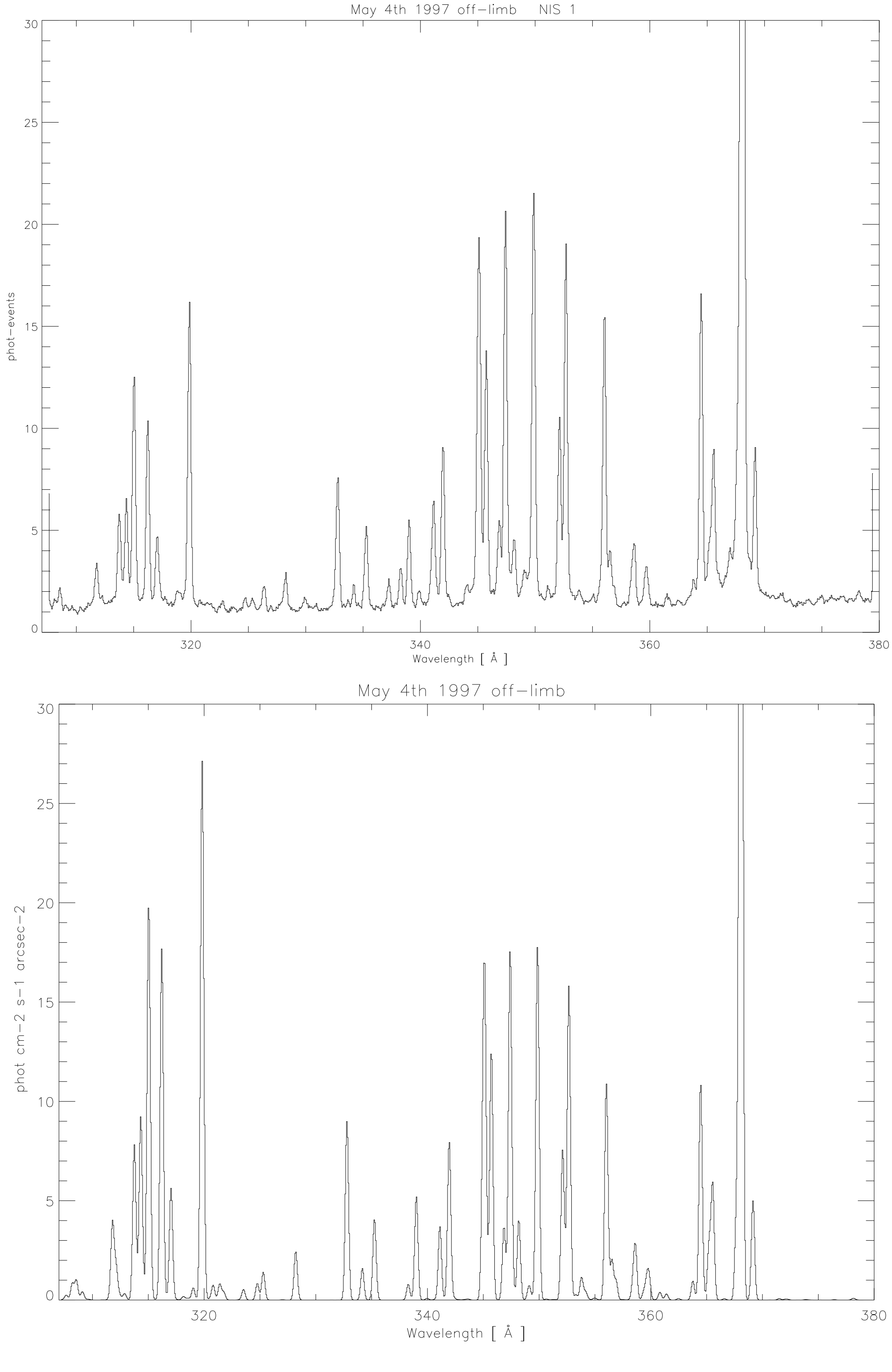

Figure 3.33: *Top: the NIS 1 spectrum of the off-limb quiet sun observation of May 4th 1997. Bottom: the corresponding synthetic spectrum, in physical units. Note how how the lines at shorter wavelengths are much depressed in the observed spectrum, indicating a much lower NIS 1 sensitivity at those wavelengths. Also, note that the central region of the spectrum is well represented, indicating how the instrument sensitivity is fairly constant there. Similar examples for all the other channels, first and second order have been produced for all the observations analysed, and used as a general check.*

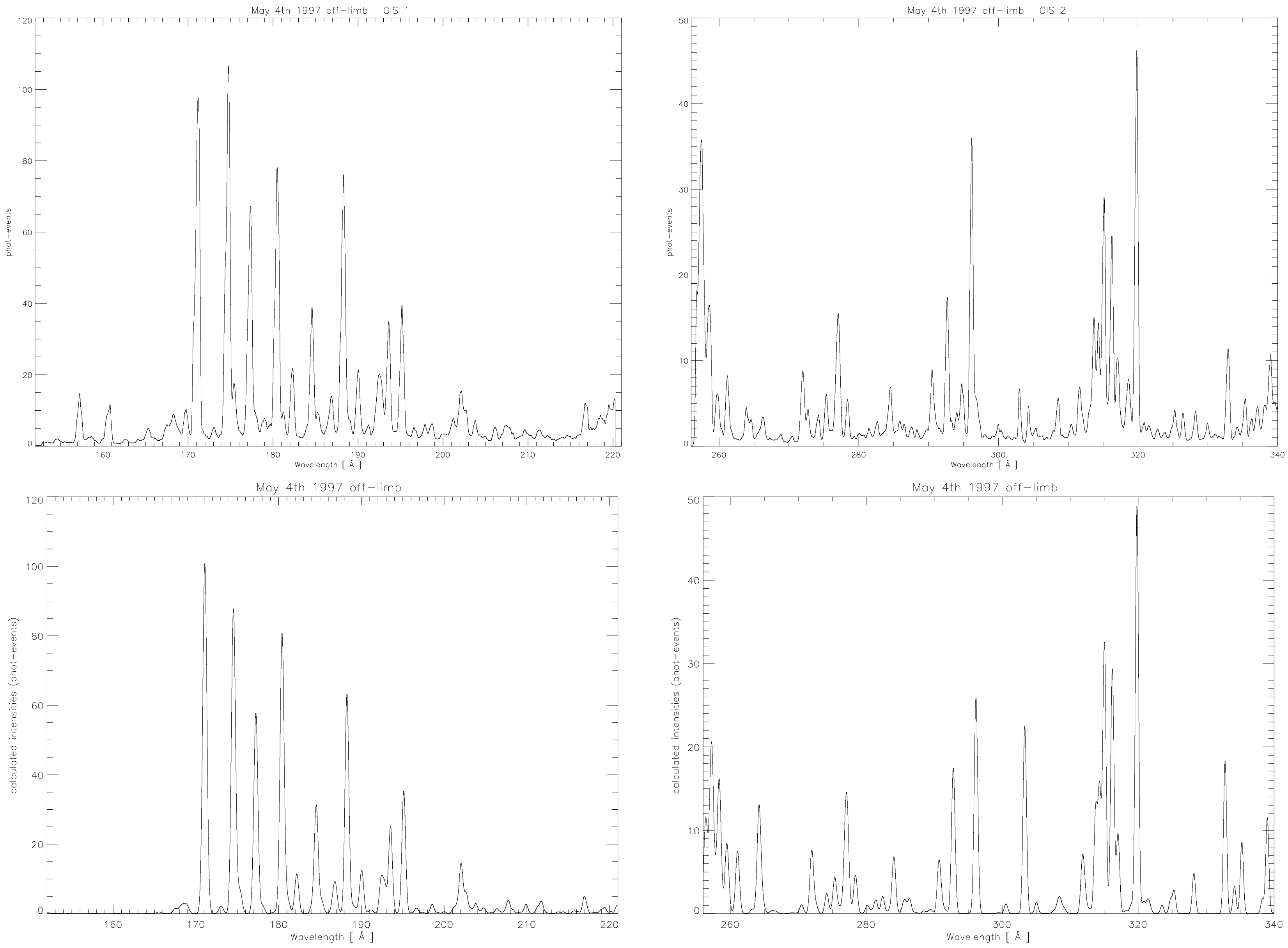

Figure 3.34: *Top: the GIS 1 and GIS 2 spectra of the off-limb quiet sun observation of May 4th 1997. Bottom: the corresponding synthetic spectra.*

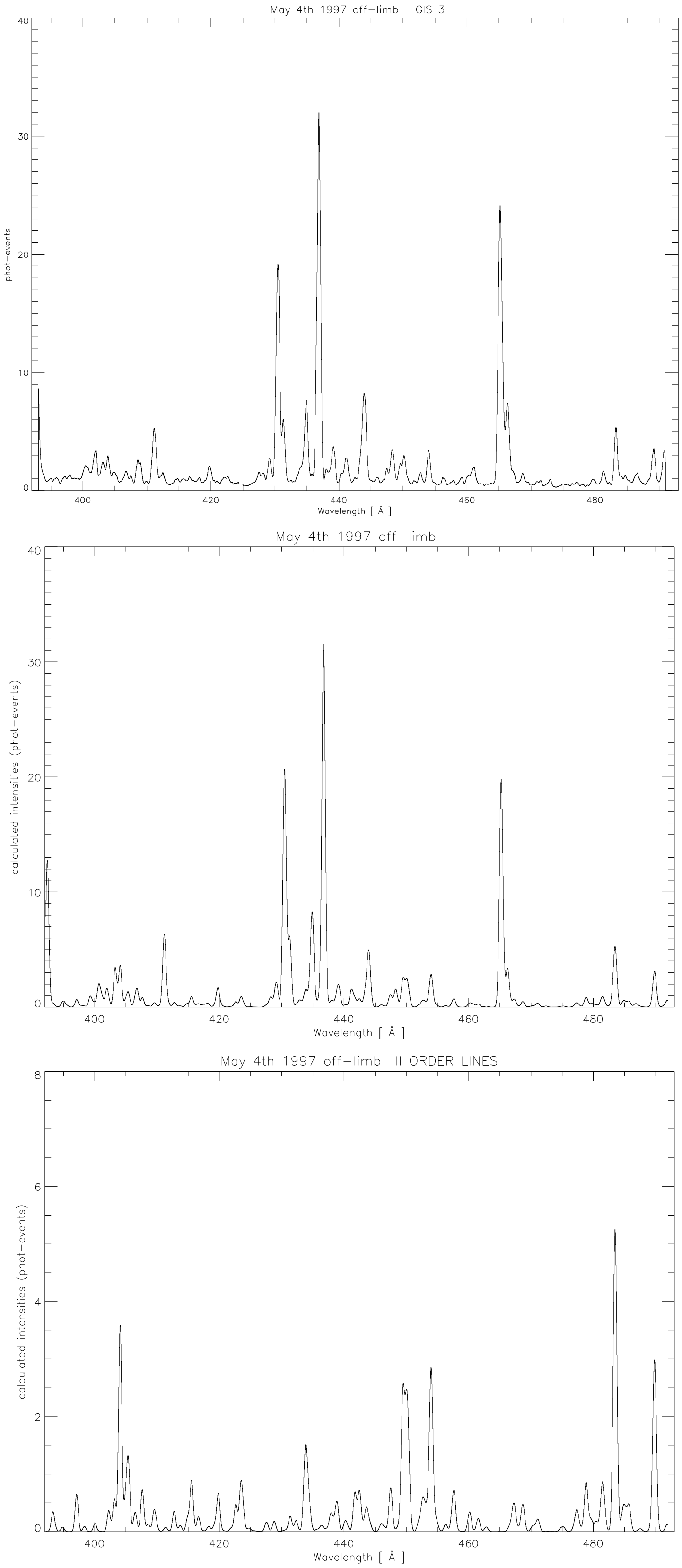

Figure 3.35: *Top: the GIS 3 spectrum of the off-limb quiet sun observation of May 4th 1997. Middle: the corresponding synthetic spectrum, on the same scale. Bottom: the synthetic spectrum with only the second order lines (note the different scale). Many second order lines are blended with first order ones, here, but there are still many that are not, in particular at middle and higher wavelengths. These lines were used to constrain the second order sensitivity.*

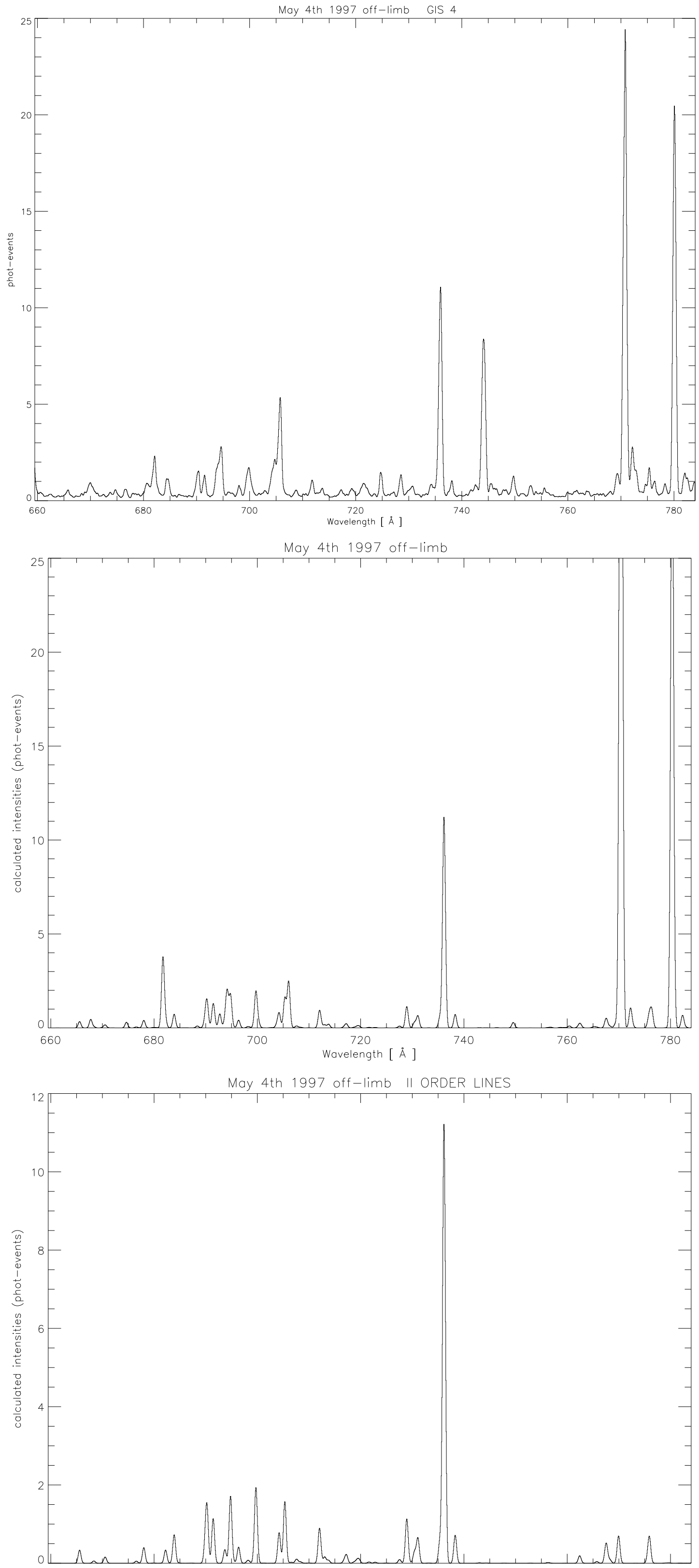

Figure 3.36: *Top: the GIS 4 spectrum of the off-limb quiet sun observation of May 4th 1997. Middle: the corresponding synthetic spectrum, on the same scale. Bottom: the synthetic spectrum with only the second order lines (different scale) Note the fact that most of the lines that are seen in GIS 4 are second order lines, and moreover not blended with the cool lines. These types of observations were used to constrain the GIS 4 second order sensitivity in the central and higher wavelength region.*

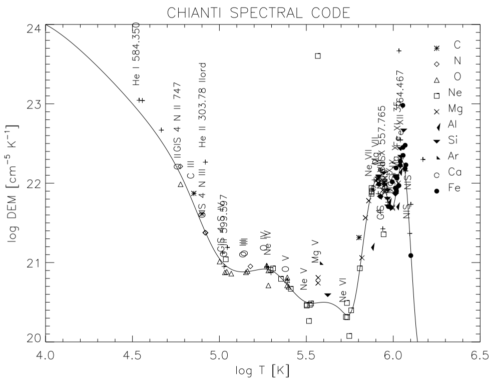

Figure 3.37: *The derived DEM for the on-disc quiet sun observation of 1997 October 16.*

Table C.4 lists the identified lines in the spectra. As in the off-limb case, synthetic spectra were calculated. They are displayed together with the observed spectra, for a direct comparison, in Figures 3.38, 3.39, 3.40.

The GIS ghosts

Figures C.17,C.18,C.19,C.20 show the on-disc GIS spectra (October 16th, 1997) with the blue- and red-shifted and the likely ghosting areas, while Table C.3.1 presents the corrections for ghosting that have been applied.

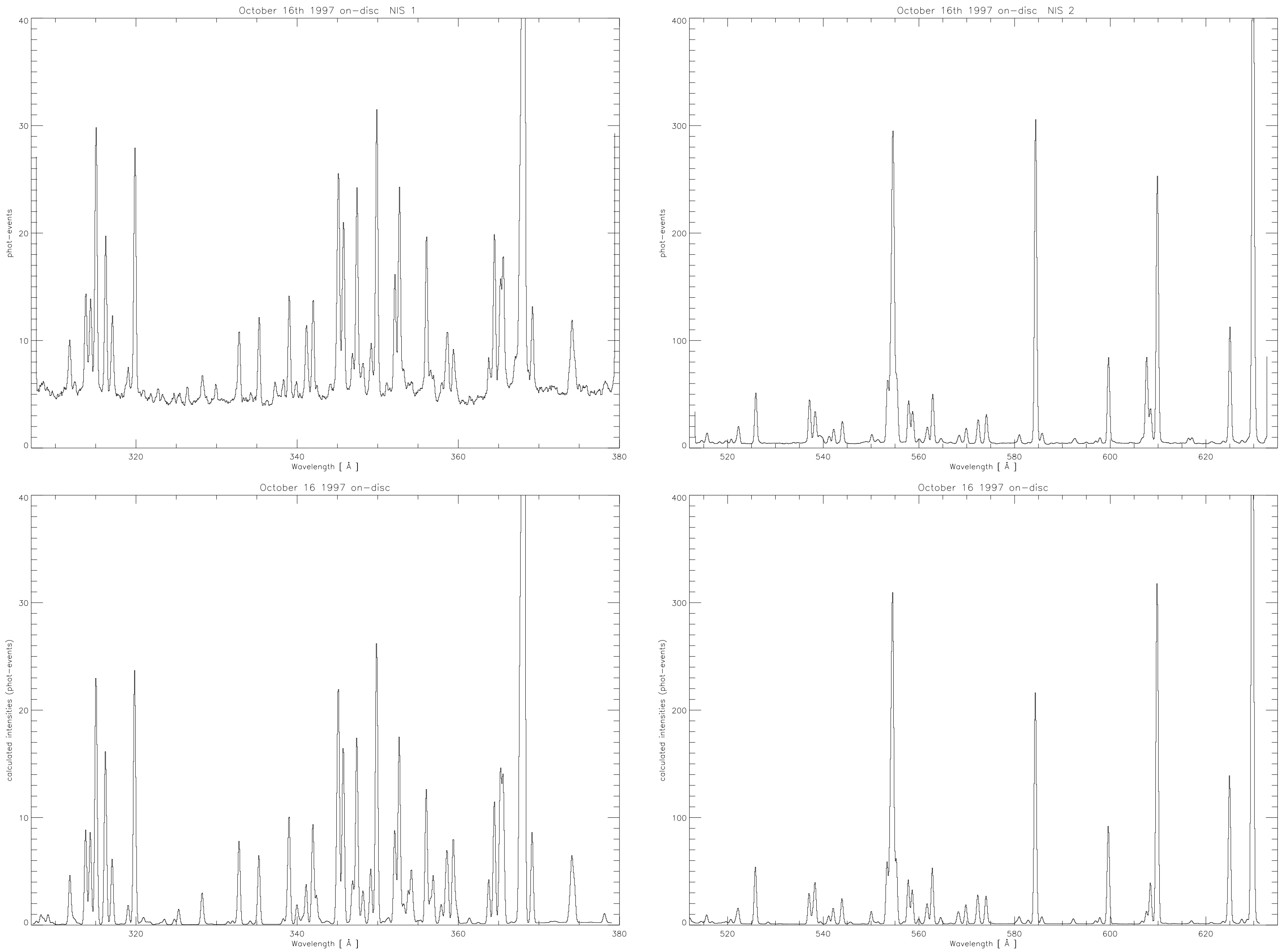

Figure 3.38: *Top: the NIS 1 and NIS 2 spectra of the on-disc quiet sun observation of October 16th 1997. Bottom: the corresponding synthetic spectra.*

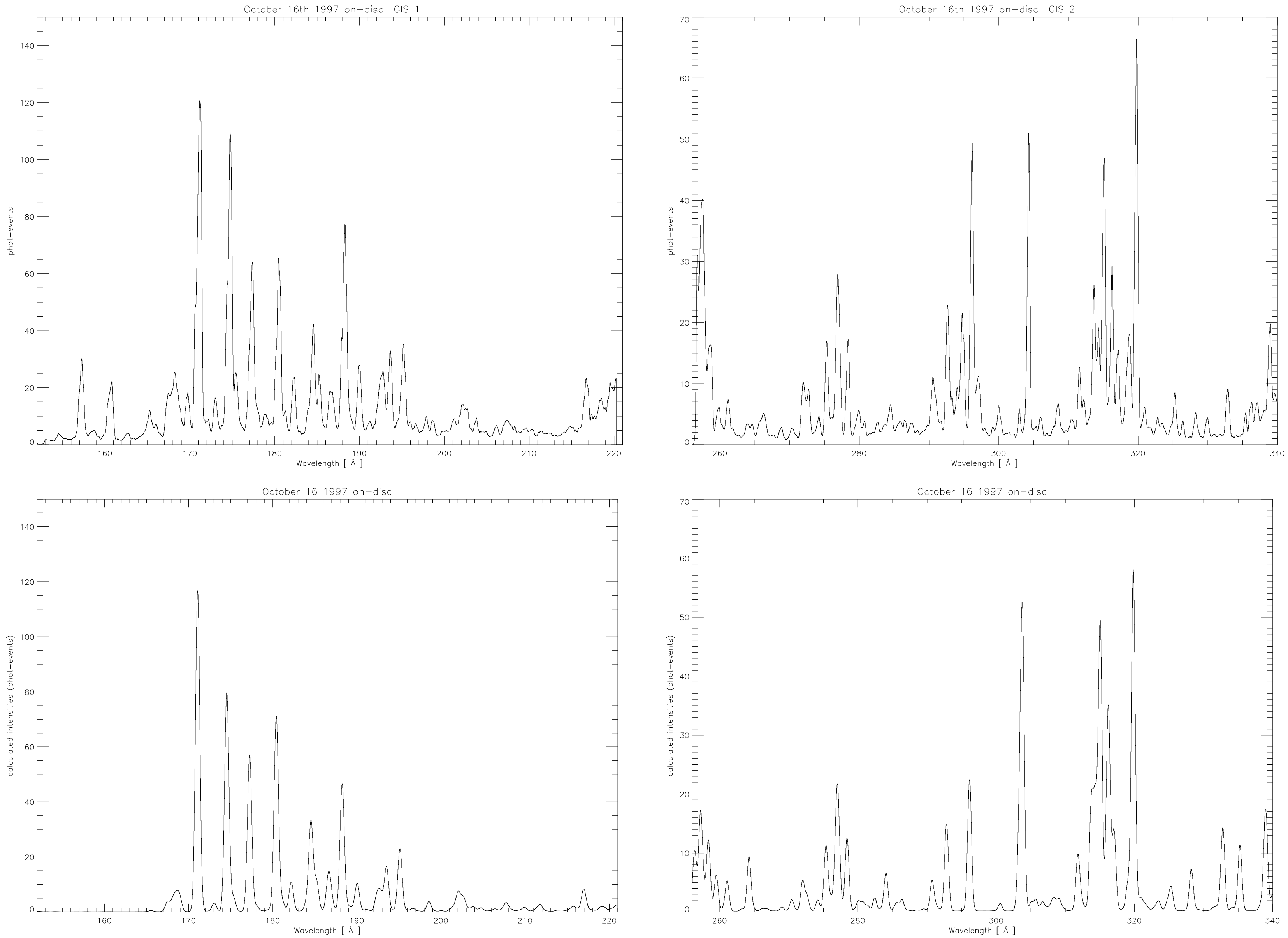

Figure 3.39: *Top: the GIS 1 and GIS 2 spectra of the on-disc quiet sun observation of October 16th 1997. Bottom: the corresponding synthetic spectra.*

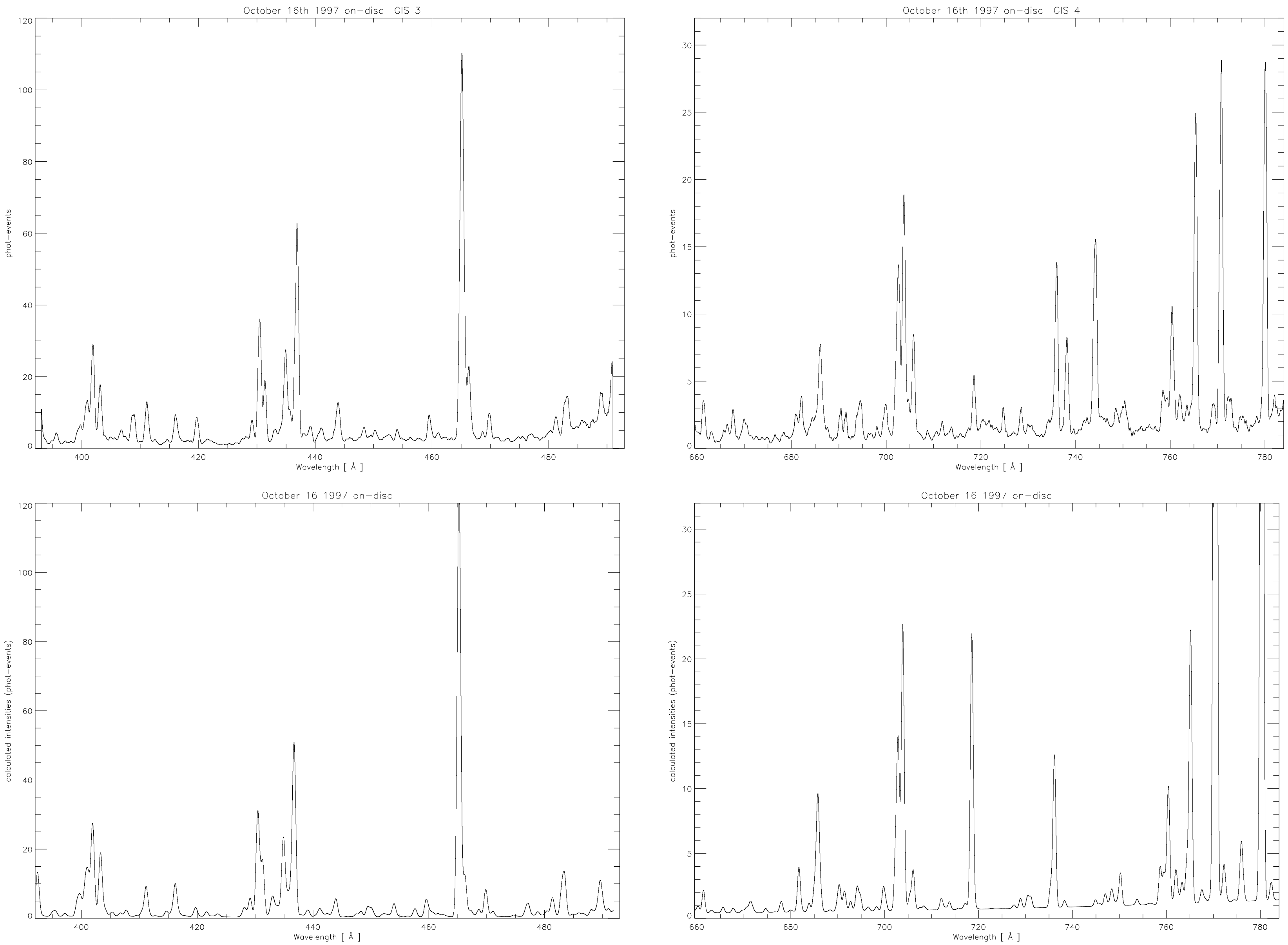

Figure 3.40: *Top: the GIS 3 and GIS 4 spectra of the on-disc quiet sun observation of October 16th 1997. Bottom: the corresponding synthetic spectra.*